



**Technische Universität München  
Fakultät für Physik**

**Methodology and Applications of Electrochemical Scanning  
Tunneling Microscopy for the Evaluation of Electrocatalysts  
under Reaction Conditions**

**Richard William Haid**

Vollständiger Abdruck der von der Fakultät für Physik der Technischen Universität München zur Erlangung des akademischen Grades eines

Doktors der Naturwissenschaften (Dr. rer. nat.)

genehmigten Dissertation.

Vorsitzender: Prof. Dr. Martin Zacharias  
Prüfer der Dissertation: 1. Prof. Dr. Aliaksandr S. Bandarenka  
2. Prof. Dr. Vitaly Alexandrov

Die Dissertation wurde am 12.04.2022 bei der Technischen Universität München eingereicht und durch die Fakultät für Physik am 20.06.2022 angenommen.



## **Abstract**

Electrocatalysis is a crucial element of sustainable energy production approaches. However, often there are critical drawbacks associated with this process, such as low efficiency and the use of scarce materials. To be able to counteract these issues, it is important to understand the origin of catalytic activity on a fundamental level. It is generally acknowledged that the atomic arrangement and composition of a surface determine the reactivity, and consequently, not all types of sites contribute equally to the overall activity. To improve the catalyst design, it is therefore imperative to find out which sites of a material are the most active. The simplest imaginable way to accomplish this would be to directly ‘watch’ what happens during the reaction on the catalyst surface. To a degree, the technique central to this thesis, noise electrochemical scanning tunneling microscopy (n-EC-STM), provides a means to achieve this. The EC-STM can visualize the electronic structure of a sample surface with down to atomic resolution. Under reaction conditions, the active sites will be revealed by a noisy signal at their position. The reason for this is the locally confined fluctuation in the tunneling properties caused by the reaction cycles. This thesis explores several novel aspects of n-EC-STM. First, a way to obtain quantitative information about the site-specific activity is developed on Pt(111). A linear relation between noise level and reaction rate is found. Based on this observation, the activity of various step sites is quantified and compared to the basal plane. Second, the possibility to visualize individual active sites with the n-EC-STM technique is demonstrated on a graphite surface, where the hydrogen evolution is investigated as a model reaction. With the resolution on an atomic level, the position of the active sites is pinpointed close to step edges and defects. The third investigation focuses on the evaluation of bifunctionally active sites. Here, the structure sensitivity of the oxygen reduction and evolution reactions was analyzed on a graphite surface. The results indicate that the active sites for both reactions are located along step edges, while the basal plane is largely inactive. Lastly, the n-EC-STM analysis is extended to a more complex system, namely manganese dioxide sheets on a modified graphite surface. The most active centers for oxygen evolution are found along the edges of the manganese dioxide sheets. In summary, the herein presented results open up new avenues for the analysis of catalytic materials with n-EC-STM. As a consequence, more substantial conclusions can be

reached, leading to a deeper understanding of electrocatalytic systems. Additionally, the identification of active sites is showcased on model systems for several key reactions in energy conversion.

## **Kurzfassung**

Elektrokatalyse ist ein Schlüsselverfahren in Ansätzen zur nachhaltigen Energieerzeugung. Allerdings sind mit diesem Verfahren häufig erhebliche Nachteile verbunden, wie z. B. geringe Effizienz und die Verwendung wertvoller Materialien. Um diesen Problemen entgegenwirken zu können, ist es wichtig, den Ursprung der katalytischen Aktivität auf einer grundlegenden Ebene zu verstehen. Es ist allgemein anerkannt, dass die atomare Anordnung und Zusammensetzung einer Oberfläche die Reaktivität beeinflusst und folglich nicht alle Arten von Zentren gleichermaßen zur Gesamtaktivität beitragen. Zur Verbesserung des Aufbaus eines Katalysators ist es daher zwingend notwendig, herauszufinden, welche Stellen eines Materials am aktivsten sind. Der simpelste vorstellbare Weg, dies zu erreichen, wäre, direkt zu "sehen", was während der Reaktion auf der Katalysatoroberfläche abläuft. Zu einem gewissen Grad bietet die Technik, die im Mittelpunkt dieser Arbeit steht, die elektrochemische Rastertunnelmikroskopie (EC-STM), eine Möglichkeit, dies zu erreichen. Mit Hilfe von EC-STM kann die elektronische Struktur einer Probenoberfläche mit einer Auflösung auf atomarer Ebene sichtbar gemacht werden. Unter Reaktionsbedingungen werden die aktiven Stellen durch ein verrauschtes Signal an ihrer Position ersichtlich. Der Grund dafür sind lokal begrenzte Fluktuation in den Tunneleigenschaften, die durch die Reaktionszyklen verursacht werden. In dieser Dissertation werden mehrere neue Aspekte dieser n-EC-STM genannten Methode untersucht. Zunächst wird ein Verfahren entwickelt, das quantitative Information über die ortsspezifische Aktivität auf Pt(111) liefert. Hierbei wird eine lineare Beziehung zwischen Rauschpegel und Reaktionsgeschwindigkeit nachgewiesen. Auf Grundlage dieser Beobachtung wird die Aktivität verschiedener Stufenkanten quantifiziert und mit der Basalebene verglichen. Als zweites wird die Möglichkeit, einzelne aktive Zentren mit der n-EC-STM-Technik sichtbar zu machen, an einer Graphitoberfläche demonstriert, wobei die Wasserstoffentwicklung als Modellreaktion untersucht wird. Mit Auflösung auf atomarer Ebene wird die Position der aktiven Stellen in der Nähe von Stufenkanten und Defekten präzise bestimmt. Die dritte Studie konzentriert sich auf die Bewertung von bifunktionell aktiven Zentren. Dazu wurde die Strukturempfindlichkeit der Sauerstoffreduktions- und -entwicklungsreaktionen auf einer Graphitoberfläche analysiert. Die Ergebnisse deuten darauf hin, dass sich die aktiven Stellen für beide Reaktionen entlang der Stufenkanten befinden, während die Basalebene weitgehend

inaktiv ist. Zum Abschluss wird die n-EC-STM-Analyse auf ein komplexeres System ausgeweitet, nämlich Mangandioxidplatten auf einer modifizierten Graphitoberfläche. Die aktivsten Zentren für die Sauerstoffentwicklung wurden entlang der Kanten der Mangandioxidplatten gefunden. Zusammengefasst eröffnen die hier vorgestellten Ergebnisse neue Möglichkeiten für die Analyse von katalytischen Materialien mit n-EC-STM. Infolgedessen können tiefergehende Erkenntnisse gewonnen werden, die zu einem verbesserten Verständnis von elektrokatalytischen Systemen führen. Darüber hinaus wird die Identifizierung aktiver Zentren an Modellsystemen für verschiedene Schlüsselreaktionen in der Energieumwandlung vorgestellt.

## List of Publications

1. Xue, S., **Haid, R. W.**, Kluge, R. M., Ding, X., Garlyyev, B., Fichtner, J., Watzele, S., Hou, S., & Bandarenka, A. S. (2020). Enhancing the hydrogen evolution reaction activity of platinum electrodes in alkaline media using Ni-Fe clusters. *Angewandte Chemie International Edition*, 59 (27), 10934-10938.
2. **Haid, R. W.**,<sup>(1)</sup> Kluge, R. M.,<sup>(1)</sup> Liang, Y & Bandarenka, A. S. (2021). In situ quantification of the local electrocatalytic activity via electrochemical scanning tunneling microscopy. *Small Methods*, 5, 2000710.
3. Kluge, R. M., **Haid, R. W.** & Bandarenka, A. S. (2021). Assessment of active areas for the oxygen evolution reaction on an amorphous iridium oxide surface. *Journal of Catalysis*, 396, 14-22.
4. Kluge, R. M.,<sup>(1)</sup> **Haid, R. W.**,<sup>(1)</sup> Stephens, I. E. L., Calle-Vallejo F. & Bandarenka, A. S. (2021). Monitoring active sites for hydrogen evolution reaction at model carbon surfaces. *Physical Chemistry Chemical Physics*, 23, 10051-10058.
5. **Haid, R. W.**,<sup>(1)</sup> Kluge, R. M.,<sup>(1)</sup> Schmidt, T. O. & Bandarenka, A. S. (2021). In-situ detection of active sites for carbon-based bifunctional oxygen reduction and evolution catalysis. *Electrochimica Acta*, 382, 138285.
6. Aufa, M. H.,<sup>(1)</sup> Watzele, S. A.,<sup>(1)</sup> Hou, S., **Haid, R. W.**, Kluge, R. M., Bandarenka, A. S. & Garlyyev, B. (2021). Fast and accurate determination of the electroactive surface area of MnO<sub>x</sub>. *Electrochimica Acta*, 389, 138692.
7. Hou, S.,<sup>(1)</sup> Kluge, R. M.,<sup>(1)</sup> **Haid, R. W.**,<sup>(1)</sup> Gubanova, E. L., Watzele, S. A., Bandarenka, A. S. & Garlyyev, B. (2021). A review on experimental identification of active sites in model bifunctional electrocatalytic systems for oxygen reduction and evolution reactions. *ChemElectroChem*, 8, 3433-3456.
8. **Haid, R. W.**,<sup>(1)</sup> Ding, X.,<sup>(1)</sup> Sarpey, T. K., Bandarenka, A. S. & Garlyyev, B. (2022). Exploration of the electrical double layer structure: influence of electrolyte components on the double layer capacitance and potential of maximum entropy. *Current Opinion in Electrochemistry*, 32, 100882.

## List of Publications

---

9. Ding, X.,<sup>(1)</sup> Scieszka, D.,<sup>(1)</sup> Watzele, S., Xue, S., Garlyyev, B., **Haid, R. W.** & Bandarenka, A. S. (2022). A systematic study of the influence of electrolyte ions on the electrode activity. *ChemElectroChem*, 9, 202101088.
10. Hou, S., Xu, L., Ding, X., Kluge, R. M., Sarpey, T. K., **Haid, R. W.**, Garlyyev, B., Mukherjee, S., Warnan, J., Koch, M., Zhang, S., Li, W., Bandarenka, A. S. & Fischer, R. A. S. (2022). Dual in-situ laser techniques underpin the role of cations in impacting electrocatalysts. *Angewandte Chemie International Edition*, (accepted, <https://onlinelibrary.wiley.com/doi/abs/10.1002/ange.202201610>).
11. **Haid, R. W.**,<sup>(1)</sup> Kluge, R. M.,<sup>(1)</sup> Schmidt, T. O. & Bandarenka, A. S. (2022). Finding efficient catalyst designs: A high-precision method to reveal active sites. *Chem Catalysis*, (accepted).
12. Kluge, R. M.,<sup>(1)</sup> Psaltis, E.,<sup>(1)</sup> **Haid, R. W.**, Hou, S., Schmidt, T. O., Schneider, O., Garlyyev, B., Calle-Vallejo, F., & Bandarenka, A. S. (2022). Revealing the nature of active sites on Pt-Gd and Pt-Pr alloys during the oxygen reduction reaction. *ACS Applied Materials & Interfaces*, (accepted).

<sup>(1)</sup> These authors contributed equally

## Conference Contributions

### Oral Presentations:

1. 9<sup>th</sup> Meeting of Electrochemistry in Nanoscience, ElecNano9, Paris, France, Virtual Conference, November 2020

**In-situ identification of active sites using electrochemical scanning tunneling microscopy**

2. Bruker European Material AFM Online User Meeting, March 2021

**In-situ identification of active sites using electrochemical scanning tunneling microscopy**

3. 72<sup>nd</sup> Annual Meeting of the International Society of Electrochemistry (ISE), Jeju, Korea, Hybrid Conference, August/September 2021

**Highly resolved imaging of active sites for carbon-based electrocatalysis under reaction conditions**

4. 5<sup>th</sup> International Conference on Applied Surface Science (ICASS), Palma, Mallorca, Spain, April 2022

**High-resolution imaging of active sites under reaction conditions for carbon-based electrocatalysis (*accepted*)**

5. 31<sup>st</sup> Topical Meeting of the ISE, Aachen, Germany, May 2022

**High-resolution imaging of active sites under reaction conditions for carbon-based electrocatalysis (*accepted*)**

6. 241<sup>st</sup> ECS Meeting, Vancouver, Canada, Hybrid Conference, May/June 2022

**High-resolution imaging of active sites under reaction conditions for carbon-based electrocatalysis (*accepted*)**

7. 32<sup>nd</sup> Topical Meeting of the ISE, Stockholm, Sweden, June 2022

**High-resolution imaging of active sites under reaction conditions for carbon-based electrocatalysis (*accepted*)**

**Poster Presentations:**

1. 708<sup>th</sup> WE-Heraeus Seminar, Bad Honnef, Germany, December 2019  
“Operando surface science - Atomistic insights into electrified solid/liquid interfaces”  
**In-situ identification of active sites using electrochemical scanning tunneling microscopy**
2. 10<sup>th</sup> Energy Colloquium of the Munich School of Engineering (MSE), Munich, Germany, Virtual Conference, July 2020  
“10 years of MSE: Energy Research in Bavaria”  
**Highly resolved in-situ imaging of active sites using electrochemical scanning tunneling microscopy**
3. 11<sup>th</sup> Energy Colloquium of the Munich School of Engineering (MSE), Munich, Germany, Virtual Conference, July 2021  
“Energy Sciences for Europe's Green Deal”  
**Highly resolved imaging of active sites for carbon-based electrocatalysis under reaction conditions**

## Table of Contents

Abstract.....	3
Kurzfassung .....	5
List of Publications .....	7
Conference Contributions .....	9
Table of Contents .....	11
1 Introduction and Motivation.....	15
1.1 The Role of Catalysis in the Solution of Global Issues .....	15
1.2 Significance and Identification of Active Catalytic Sites .....	17
1.3 Scope and Aim of this Research .....	18
2 Fundamentals of Electrocatalysis .....	21
2.1 Composition of the Electrified Electrode/Electrolyte Interface.....	22
2.2 Faradaic Processes at the Electrified Electrode/Electrolyte Interface .....	24
2.3 Electrochemical Evaluation of Reaction Kinetics .....	26
2.4 Binding of Reaction Intermediates at the Catalyst Surface .....	28
2.5 Overview of Experimental Techniques for the Identification of Active Sites.....	30
3 Model Catalytic Reactions .....	35
3.1 Acidic Hydrogen Evolution Reaction.....	37
3.2 Alkaline/Acidic Oxygen Reduction Reaction.....	39
3.3 Alkaline Oxygen Evolution Reaction .....	40
4 Electrochemical Scanning Tunneling Microscopy .....	43
4.1 Scanning Tunneling Microscopy .....	43
4.1.1 Operation in Electrochemical Environment .....	46
4.1.2 Tunneling in Electrolyte .....	47

## Table of Contents

---

4.2	Identification of Active Sites.....	50
4.3	Experimental Equipment.....	53
4.3.1	Bruker Multimode.....	53
4.3.2	Tip Preparation.....	55
5	Quantitative Determination of the Local Activity Using n-EC-STM .....	57
5.1	Preparation of the Pt(111) Single Crystals .....	58
5.2	Establishing a Noise-Activity Relation on the Basal Plane .....	59
5.3	Extracting the Site-Specific Turn-Over Frequency.....	65
5.4	Discussion .....	67
6	Highly Resolved Active Sites for the Hydrogen Evolution at Model Carbon Surfaces...	71
6.1	The Structure of Highly Oriented Pyrolytic Graphite .....	72
6.2	n-EC-STM at HOPG Terraces and Edges.....	73
6.3	High-Resolution of Active Sites.....	76
6.4	Discussion .....	78
7	Active Sites for Alkaline Oxygen Reduction and Evolution Catalysis on Graphite .....	83
7.1	n-EC-STM at Terraces and Step Sites.....	83
7.2	Monitoring a Larger Surface Area .....	86
7.3	High-Resolution of ORR Active Sites .....	88
7.4	Discussion .....	90
8	Monitoring the Oxygen Evolution on Manganese Oxide Nanosheets .....	93
8.1	<i>Ex-situ</i> Characterization of the Sample System .....	94
8.2	Active Sites of MnO <sub>2</sub> -NS under Oxygen Evolution Conditions.....	98
8.3	Discussion .....	101
9	Outlook: Influence of the Electrolyte Species .....	105
10	Summary and Conclusion .....	109

## Table of Contents

---

Appendix A: Acknowledgements.....	113
Appendix B: EC-STM Measurement Parameters .....	115
Appendix C: Additional Data of the Quantitative n-EC-STM Method .....	117
Appendix D: n-EC-STM of the HOPG Modified by a Carbonaceous Iron Porphyrin Film..	123
Appendix E: Symbols and Abbreviations .....	125
References .....	129



# 1 Introduction and Motivation

In many aspects of the global economy, catalysts are an indispensable element, and their importance is only going to increase in the future. Production of fundamental goods such as plastics, fertilizers, and pharmaceuticals would not be practicable without them. Moreover, promising conversion and storage devices for sustainable energy supply cannot be realized without appropriate catalytic components. Consequently, to control the human impact on the environment and hold or even increase the quality of life in the future, reaching a higher efficiency in catalytic systems needs to be a primary target.

## 1.1 The Role of Catalysis in the Solution of Global Issues

One of the most direct impacts of catalysis on human life can be observed in the agricultural sector. After the development of the Haber-Bosch process, large amounts of cheap fertilizer could be produced.<sup>[1]</sup> This event is seen as the starting point of the accelerated growth of the global population. However, the synthesis of the fertilizers requires large amounts of electricity and is responsible for approximately 2.5% of the world's fossil-based CO<sub>2</sub> emissions.<sup>[2]</sup> With a still-growing population, these numbers will likely increase further in the future. Consequently, the search for more efficient catalysts is now more important than ever.

Catalysis also plays an important role in the medical and healthcare sector. Often pharmaceuticals are produced using specifically designed catalysts in the process.<sup>[3]</sup> One example is menthol, an aromatic substance, which is a part of many pharmaceuticals and hygiene articles.<sup>[4]</sup> The demand for this chemical exceeds the naturally available resources. However, the development of catalytic pathways for the synthetic formation of menthol has been able to mitigate this circumstance.<sup>[3]</sup> Furthermore, as the COVID-19 pandemic has demonstrated, it can be necessary to produce basic medical equipment such as oxygen masks and protective wear fast and cheap. This is not possible without plastics which in their production rely heavily on catalytic support.<sup>[5]</sup>

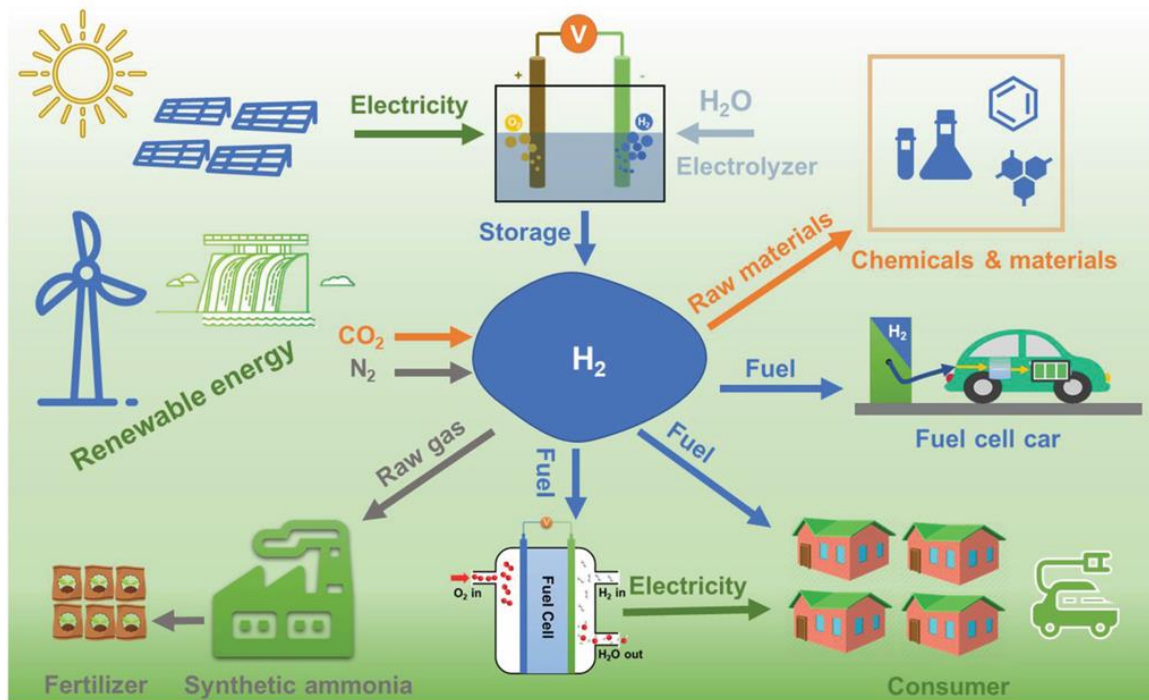


**Figure 1** Schematic of a hydrogen-based energy economy. Using renewable energy for water electrolysis produces ‘clean’ hydrogen. It can then be used in the production of chemicals and other materials. Moreover, it can be consumed in fuel cells to produce electricity in stationary and mobile applications. Since the whole system is based on water and its components, the sustainability is far superior to the current, carbon-dominated energy provision scheme. Reprinted with permission from Ref. [6], Copyright © 2020, The Authors.

The area which will arguably experience the most drastic changes in the near future is the energy sector. While the production of ‘green’ electricity by means of renewable sources is relatively straightforward, conversion and storage in sustainable ways remain critical issues.<sup>[7,8,9]</sup> Promising energy storage devices such as metal-air batteries depend strongly on catalytic materials.<sup>[10, 11, 12]</sup> Moreover, a hydrogen-based energy economy is generally considered one of the most promising solutions to the current crisis.<sup>[7,8,9,13]</sup> The basic idea, as sketched in Figure 1, is to produce hydrogen via electrolysis utilizing electricity from renewable sources. It can then be applied in the production of, *e.g.*, chemicals or be converted back to electricity in fuel cells. The system offers high sustainability as it is based mainly on water and its components. Thus, in the past three years, many countries and the European Union have developed hydrogen strategies involving large sums of money to advance the impact of hydrogen as an energy carrier.<sup>[14,15]</sup> Nevertheless, several important issues need to be solved

before the hydrogen economy can be practiced on a large scale. For instance, safe ways to transport and store large amounts of hydrogen are needed.<sup>[9,16,17]</sup> Furthermore, both the electrolysis of water and the generation of energy in fuel cells are obstructed by issues such as stability, selectivity, and efficiency of the components.<sup>[9,6,18,19]</sup> Thus, developing specific electrocatalysts that elevate the overall performance is particularly important. In addition, many state-of-the-art catalysts involve platinum group metals, which should be replaced by more economical and abundant alternatives such as carbon-based materials. The crucial question regarding these issues is how to know which materials are best to use and how to design the most efficient catalysts structures?

### **1.2 Significance and Identification of Active Catalytic Sites**

In the past, the identification of catalyst materials has mainly been based on a trial and error approach.<sup>[20,21,22]</sup> Naturally, this is not an efficient method, and improvements require long periods of time. For instance, already from experiments by Döbereiner in the first half of the 19<sup>th</sup> century, the ability of platinum to combine hydrogen and oxygen to form water at low temperatures is known.<sup>[23,24]</sup> Still today, researchers are trying to improve platinum as a catalyst or find more active and abundant alternatives.<sup>[25,26,27]</sup> Meaningful progress in any direction requires understanding the underlying chemical reasons for catalytic phenomena, which only started in the early 20<sup>th</sup> century when Sabatier and Langmuir developed basic principles for the adsorption of reaction species on the catalyst.<sup>[24,28,29]</sup> Based on these concepts, researchers have been looking for systematic ways of identifying and qualifying catalyst materials in the past decades. Theoretical models have been developed to perform large-scale screening of catalysts and predict suitable candidates for a given reaction.<sup>[30,31,32,33,34]</sup> However, just identifying the best materials and material combinations is not sufficient. In many cases, the catalytic properties are structure-dependent.<sup>[35,36,37,38,39]</sup> Hugh Stott Taylor already proposed in 1925 that a catalyst surface is not homogeneously active.<sup>[40]</sup> There are specific active sites that offer the most suitable conditions for a reaction due to their local electronic structure.<sup>[41,42,43]</sup> Consequently, to develop the most efficient catalyst, it is necessary to find the most promising materials and shape them in a way that maximizes the benefit from active sites. Therefore,

identifying the nature of the most active sites of a catalyst is an important research topic from both the theoretical and experimental sides.<sup>[44,45,46]</sup>

### 1.3 Scope and Aim of this Research

But what if one could simply ‘see’ which sites are active while the reaction occurs? In a way, noise electrochemical scanning tunneling microscopy (n-EC-STM) is a technique that comes close to this idea.<sup>[47]</sup> The scanning tunneling microscopy (STM) in general, and the n-EC-STM technique in particular, will be discussed in detail in Chapter 4. Essentially, the STM can reveal the electronic structure of a sample by scanning a sharp tip over the surface and monitoring the tunneling current between the two of them.<sup>[48]</sup> This can also be done in an electrochemical environment, thus allowing to image the surface of a catalyst under reaction conditions. In this case, active catalytic sites influence the tunneling when the tip passes over them, which causes locally confined noise in the STM signal. The resulting images can be seen as a representation of the surface structure superimposed by noise spikes at active sites. This novel technique has been successfully demonstrated on a variety of materials (such as platinum, platinum alloys, metal oxides, and dichalcogenides) and reactions (*e.g.*, oxygen reduction reaction (ORR), oxygen evolution reaction (OER), and hydrogen evolution reaction (HER)).<sup>[47][49][50][51][52][53][54]</sup> Since the method can visualize the active sites directly under reaction conditions, evaluating the catalyst performance becomes much faster and more straightforward. In combination with theoretical approaches and other experimental evaluation techniques, n-EC-STM adds to the comprehensive understanding of catalyst behavior, so that concrete guidelines for a smart material design can be proposed.

In this thesis, several methodological aspects of n-EC-STM will be studied, and the practical application to specific model systems will be demonstrated. Generally, the herein presented investigations are motivated by two independent reasons. Naturally, one aim is to gain insight and improve on the catalytic properties of the model system. At the same time, although n-EC-STM has already been applied to various classes of materials, it is a relatively young technique, and further methodological development is of great interest. Thus, the here presented experiments challenge the technique in specific aspects, such as improving the resolution and

obtaining quantitative information. In total, four independent studies using the n-EC-STM technique will be presented in this thesis:

- **Quantification of the local activity:**

In the first study, the possibilities of obtaining quantitative information on the activity of surface sites using the n-EC-STM technique are tested. As a model system, the well-studied (111) facet of a Pt single crystal is analyzed under ORR conditions in an acidic electrolyte. It is revealed that the noise level on the active basal plane scales linearly with the current density of the electrode. This relation is utilized to estimate the activity of step sites, yielding improvement factors similar to literature. The results demonstrate the capability of n-EC-STM to deliver qualitative and quantitative information on the activity of surface sites and confirm the activity trends reported in the literature regarding Pt(111) steps.

- **Atomically resolved active sites:**

The second study deals with transferring the ability of the STM to achieve an atomic resolution to n-EC-STM. The aim is to pinpoint individual active sites in the atomic structure of the catalyst. As the model system, highly oriented pyrolytic graphite (HOPG) is examined for the HER in acidic electrolyte. It is shown that the basal plane is largely inactive and that the majority of active sites are located near step edges and defects. It is demonstrated that these can be captured with resolution on an atomic level. The data is discussed utilizing theoretical calculations to confirm the experimental evidence.

- **n-EC-STM for bifunctional catalysis:**

In certain cases, catalysts are required to promote more than one reaction. In the third study, n-EC-STM is applied for such a situation. The investigation focuses on the oxygen reduction and evolution reactions on HOPG in an alkaline medium. It is found that the active sites are predominantly at the edge and defective sites for both reactions. The results include high-resolution images indicating that different surface sites become active at different potentials.

- **Oxygen evolution at manganese oxide:** Lastly, a more complex model system was analyzed with the n-EC-STM technique. A carbon sample decorated with nanosheets (NS) of manganese dioxide ( $\text{MnO}_2$ ) was scanned under OER conditions in an alkaline medium. Active sites were found on the surface and at the edge of the NS, while the substrate remained largely inactive at the applied potentials. By high-resolution imaging, the outstanding activity of the NS edge sites was confirmed, indicating particularly beneficial electronic configurations at these positions.

These investigations will be presented in detail in Chapters 5-8, while Chapters 2-4 provide essential information regarding electrocatalysis, the investigated reactions, and the n-EC-STM technique. As an outlook, the importance of the electrolyte components is briefly elaborated in Chapter 9. Overall, this thesis explores the versatility of n-EC-STM and demonstrates its ability to observe the active sites directly under reaction conditions on specific model systems. It will be shown that with this *in-situ* approach, concrete guidelines for catalyst design can be obtained in a straightforward way. This is a particularly important feature in light of the pressing climate issues and the necessary transition towards a sustainable energy economy.

## 2 Fundamentals of Electrocatalysis

Wilhelm Ostwald, who was among the first to perform extensive research on catalysis, formulated the following basic definition for the phenomenon: “[Catalysis is] the acceleration of chemical reactions by the presence of foreign substances which are not consumed”.<sup>[55][56]</sup> This is achieved by a lowering of the activation energy of the reaction (Figure 2.1A) and sometimes by additionally altering the reaction mechanism to a more favorable pathway (Figure 2.1B). In this thesis, the focus will be on catalysis at the electrified solid/liquid interface. To increase a reaction rate in such a configuration, it is necessary to optimize the activity of the catalyst. This largely depends on the temporary binding of reactive species to the catalyst surface. Since the local arrangement and composition of surface structures can influence the binding properties, identification and characterization of the most active sites have become a focal point of experimental and theoretical studies in electrocatalytic research. This is typically done by using well-defined model systems with *e.g.* only a few different structural motifs to allow concrete conclusions which can subsequently be transferred to maximize the efficiency

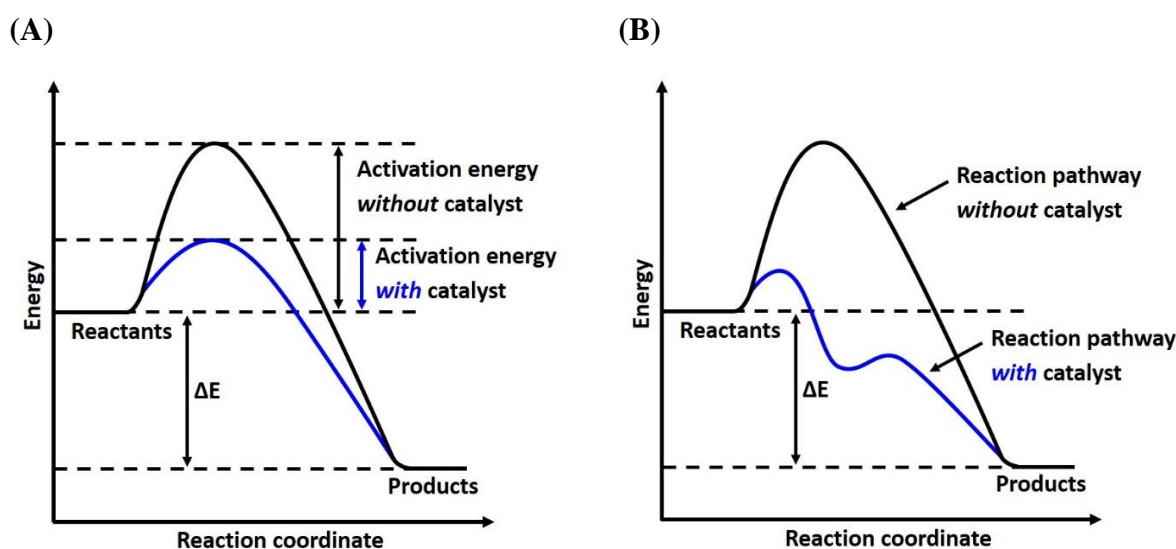


**Figure 2.1** The effect of the catalyst on a reaction. (A) The catalyst lowers the required energy to perform the reaction. The catalyst is not consumed in the reaction. (B) The reaction mechanism is altered by the catalyst. This can for example imply different intermediate states along the reaction pathway. Adapted from Ref. [166].

in practical applications. Along these lines, in this thesis, the structure-activity relationships of several model systems are characterized using the *in-situ* technique.

This Chapter will introduce the fundamental electrochemical principles that provide the framework for the electrocatalytic studies in this thesis. Further, the consequences of the Sabatier principle and the concept of active sites in the scope of heterogeneous catalysis at the electrified solid/liquid interface will be discussed.

### 2.1 Composition of the Electrified Electrode/Electrolyte Interface

The main focus of this thesis is concerned with reaction processes at a heterogeneous interface, specifically the solid/liquid interface between an electrode (electron conductor) and an electrolyte (ion conductor). The details of such systems can be found in standard textbooks of electrochemistry and electrocatalysis such as Refs. [57,58,59]. In the following, the essential principles required for the discussion of the results will be reviewed. At the interface between a charged electrode and an electrolyte, an electrical double layer (EDL) is formed, governing the local dynamics. First introduced by Hermann von Helmholtz, the model of the EDL has received many modifications, most prominently by Gouy, Chapman, and Stern.<sup>[57,60,61,62,63]</sup> Figure 2.2A shows a typical portrayal of the EDL. Due to the different phases of the electrode and the electrolyte, charge separation is developed at the interface. Supposing the electrode is negatively charged, the layer closest to the electrode can consist of specifically adsorbed anions and solvent molecules, *i.e.* water dipoles aligning along the electrode surface (Inner Helmholtz Plane, IHP). Solvated cations form the second layer (Outer Helmholtz Plane, OHP). With increasing distance to the electrode, the effect of the charge separation decreases (diffuse layer) until the bulk concentration is reached. Therefore, it is essential to note that changes in the electrode potential will mainly influence the area within a few nanometers from the interface.

Generally, for the examination of the electrified electrode/electrolyte interface in this study, an electrochemical three-electrode configuration was used, as sketched in Figure 2.2B. The processes at the working electrode (WE) are the subject of the investigation. The current flows between the counter electrode (CE) and the WE. In contrast to a two-electrode configuration, a

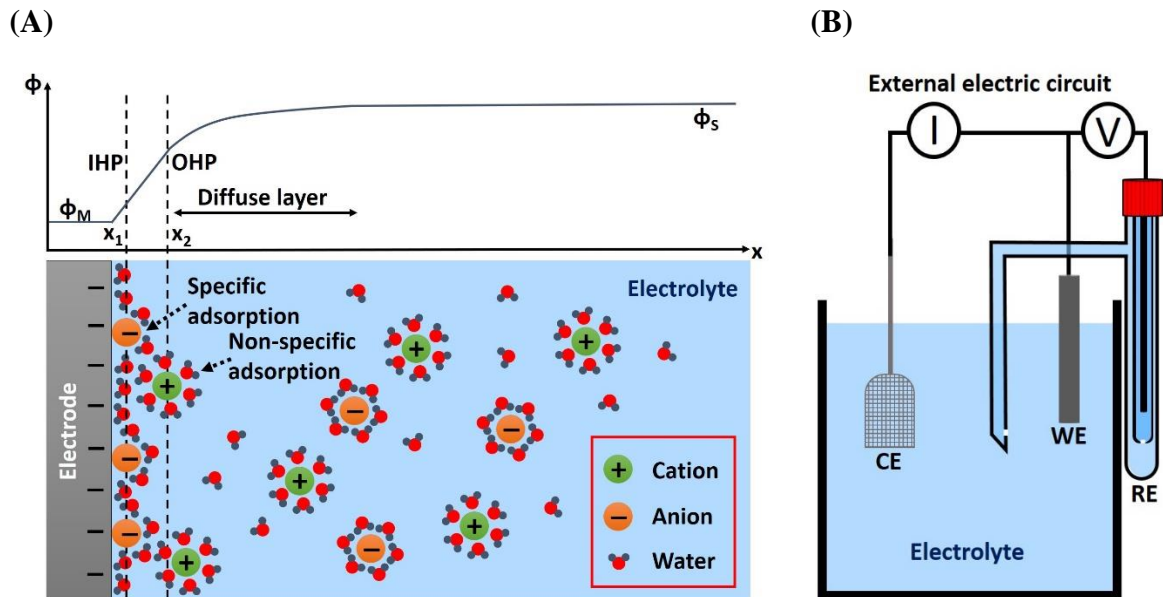


**Figure 2.2** (A) Schematic of an electrical double layer at the electrified electrode/electrolyte interface. At a negatively charged electrode (potential  $\phi_M$ ), there will be specifically adsorbed anions forming the IHP ( $x_1$ ) and non-specifically adsorbed cations composing the OHP ( $x_2$ ). After the diffuse layer, the potential stabilizes at the bulk solution level ( $\phi_s$ ). Both potential and charge density change predominantly close to the interface under the application of a potential. (B) Standard three-electrode setup for electrochemical experiments. WE, CE, and RE (electron conductors) are immersed in an electrolyte (ion conductor). An external connection closes the electric circuit. Potentials are applied with respect to the RE, while the majority of the reaction currents are passed through the counter electrode. This type of setup allows to single out and precisely analyze the processes at the WE.

third electrode, the reference electrode (RE), is introduced to the system. By measuring the potential between this neutral element and the WE, precise potential control can be achieved. In this way, the behavior of the WE can be isolated, and the performance can be compared to other electrode materials and shapes.

## 2.2 Faradaic Processes at the Electrified Electrode/Electrolyte Interface

A reaction where  $z$  electrons are transferred can be described as follows:



where  $O$  and  $R$  are the oxidized and reduced species, respectively.  $k_R$  and  $k_O$  are the rate constants of the reduction and oxidation reaction. Details on the mathematical description of their kinetics can be found elsewhere (*cf.* Refs [57,58,59]). A reaction process occurring on the electrode surface can be divided into several steps (Figure 2.3). For charge transfer to take place, the reactants need to diffuse towards the surface and adsorb. Similarly, after completion of the charge transfer, the products should desorb and diffuse towards the bulk electrolyte. The slowest of these steps is the rate-determining step of the reaction. To characterize the electrochemical behavior of an electrified electrode/electrolyte interface, cyclic voltammetry (CV) has become one of the most popular techniques. For recording a so-called cyclic voltammogram (also CV), a periodic linear sweep between the potentials  $U_{\min}$  and  $U_{\max}$  is performed (see Figure 2.4A). In the CV the current (density) is plotted as a function of applied

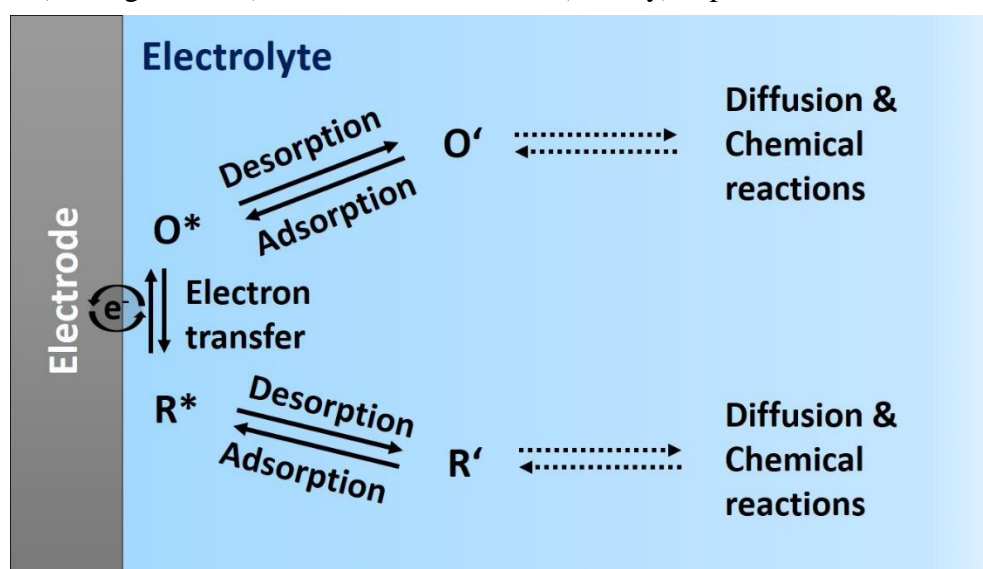


**Figure 2.3** There are several steps involved in a reaction process, such as diffusion, ad-/desorption, and electron transfer. The slowest step is the rate-determining step.

## Fundamentals of Electrocatalysis

potential. One can differentiate between the anodic scan, the current measured when the potential is linearly increased, and the cathodic scan when the potential is decreased. As a result, the changes in the current of the system can indicate at which potential faradaic and non-faradaic processes occur.<sup>[59,64,65]</sup> The exact shape of the CV depends on several factors, such as the applied potentials, the nature of the electrode and the electrolyte, the atmosphere, and the scan rate (mV/s). As an example, in Figure 2.4B, the typical CV of Pt(111) in Ar-saturated 0.1 M HClO<sub>4</sub> is given.<sup>[44]</sup> Here, the profile reveals at which potentials H, OH, and O ad-/desorption take place. The potential range with minimal current in-between the H adsorption/desorption and the OH adsorption region is denoted as the double layer. In addition, the reversibility of individual reactions can be investigated by examining the peak separation. In many cases, the CV of a material under a given set of conditions can be used like a ‘finger-print’ to ensure the presence of a clean and defect-free surface.

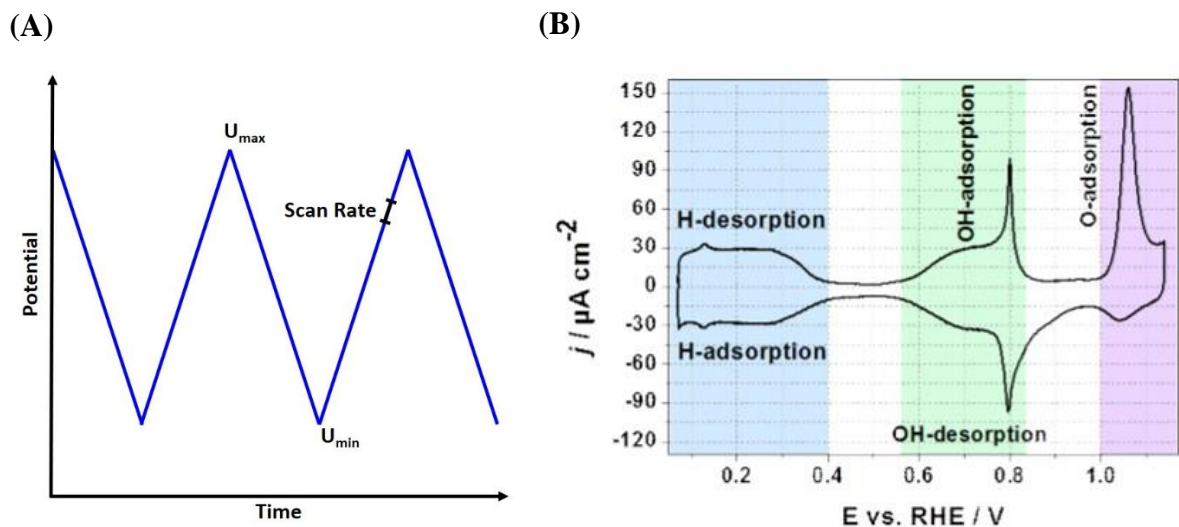


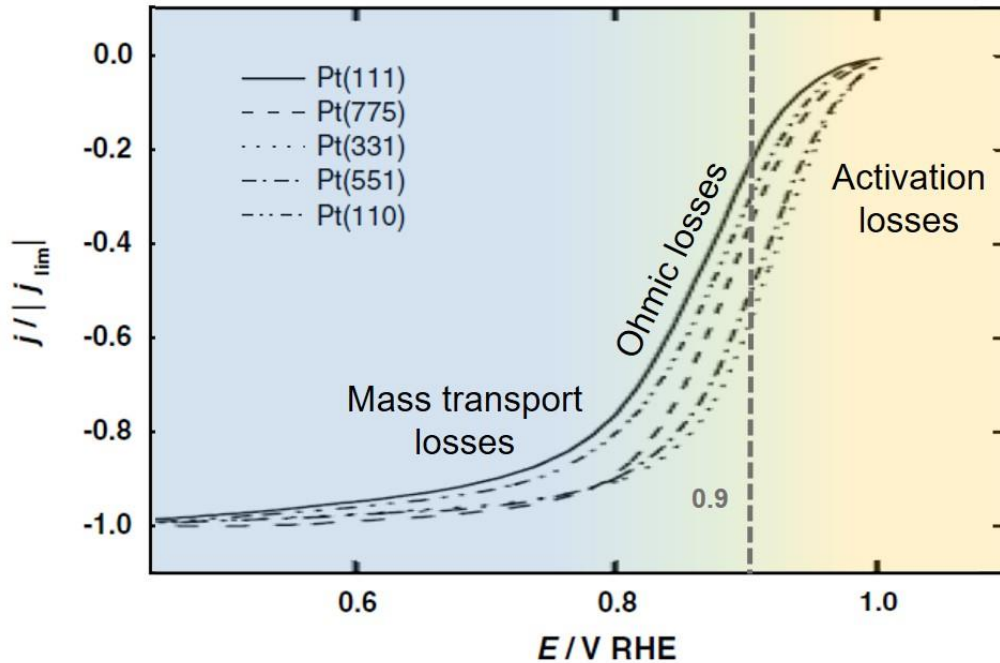
**Figure 2.4** (A) In cyclic voltammetry the potential at the WE is linearly ramped between  $U_{min}$  and  $U_{max}$ , while the current response of the system is measured. Parameters such as the scan rate and potential range have an impact on the shape of the CV. (B) CV of Pt(111) in Ar-saturated 0.1 M HClO<sub>4</sub> (scan rate 50 mV/s). The features of the CVs reveal the potentials at which ad-/desorption processes occur, as well as give hints regarding the reversibility of these mechanisms. Reprinted with permission from Ref. [44].

## 2.3 Electrochemical Evaluation of Reaction Kinetics

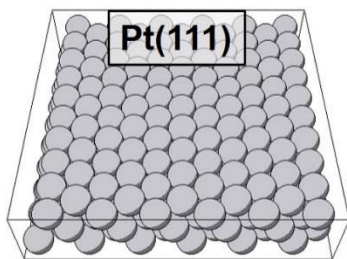
When investigating a specific reaction, it is often interesting to record a linear sweep voltammogram (LSV) of the related potential region. In this case, the potential region is only covered once instead of cycling back and forth as for the CV. The resulting polarization curve reflects the reaction kinetics and allows the comparison of different electrode structures and materials. In combination with a rotating disk electrode (RDE) setup, this is a popular way to analyze model systems under aspects such as activity, stability, and influence of temperature and electrolyte composition.<sup>[66,67,68,69,70,71,72,73]</sup> For this purpose, the electrode is mounted to a rotator which spins with typically 200 to 3000 revolutions per minute (rpm). Due to the convection created by the rotation, mass transport is facilitated, resulting in a constant thickness of the diffuse layer. In this way, the effect of factors such as electrode structure and electrolyte composition on the overall activity can be analyzed in a comparable manner. For instance, Figure 2.5A shows RDE measurements of various Pt facets in the ORR range.<sup>[76]</sup> For the measurements, the electrolyte (0.1 M HClO<sub>4</sub>) was saturated with oxygen, and the rotation speed was set to 1600 rpm. In general, three main factors negatively influence the performance: activation losses, Ohmic losses, and mass transport losses.<sup>[74,75]</sup> The activation losses are caused by the energy barrier that needs to be overcome for the reaction to occur, which strongly affects the efficiency at low current densities. This is where the catalysts play a crucial role by lowering the activation energy and altering the reaction pathway. In this example, the RDE measurements reveal that the current density at the benchmark potential 0.9 V vs the reversible hydrogen electrode (RHE) is positively influenced by a higher step density on the electrode surface (*cf.* Figure 2.5B-D, where models of Pt(111) – low step density, Pt(775) – medium step density, and Pt(331) – high step density, are displayed).

Ohmic losses are connected to the resistance of the system, causing a mostly linear decrease of the performance in the entire potential range. Here, especially the ion conduction mechanism in the electrolyte and electrical contact resistances are restricting factors. At high current densities, mass transport issues start to significantly influence the efficiency negatively, as the reactive species are not able to quickly reach/free-up adsorption sites on the surface. For this reason, at a certain potential, the limiting current is reached.

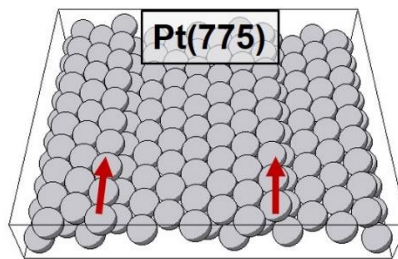
(A)



(B)



(C)



(D)

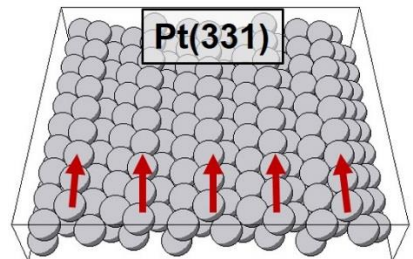


**Figure 2.5** (A) Oxygen reduction LSV measurements of several Pt facets recorded with an RDE setup (in oxygen saturated 0.1 M HClO<sub>4</sub>, 50 mV/s scan rate, 1600 rpm rotation speed). Here, the differences in the curves illustrate the effect that surface structures can have on the electrocatalytic activity. The main factors influencing the performance are activation losses, Ohmic losses, and mass transport losses, as indicated. Adapted with permission from Ref. [76] Copyright © 2007, Elsevier. (B-D) Models of three Pt facets with different step densities (steps are marked by red arrows). In combination with the LSV curves in (A), a relation between step density and catalytic performance can be asserted. The models were rendered using Ref. [77].

## 2.4 Binding of Reaction Intermediates at the Catalyst Surface

As evident in Figure 2.5, the nature of the electrode surface influences the reaction rate. To explain the differences in the reaction kinetics at catalyst surfaces, the key aspect is their ability to bind the reaction intermediates. As previously stated, according to the Sabatier principle, the bond strength regarding the reaction intermediates should be neither too weak nor too strong.<sup>[28]</sup> Otherwise, the reaction rate will be limited by the poor adsorption or desorption of the reactants or the products. In the search for the best catalytic materials, it is therefore of great interest to find the materials with optimal binding conditions for a specific reaction. The most common way to obtain binding energies for electrocatalytic systems features density functional theory (DFT) calculations.<sup>[45,78]</sup> In general, DFT is an attempt to describe and predict the behavior of many-body systems using a theoretical approach. In principle, such systems can be represented by the Schrödinger equation. However, solving the equation exactly is not practicable or even not nowadays possible for complex systems with many degrees of freedom. For this reason, Kohn developed a framework for the approximation of the solution, which is based on two theorems (Hohenberg-Kohn theorems).<sup>[79]</sup> According to the first theorem, the energy and the density of the system are related in the ground-state. As a consequence, instead of the 3n-coordinates of the n electrons in the system, there are only three degrees of freedom left. The second theorem introduces a so-called functional for the energy density of the system, which is minimized in the ground-state. With these theorems, the energy of the many-body system can be described as:<sup>[79]</sup>

$$E = \int v(\mathbf{r}) \underbrace{\rho(\mathbf{r})}_{\text{electron density}} d\mathbf{r} + \underbrace{F[\rho(\mathbf{r})]}_{\text{functional of the electron density}} \quad 2.2$$

This function can be solved considering that it has its minimum in the system's ground state. The first term describes the influence of an external field  $v(\mathbf{r})$ , *e.g.*, caused by atomic nuclei. The second term is the functional of the electron density. As the name already suggests, these functionals are the heart of DFT calculations, as they determine the accuracy of the solution. There are several approaches for the construction of functionals, such as the simpler local spin density approximation (LSDA),<sup>[80]</sup> more complex ones such as the generalized gradient approximation (GGA),<sup>[81,82,83,84]</sup> and highly complex ones such as hybrid functionals.<sup>[85,86,87,88,89]</sup>

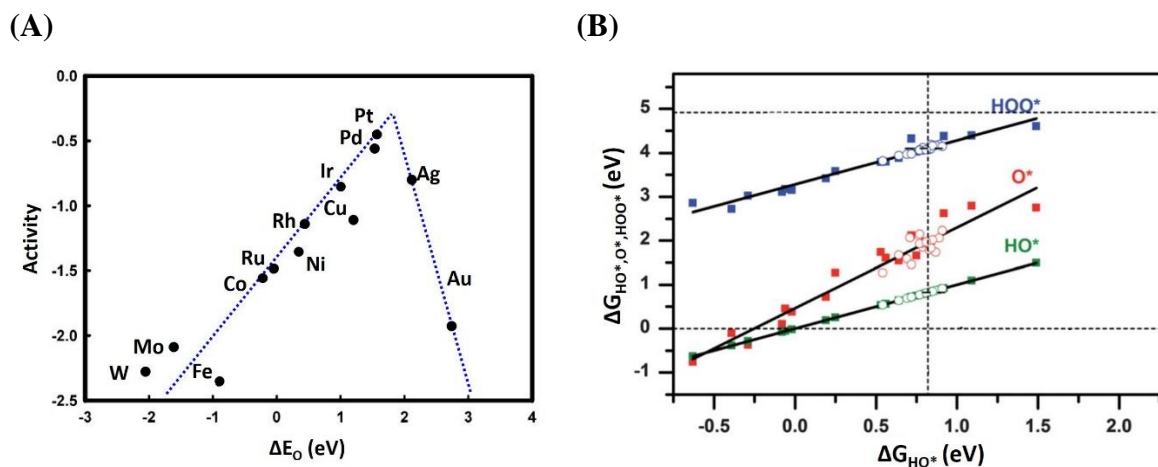


**Figure 2.6** (A) Volcano plot for the ORR, based on DFT calculations for the binding energy of oxygen on several metal surfaces. The blue line indicates a theoretical trend with optimal bond strength at the apex. The predictions from DFT calculations are a valuable guide for the experimental identification of the most active sites. Adapted with permission from Ref. [30]. Copyright © 2004, American Chemical Society. (B) Scaling relations of  $HO^*$ ,  $O^*$ , and  $HOO^*$  on metal (squares) and Pt-overlayer on Pt-alloy (open circles) surfaces. These relations form a major restriction for complex processes which involve several reaction intermediates since the improvement of one bond can negatively influence another. Adapted with permission from Ref. [90]. Copyright © 2012, Royal Society of Chemistry.

It is essential to keep in mind that complex functionals can result in more accurate solutions. However, they also require more computational capacity.

In electrocatalysis, the DFT approach is usually employed to model the interaction between catalyst surface and reaction intermediates.<sup>[45,78,91,92,93,94,95,96,97]</sup> Often, results of the DFT calculations are represented in a Sabatier-type volcano plot which classifies the materials by the binding of a reaction intermediate and a measure of activity such as the overpotential (the required potential difference to drive the reaction compared to the equilibrium potential) or current density.<sup>[30]</sup> An exemplary volcano plot for the ORR is shown in Figure 2.6A. The blue line serves as a guide to the eye, indicating the theoretical trend. A major objective of electrocatalytic research is to find materials close to the apex of the imagined volcano, where reaction species are bound optimally. DFT calculations allow relatively fast screening of potential catalysts and can therefore be an important support for experimental studies.<sup>[31,98,99,100]</sup>

It is important to note that in complex processes such as the ORR, the maximal efficiency of a catalyst is limited by the relation of the binding of the reaction intermediates to surface sites. This is often expressed in scaling relations such as Figure 2.6B, which shows that the binding of reaction intermediates on metal surfaces scales linearly.<sup>[90]</sup> It implies that improving the binding of one reaction intermediate can have a negative effect on the binding of another, limiting the overall achievable efficiency.

Although DFT calculations are a powerful tool for the prediction of electrocatalytic properties, there are several drawbacks related to this theoretical approach. Due to the complexity of the studied systems, many simplifications have to be conceded to run the simulations. Most often, the influence of the electrolyte/solvent can only be considered to a certain degree or somewhat neglected.<sup>[34][101]</sup> Furthermore, a site with the lowest calculated overpotential does not necessarily translate as the most active site.<sup>[32]</sup> Consequently, experimental approaches for the identification of active or most active sites are required to substantiate the understanding of catalysts.

## 2.5 Overview of Experimental Techniques for the Identification of Active Sites

Recently, several experimental techniques have been developed or adapted to facilitate the search for the most active sites on catalyst materials.<sup>[46,102,103]</sup> In comparison to the previously introduced RDE analysis, which tests the entire catalyst surface, the point of these techniques is to probe the sample more locally to identify the structural motifs behind the activity.

Parts of this chapter are based on the publication:

*Hou, S.<sup>1</sup>; Kluge, R. M.<sup>1</sup>; Haid, R. W.<sup>1</sup>; Gubanova, E. L., Watzel, S. A.; Bandarenka, A. S. and Garlyyev, B. A review on experimental identification of active sites in model bifunctional electrocatalytic systems for oxygen reduction and evolution reactions, *ChemElectroChem* **2021**, *8*, 3433-3456.<sup>[46]</sup>*

## Fundamentals of Electrocatalysis

A prevalent example of such an approach is X-ray absorption spectroscopy (XAS).<sup>[104,105,106,107,108]</sup> In this case, an X-ray beam is used to probe the sample (*cf.* Figure 2.7A). The energy of the photon beam is gradually varied to cover a wide energy range. At certain energies, the photons will excite the inner shell electrons of the sample to a higher level. Thus, by monitoring the intensity of the beam transmitted from the sample, the existing energy states can be analyzed. The XAS spectrum consists of the extended X-ray absorption fine structure

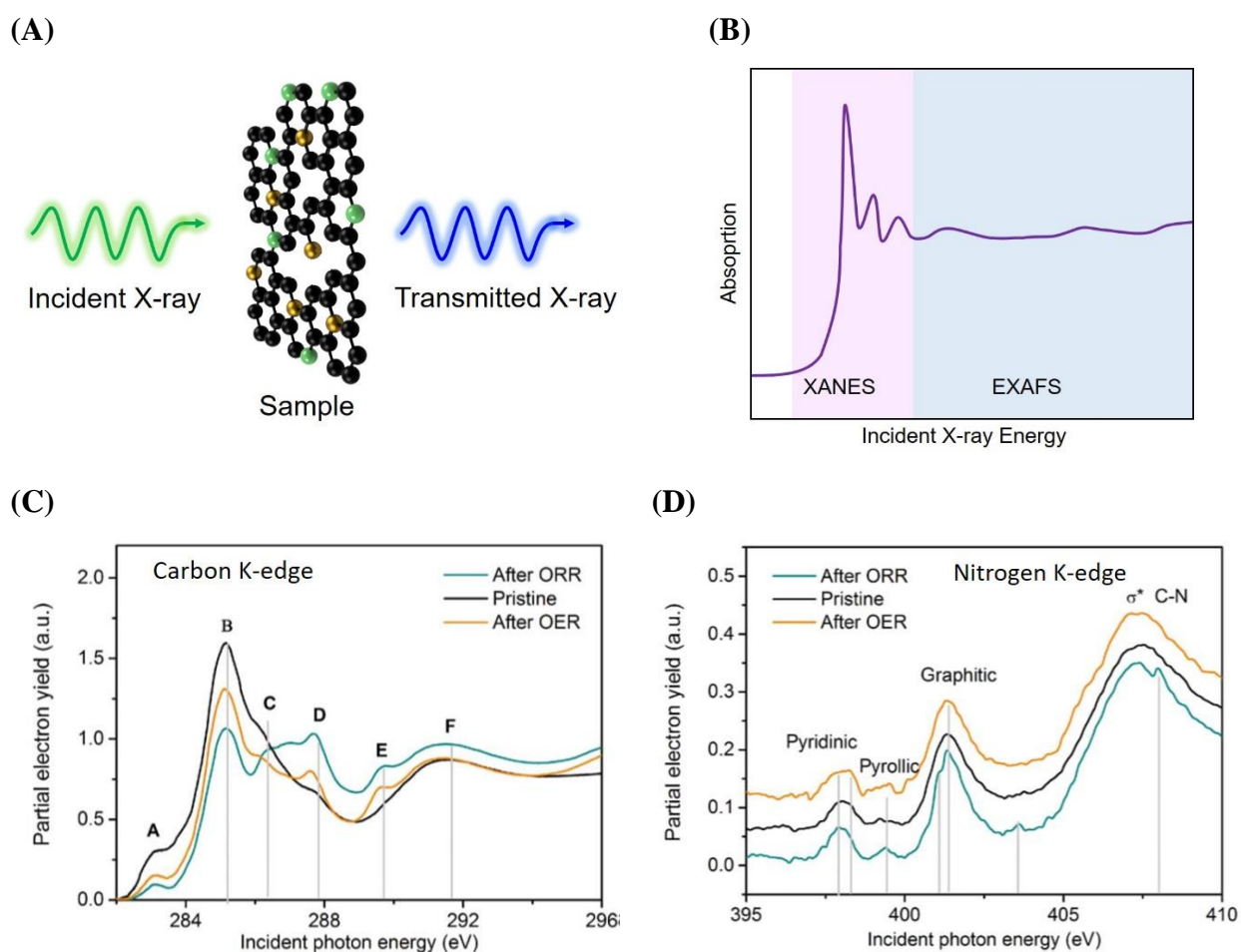


**Figure 2.7** (A) During XAS, the sample is probed with an X-ray beam within a certain range of energies. The intensity of the transmitted beam reflects the energy states of the electrons in the sample. (B) The XAS spectrum consists of the EXAFS and XANES sections. Particularly, variations of the peaks in the XANES spectrum indicate adsorbate-sample interactions. (C) Carbon K-edge and (D) nitrogen K-edge XANES spectra of an N-doped graphene catalyst. Changes in the peaks after ORR and OER compared to the pristine sample were caused by adsorption of reaction intermediates, and thus led to the identification of the active doping configurations. (C) and (D) Adapted with permission from Ref. [106]. Copyright © 2016, AAAS.

(EXAFS) and the X-ray absorption near edge structure (XANES, see Figure 2.7B). Particularly the latter can be taken advantage of in electrocatalysis to obtain information about the adsorbed species at the electrode surface. For instance, Yang *et al.* utilized this technique to study an N-doped graphene catalyst.<sup>[106]</sup> Comparing the carbon and nitrogen K-edge XANES spectra (Figure 2.7C and D, respectively) of the pristine sample to the ones after ORR and after OER, they were able to observe slight variations in the position and height of the peaks. These can be connected to modifications of the electronic structure due to the adsorption of reaction intermediates. Specifically, the peaks at 287.7 eV and 289.6 eV in Figure 2.7C served as evidence of O and OOH adsorption during both reactions. Furthermore, the peaks in Figure 2.7D at 398.0 eV after the OER and at 401.0 eV after the ORR hinted at the nature of the active

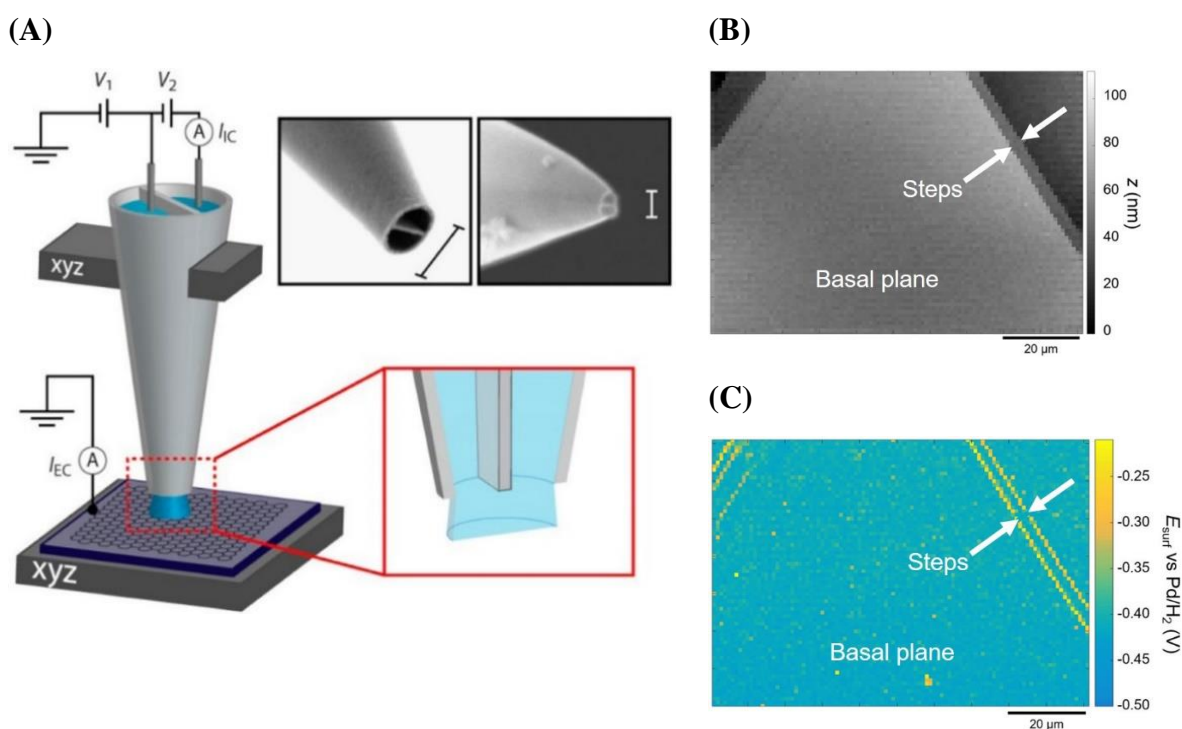


**Figure 2.8** (A) Working principle of SECCM measurements. A capillary containing electrolyte and RE/CE electrode is scanned over the sample, connected by an electrolyte meniscus. The measured current density reflects the activity of the probed area, and thus, active centers can be determined. Reprinted with permission from Ref. [112]. Copyright © 2016, American Chemical Society. (B) Topographic and (C) electrochemical image of a  $\text{MoS}_2$  surface under HER conditions. A comparison of the two datasets revealed a high HER activity along the step edges. Reprinted with permission from Ref. [113]. Copyright © 2019, American Chemical Society.

sites. Based on these observations, the authors concluded that the active configurations for this system are the n-type doping for the ORR and the p-type doping for the OER.

A more direct approach to visualize catalyst activity was developed by Unwin *et al.*, scanning electrochemical cell microscopy (SECCM).<sup>[109,110,111,112,113,114]</sup> In this case, a miniaturized electrochemical cell was designed to probe the WE surface (*cf.* Figure 2.8A).<sup>[112]</sup> For this purpose, a capillary holding the electrolyte solution and the reference/counter electrode was connected to the sample surface *via* an electrolyte meniscus. As a consequence, the catalytic behavior of an area as small as the contact between probe and sample can be analyzed. By scanning the ‘cell’ across the electrode, an electrochemical map of its surface can be rendered. A higher current density revealed active areas compared to non-active areas. For example, Figure 2.8B shows the topography of a molybdenum disulfide (MoS<sub>2</sub>) surface, and Figure 2.8C the corresponding SECCM image under HER conditions.<sup>[113]</sup> A comparison of the images revealed an enhanced HER activity along the step edges.

Another interesting approach for the experimental identification of active sites is electrochemical tip-enhanced Raman spectroscopy (EC-TERS).<sup>[115,116,117,118,119,120]</sup> Here, the sample surface is scanned using an STM setup, while simultaneously performing Raman spectroscopy at the position of the scanning tip (see Figure 2.9A for a sketch of the setup).<sup>[115]</sup> For this purpose, a laser illuminates the tip, which amplifies the intensity due to plasmon interaction.<sup>[121,122,123]</sup> The recorded signal from Raman scattering of the photons then reveals information about the energy levels of the electrons in the chemical species at that position. Performing this experiment in an electrochemical setup allows control over the reactions at the surface, and consequently, the technique can be used to probe the catalyst-adsorbate interaction at specific sites. By smart experiment design, not only the active sites can be identified but even information about the reaction mechanism can be obtained.<sup>[115,116,124]</sup> Recently, this technique was applied by Pfisterer *et al.* to analyze the water splitting at defects of a roughened Au(111) crystal in 0.1 M H<sub>2</sub>SO<sub>4</sub>.<sup>[116]</sup> Figure 2.9B shows the STM image of the surface, and Figure 2.9C is a corresponding map of the Au oxide (AuOx) peak intensity in the TERS signal. During the image, the potential was switched to allow (ON) and suppress (OFF) water splitting, as indicated. In the ON state, the Raman signal showed clear evidence of activity at the defect-rich surface.

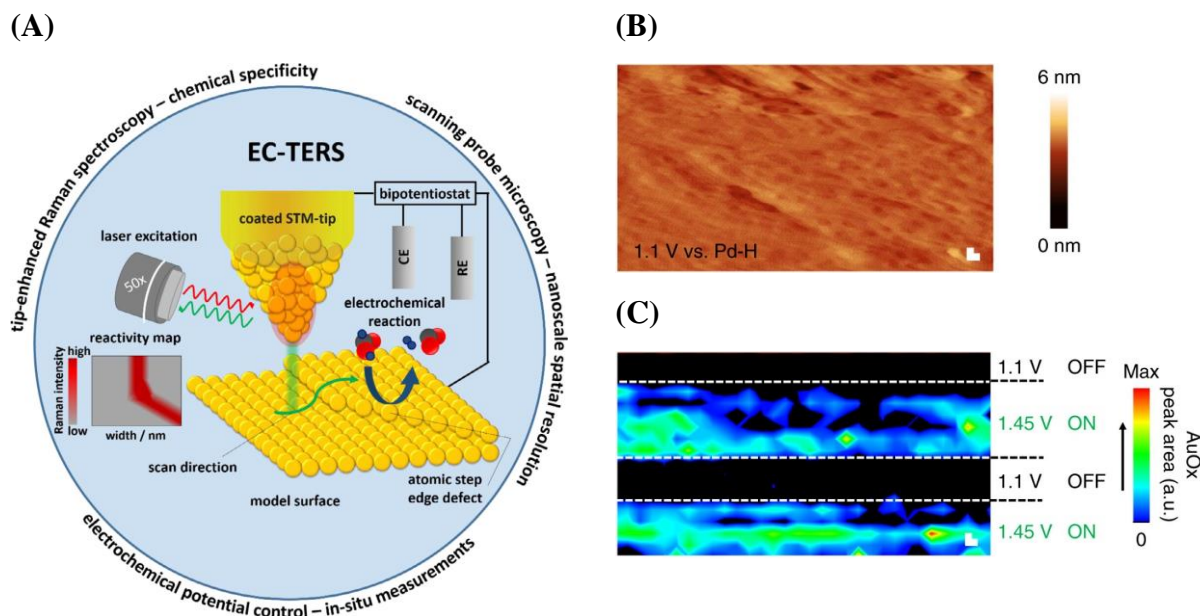


**Figure 2.9** (A) EC-TERS technique for identification of active sites. The STM tip is used as an antenna for Raman spectroscopy by illumination with a laser. At the same time, it maps the electronic structure of the surface. The obtained information can be linked to active sites and the reaction mechanism. Reprinted with permission from Ref. [115]. Copyright © 2018, Elsevier. (B) STM image of a roughened Au(111) single crystal. (C) Corresponding Raman response of the AuOx peak, confirming water splitting activity at the ON potential. Reprinted with permission from Ref. [116]. Copyright © 2019, The Authors.

All of the mentioned techniques have their advantages and disadvantages. For instance, XAS is a powerful tool to probe adsorbate-sample interaction. However, the X-ray transmission restricts the thickness of the sample. The SECCM technique can evaluate the topography and electrochemistry of an electrode surface, but the resolution is limited by the size of the aperture of the capillary ( $\sim 500$  nm). Similarly, the resolution of the EC-TERS is reduced by the bifunctional use of the tip as a Raman antenna and STM probe. Besides, the experimental setup of the techniques is complex, requiring *e.g.* the adjustment of the X-ray or laser beam in liquid for the *in-situ* analysis. In this light, the central technique of this thesis, the n-EC-STM, offers several advantages for the identification of active sites. It makes use of a conventional EC-STM setup with uncomplicated access to the electrodes and electrolytes. A particular strong point of the approach is the ability to probe the activity of specific surface sites down to atomic resolution. A detailed introduction to this approach is given in Chapter 4.

### 3 Model Catalytic Reactions

In this work, the focus is mainly set on electrocatalytic processes involved in hydrogen fuel cells, water electrolyzers, and metal-air batteries. The first of those devices, the fuel cell, is seen as a promising solution for mobile energy provision, *e.g.*, in cars, busses, and planes.<sup>[7][8][125]</sup> Figure 3.1A illustrates an (alkaline) hydrogen fuel cell, which uses molecular hydrogen and oxygen to produce an electric current. A clear advantage of this process is that the only ‘waste’-product from this reaction is water.<sup>[74]</sup> While oxygen can be readily obtained from the air, hydrogen is not abundantly available in an unbound form. Consequently, there is a need to produce it electrochemically. Here, the second of the above-listed devices, the electrolyzer, comes into play. Essentially, the water electrolyzer (*cf.* Figure 3.1B) splits  $\text{H}_2\text{O}$  into its components, yielding  $\text{O}_2$  and, more importantly,  $\text{H}_2$ .<sup>[9][126]</sup> As detailed in the introduction,

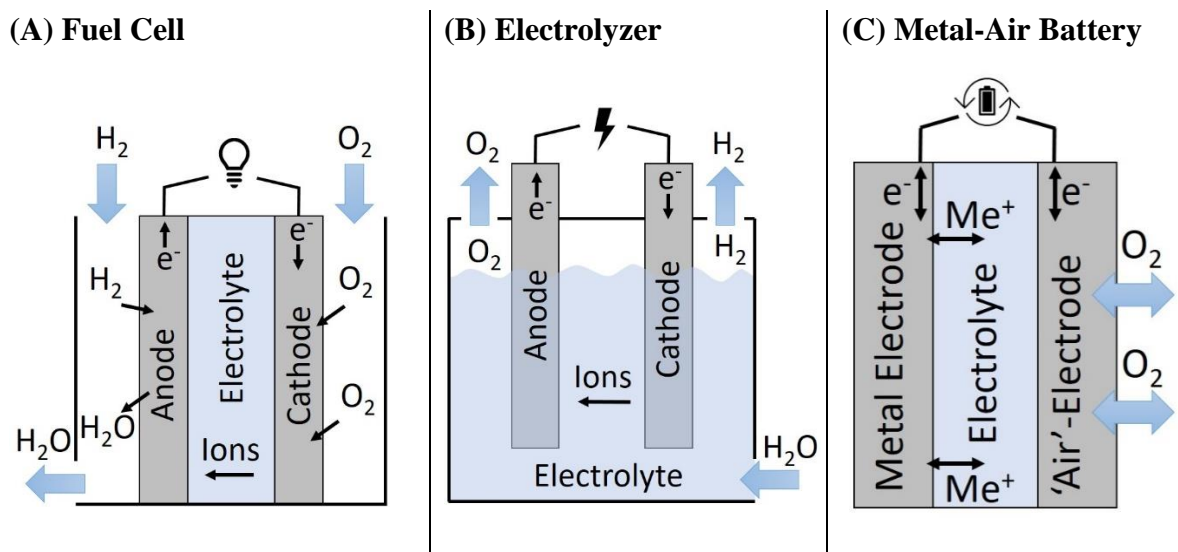
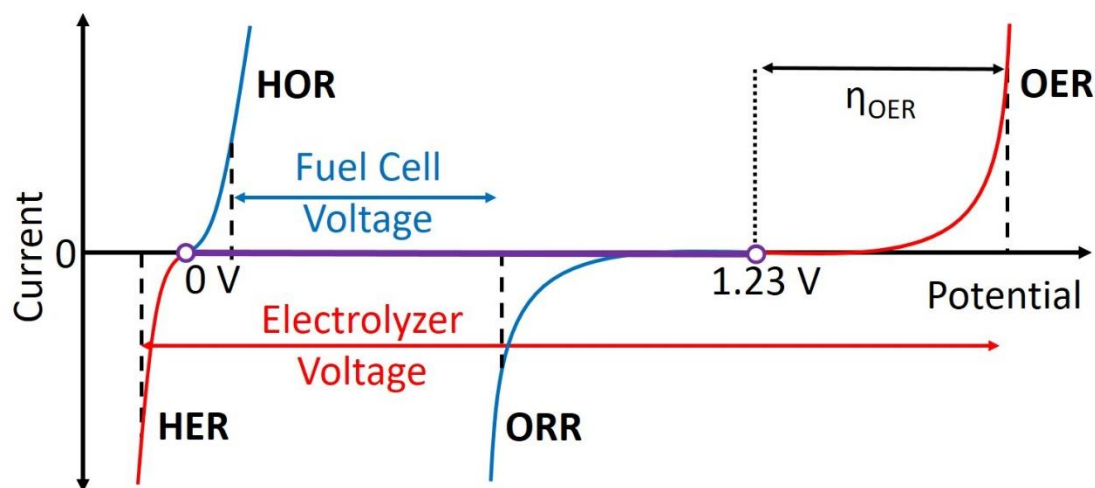


**Figure 3.1** Schematic of important energy devices. (A) In the (alkaline) hydrogen fuel cell, hydrogen and oxygen are used to generate an electric current. This could be an ideal method for ‘clean’ mobile energy provision. (B) The (alkaline) water electrolyzer produces molecular oxygen and hydrogen. Hydrogen is particularly valuable due to its critical role in sustainable energy schemes. (C) The metal-air battery is composed of a metal electrode and a so-called ‘air’-electrode, connected by an electrolyte. The ‘air’-electrode allows oxygen from the surroundings to diffuse in and out of the bulk. During the charge and discharge of the battery, the oxygen is, respectively, evolved and reduced at this electrode.

in order to achieve a sustainable, environmentally friendly energy strategy, the required current to drive the electrolyzer reactions could be provided from renewable sources.

(A)



(B)

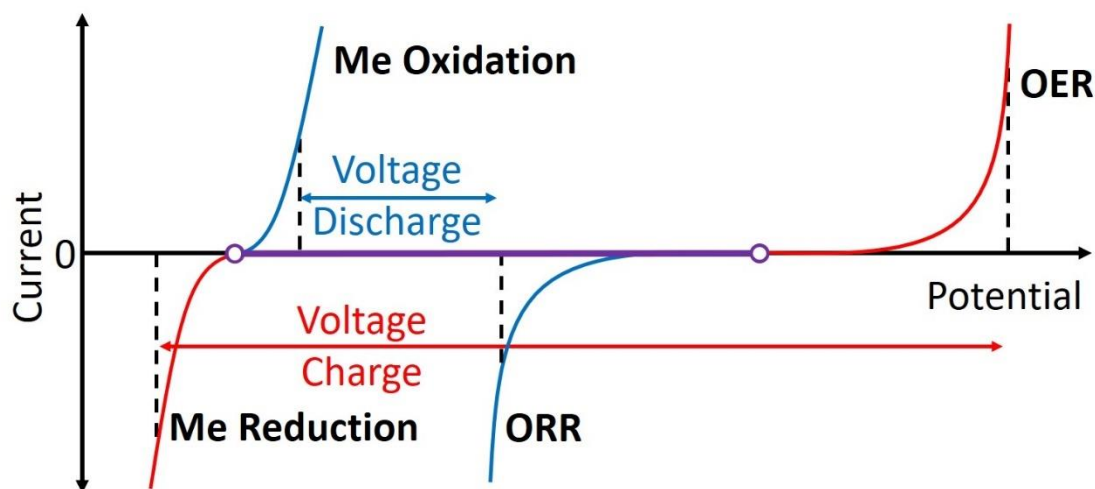


**Figure 3.2** Schematic polarization curves for (A) the hydrogen fuel cell and water electrolyzer reactions and (B) the metal-air-battery reactions. Moving the voltages closer to the potential difference between the equilibrium potentials (indicated in purple), while still obtaining high currents is a key objective of electrocatalysis. As evident from the figure, especially the large overpotential ( $\eta$ ) necessary to drive the ORR and OER is a critical issue. Regarding the HER, an important matter is a shift from precious-metal-based catalysts to more sustainable and economical alternatives such as carbon. Adapted with permission from Ref. [127], Copyright © 2016, Springer Nature; and Ref. [128], Copyright © 2010, John Wiley and Sons.

The third of the mentioned devices, the metal-air battery, is based on a charge-discharge cycle between a metal electrode (typically Li, Na, Zn, etc.) and a porous ‘air’-electrode (*cf.* Figure 3.1C). During the discharge, the so-called ‘air’-electrode uses the oxygen from ambient air to generate an electric current. On the other hand, during the charging process, it needs to be able to produce oxygen. Thus, this type of battery requires bifunctional materials with high efficiencies for both the ORR and OER. <sup>[12][129][130]</sup>

Figure 3.2 gives a schematic overview of the kinetics of the reactions involved in these devices. As is evident, the fuel cell/electrolyzer voltages (Figure 3.2A), as well as the metal-air battery charge/discharge voltages (Figure 3.2B), are far from the theoretical maximum (indicated in purple).<sup>[127,128]</sup> To get closer to the optimum, increasing the efficiency of the catalyst materials is paramount. However, it is important to also keep in mind other conditions of catalyst design such as durability, selectivity, abundance, and cost. In this thesis, several key reactions, specifically the HER, ORR, and OER, were examined considering these aspects. For simplicity, the subsequent discussion of these processes focuses on the reaction pathways in the electrolyte conditions used in the experiments, *i.e.*, alkaline and/or acidic.

### 3.1 Acidic Hydrogen Evolution Reaction

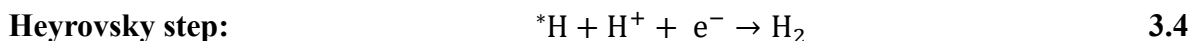
The overall reaction of the HER in acidic media is as follows:



It is widely accepted that this reaction can occur following two mechanisms, as illustrated in Figure 3.3A.<sup>[131][132]</sup> In both cases, the first step (Volmer step) is the adsorption of hydrogen to the electrode surface:



Here, \*H represents adsorbed hydrogen. To form hydrogen gas, the \*H can combine either with another \*H nearby (Tafel step) or with a proton from the electrolyte and an electron from the electrode (Heyrovsky step):



Notably, the mechanism involves only one bound intermediate ( $*\text{H}$ ). Therefore, the performance of the catalyst materials hinges mainly on the binding of hydrogen.<sup>[131][133]</sup> Ideally, the ad- and desorption of the reaction intermediate to the electrode is balanced, binding neither too weak nor too strong. This is reflected in the volcano plot in Figure 3.3B, where the best performing metal catalysts can be found at the tip of the volcano.<sup>[133][134]</sup> As is evident, platinum group metals show the highest activities towards the HER. However, to avoid using these rare and expensive materials, there is a growing interest in using carbon-based alternatives.<sup>[131][135][136]</sup> Designing such carbon-based catalysts with activities competitive with state-of-the-art precious metal catalysts requires a detailed understanding of the nature of the active sites.

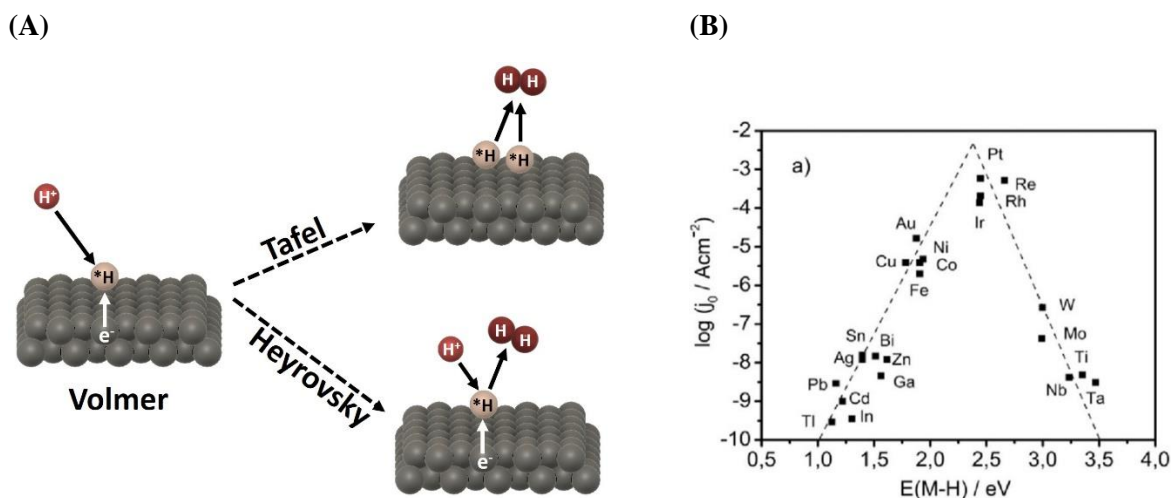
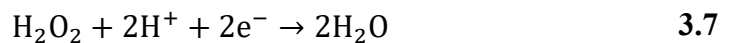
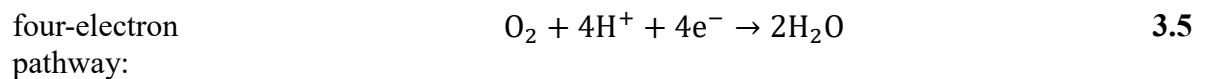


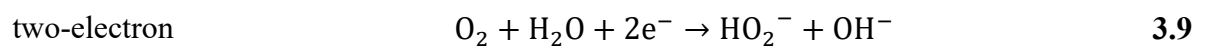
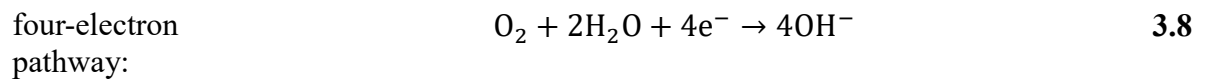
**Figure 3.3** (A) Illustration of the HER reaction mechanisms in an acidic environment. In the Volmer step, a proton adsorbs to the surface. In the Tafel step, two  $*\text{H}$  combine to form  $\text{H}_2$ . Alternatively, in the Heyrovsky step, an  $*\text{H}$  can combine with a proton and an electron to produce  $\text{H}_2$ . (B) Volcano plot for the HER in acidic media. An optimal catalyst balances the ad- and desorption of hydrogen. At the tip of the volcano, where the best catalysts are located, mainly platinum group metals can be found. Reprinted with permission from Ref. [133], Copyright © 2016, John Wiley and Sons.

### 3.2 Alkaline/Acidic Oxygen Reduction Reaction

The ORR has a standard reduction potential of 1.23 V vs the standard hydrogen electrode and is a complex process involving several reaction steps. Generally, the ORR can proceed through either a four-electron pathway or a two-electron pathway. In acidic media, these can be summarized as:<sup>[137]</sup>



As illustrated in Figure 3.4A, the four-electron pathway can proceed either through an associative (starting with the formation of  $*O_2$ ) or a dissociative mechanism (starting with the formation of two  $*O$ ).<sup>[30][138]</sup> It is believed that the two-electron pathway is less desirable due to lower efficiency and the responsibility of  $H_2O_2$  for degradation *e.g.* in the membrane electrode assembly of PEM fuel cells.<sup>[139][140][141]</sup> In alkaline media, the ORR reaction mechanisms can be written as follows:



The key issues regarding the ORR are the complicated, multi-step mechanisms along which these pathways take place. Additionally, the scaling relations mentioned in Chapter 2 become essential. Optimization of the catalyst hinges on finding the right balance regarding the binding of all reaction intermediates. The exact reaction mechanism is challenging to determine and depends on the catalyst material.<sup>[137][142]</sup>

As the volcano plot in Figure 2.6A suggests, the most active ORR catalysts typically rely on precious metals, particularly Pt.<sup>[30][142][143]</sup> Still, the required overpotentials are large, and consequently, the oxygen reduction is, in most cases, the limiting factor in energy conversion devices. Additionally, it would be desirable to move away from precious metal catalysts due to

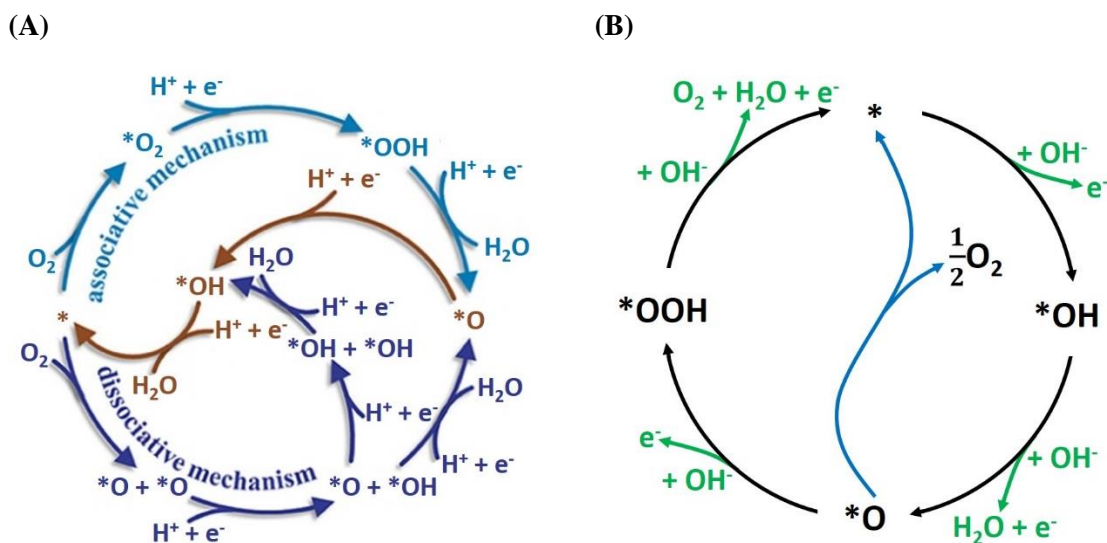


**Figure 3.4** (A) Illustration of the possible pathways of the ORR in acidic electrolytes. The complicated mechanism involving several intermediate steps is the main cause of the poor reaction kinetics. Adapted with permission from Ref. [138], Copyright © 2019, Ma, Gong, Shen, Sun, Liu, Zhang, Liu, Zhang, and Xia. (B) Reaction pathways of the alkaline OER. Like the ORR, the OER kinetics depend on the binding of several reaction intermediates, resulting in high overpotentials. Adapted with permission from Ref. [144], Copyright © 2018, American Chemical Society.

their cost and contamination issues.<sup>[142][143]</sup> There is also a specific interest in employing alkaline electrolytes, which offer less demanding conditions for the catalyst and facilitate ORR kinetics.<sup>[137,145]</sup> With these considerations in mind, it is clear that understanding the nature of the active sites for ORR electrocatalysts in both alkaline and acidic electrolytes is crucial to improving the reaction processes.

### 3.3 Alkaline Oxygen Evolution Reaction

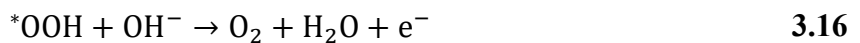
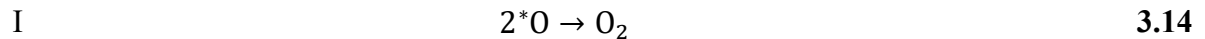
Like the ORR, its reverse reaction, the OER suffers from a complicated mechanism and, consequently, sluggish reaction kinetics. The overall reaction in alkaline media equates to:<sup>[146]</sup>



The individual reaction steps are sketched in Figure 3.4B and can be written as follows:



At this point, there are two alternative pathways:



Due to the nature of the reaction, the best performing catalysts are typically oxides. Figure 3.5 shows volcano plots for the OER on (A) metal oxides and (B) perovskite structures.<sup>[147]</sup> Again, it is important to consider the scaling relations between the reaction intermediates. In this case, it has been found that the binding energies of \*OH and \*OOH are consistently separated by 3.2 eV.<sup>[146][147]</sup> Due to this circumstance, the free energies of \*O and \*OH are sufficient as a descriptor for the intermediate binding in the volcano plots. However, it also sets a lower limit for the overpotential of 0.4 – 0.2 V.<sup>[147]</sup> Although the volcano plots are a good indicator for the electrocatalytic properties of materials, it is important to keep other aspects, such as stability, selectivity, etc., in mind. For instance, although RuO<sub>2</sub> is closer to the optimum than IrO<sub>2</sub>, the latter is seen as state-of-the-art due to higher corrosion resistance.<sup>[146,148,149]</sup> As shown in Figure 3.5B, a promising class of OER catalysts are perovskites. This class of materials possesses several advantages, such as the possibility to easily modify their properties by substitution of ions in their structure.<sup>[150]</sup> Moreover, they rely on more abundant elements compared to precious metal alternatives. Still, analogous to all mentioned reactions, it is desirable to employ completely metal-free alternatives. The use of alkaline electrolytes allows such less resistant materials to be viable options as OER electrodes. Particularly, doped carbon has been the focus of recent research.<sup>[144][151][152][153]</sup> Hence, identifying the active sites on carbon and modified carbon surfaces is essential to provide guidelines for the targeted improvement of metal-free OER catalysts.

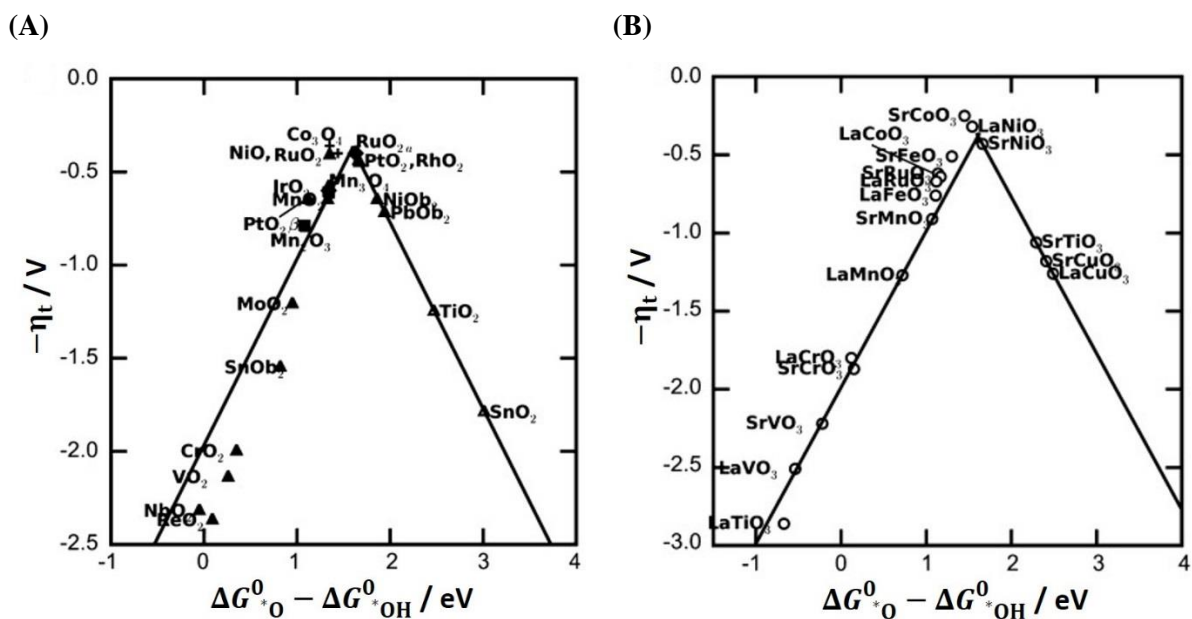


**Figure 3.5** (A) OER volcano plot of oxide materials. The best catalysts are based on precious metals. RuO<sub>2</sub> is at the peak of the curve. However, its corrosion stability is problematic. (B) Perovskite structures can be designed to produce high OER activities. Additionally, they do not require large amounts of rare elements. Adapted with permission from Ref. [147], Copyright © 2011, John Wiley and Sons.

## 4 Electrochemical Scanning Tunneling Microscopy

In his famous speech titled ‘There’s Plenty of Room at the Bottom’ at the California Institute of Technology in 1959, Richard Feynman prophesized the key role nanoscale science would be playing in the future.<sup>[154]</sup> Soon, ‘nano-technology’ became the focus of an ever-increasing amount of research. Consequently, new investigation techniques that could operate on an atomic level were required. Thus, the real start of the nano-era could be linked to the introduction of the scanning tunneling microscope, which enables the visualization of individual atom orbitals. It was pioneered and developed by Binnig and Rohrer at the beginning of the 1980s.<sup>[155,156]</sup> Their successful observation of the 7 x 7 reconstruction of Si(111) can be regarded as the first demonstration of the technique’s remarkable potential.<sup>[157]</sup> Originally intended for use in vacuum, the STM was soon adjusted for ambient conditions and, in the late 1980s, modified for experiments in liquids.<sup>[158,159,160,161,162,163]</sup> The basic principle is to measure the tunneling interaction between the sample and an atomically sharp tip. Systematically moving the tip across the sample surface at a close distance creates a conductivity map that can be related to the physical structure.

In the following, the working principle of the STM will be explained, with a focus on the operation in an electrochemical environment. Additionally, the EC-STM technique for identifying active sites is discussed in detail.

### 4.1 Scanning Tunneling Microscopy

The STM takes advantage of the tunneling current between an atomically sharp tip and the sample to probe the morphology of the surface.<sup>[48,164]</sup> In a vacuum, the tunneling current between tip and sample can be expressed as:<sup>[165]</sup>

$$I_T \propto \frac{\rho_s \rho_t V_b}{d} e^{-A\sqrt{\phi_e}d} \quad 4.1$$

Where  $A$  is a constant,  $V_b$  is the potential bias between tip and sample, and  $\phi_e$  is the effective height of the tunneling barrier.  $\rho_s$  and  $\rho_t$  are the local densities of states (LDOS) at the Fermi

level of the sample and tip, which depend on the potential bias. Furthermore, the distance  $d$  between tip and sample and the effective barrier height  $\phi_e$ , which is constant in a vacuum, play important roles. The latter is altered by the presence of a medium, such as an electrolyte, in the tunneling gap. This will become more significant in Chapter 4.1.1, describing the EC-STM working principle.

By scanning the surface with the tip at a controlled distance, a conductivity map, which can be related to the physical position of the surface atoms, can be rendered. Both tip and sample need to be at least semiconducting for this type of investigation. A typical STM setup is sketched in Figure 4.1A. The tip is moved over the sample surface in x-, y- and z-direction by piezo elements. These actuators allow precise movement even in the Angstrom region; however, they are also especially sensitive to thermal drift. This can, to a degree, be counteracted by warming the device up to its working temperature. A potentiostat provides the potential bias between tip and sample to provoke electron tunneling. The initial tunneling current is relayed to an operational amplifier which increases the signal's strength. This information is subsequently processed in the control unit (CU), which includes a feedback loop. It ensures that the tip position can be corrected based on the measured tunneling current by moving closer to or further away from the surface. In addition, the CU processes the data and converts it into an image portraying the conductivity of the surface. Due to the sensitivity of the tunneling current, a high lateral resolution can be achieved, permitting visualization of individual atom orbitals. The size of the investigated area typically ranges from a few nm to several  $\mu\text{m}$ .

Usually, STMs can be operated in two distinct modes. In the constant current mode (Figure 4.1B), the CU keeps the tunneling current consistently at a chosen setpoint, while the feedback loop is constantly readjusting the z-position of the tip. The variation of the z-axis is recorded and used to display the topography of the surface. This mode can be employed for larger-scale imaging, as it allows adjusting the tip to the surface structure. The constant height mode (Figure 4.1C) operates in a reversed manner. Here, the tip is kept at a constant height while the tunneling current is recorded. This way, the feedback loop is not needed, and faster scans can be performed.

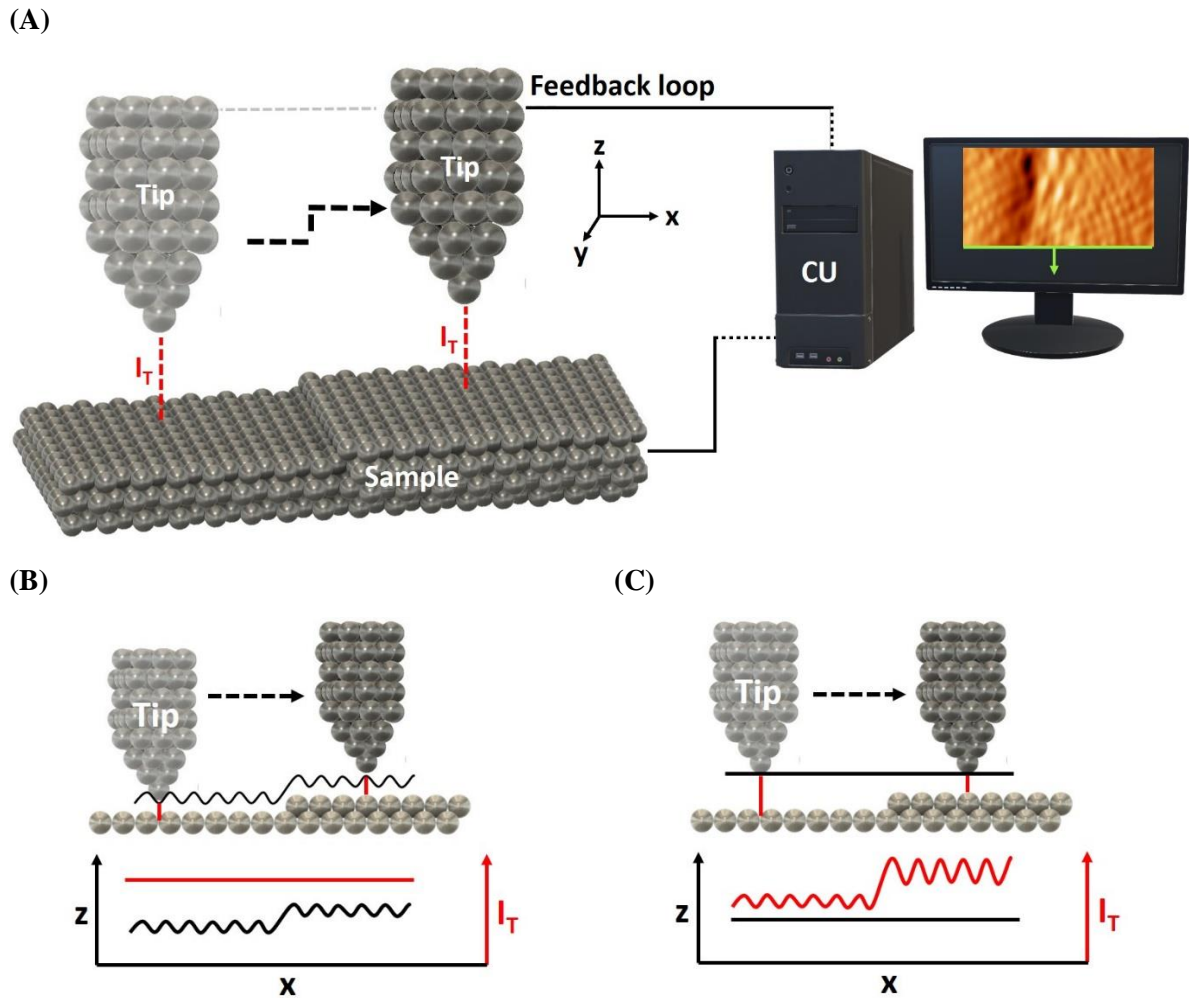


**Figure 4.1** (A) Basic STM setup. The tip is moved across the sample while the tunneling current and relative height are recorded. The CU is the central control mechanism and includes a feedback loop to ‘predict’ necessary adjustments in the z-direction. The result is a conductivity map of the sample surface, which is relatable to its topography. (B) Constant current mode. Here, the feedback loop constantly readjusts the z-position of the tip, to keep the tunneling current constant at a chosen setpoint. (C) Constant height mode. By keeping the tip at a constant height, the measured tunneling current reflects the local conductivity. Typically, this mode allows a slightly improved resolution and since the feedback loop is not needed in this mode, faster scans can be performed. On the downside, it is more likely for the tip to crash into a protruding structure.

Typically, this imaging mode allows higher resolution. However, because of the fixed tip position, the risk of crashing into a larger surface structure is increased. Therefore, it should be engaged only at relatively small scan sizes and, ideally, atomically flat surfaces. Naturally, since

the STM operates on the nanoscale and even below, the sensitivity to technical and environmental aspects is very high. The current setpoint, the potential bias, and the permitted gain of the feedback must be chosen carefully and appropriately for the investigated system. Moreover, scan size and speed need to be selected in a way that accommodates the desired results. The device itself should be isolated from vibrations and temperature changes as much as possible.

### 4.1.1 Operation in Electrochemical Environment

EC-STM allows the observation of an electrode surface while electrochemical processes are occurring. Adapting the STM for investigations in an electrochemical environment requires several modifications.<sup>[160,162,163,167]</sup> First, the sample (also the WE) needs to be mounted in an electrochemical cell which can be placed under the STM head. Figure 4.2A shows a typical EC-STM-cell, comprised of a conductive baseplate (stainless steel) and a Teflon™ ring. The sample is fastened in-between using four screws. The hole in the Teflon™ ring acts as a basin for the electrolyte. The RE and CE, connected to the STM head, are immersed into this cell. Usually, noble metal wires are used for this purpose, although other materials, such as carbon,

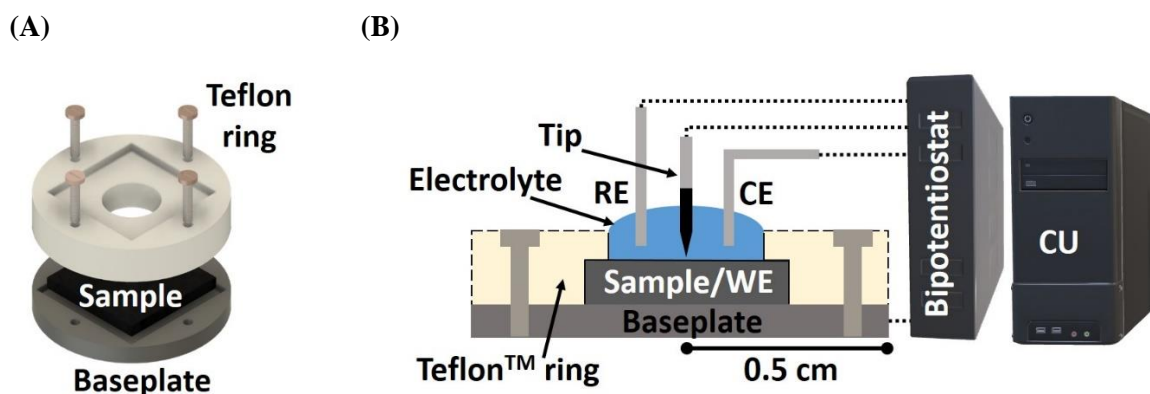


**Figure 4.2** (A) EC-STM cell. The sample is mounted between a steel baseplate and a Teflon™ ring, which holds the electrolyte. Adapted from Ref. [166]. (B) Schematic portrayal of an EC-STM setup (not to scale). The sample/WE, RE, CE, and tip are connected to a bipotentiostat, regulating *i.a.* the potential bias. The tip needs to be insulated to prevent faradaic currents. The setup allows the observation of the WE surface while electrochemical processes are occurring. Adapted with permission from Ref. [163]. Copyright © 1988 Elsevier B.V.

can be utilized.<sup>[168]</sup> The three electrodes, as well as the tip, are connected to a bipotentiostat which is controlled by the CU (see Figure 4.2B). The bipotentiostat is necessary to regulate the voltage of the four electrodes (tip, WE, RE, and CE).<sup>[167]</sup> In order to avoid faradaic currents at the tip, insulation is applied to cover all but a few atoms at the apex (for further details, please refer to Chapter 4.3.2). EC-STM has found numerous applications and, due to its high resolution, is becoming increasingly appreciated in electrocatalytic research.<sup>[47,49,50,51,115,116,169,170,171,172]</sup> In this thesis, its capability of detecting active sites under reaction conditions will be explored and applied to relevant electrochemical model systems. It is important to note that the tunneling current behaves differently in electrolytes than in vacuum or air, as discussed in more detail in the following.<sup>[173,174]</sup>

### 4.1.2 Tunneling in Electrolyte

In an EC-STM, tunneling between tip and sample occurs amidst an electrolyte. In this case, the effective barrier height in Eq. 4.1 needs to be modified to suit the investigated system. Interestingly, the barrier is lowered in a liquid environment, presumably owing to transmission via intermediate states related to the water dipoles near the tip and the sample.<sup>[175]</sup> Early studies tried to compensate for the electrolyte in the tunneling gap by generating an average  $\phi_e$  specific to the employed materials.<sup>[175,176]</sup> However, these approximations do not accurately describe the tunneling conditions. A more detailed description was found by Hugelmann & Schindler by systematic distance tunneling spectroscopy (DTS) measurements.<sup>[173,177]</sup> With this technique, the tunneling current is measured in dependence on the distance between the tip and the sample in an EC-STM. In their experiments, the same material for tip and sample (both Au) was used to ensure zero bias from the work function of the electrodes. Then, under the application of a constant potential bias, only  $\phi_e$  is left variable in Eq. 4.1 and thus it can be experimentally determined. In Figure 4.3A, an exemplary DTS measurement is shown (logarithmic scale for  $I_T$ ). The tip current was recorded at distinct points between the point of contact with the sample ( $z = 0$ ) and the Faraday regime ( $z < -1.0$  nm), where current from faradaic reactions dominates.

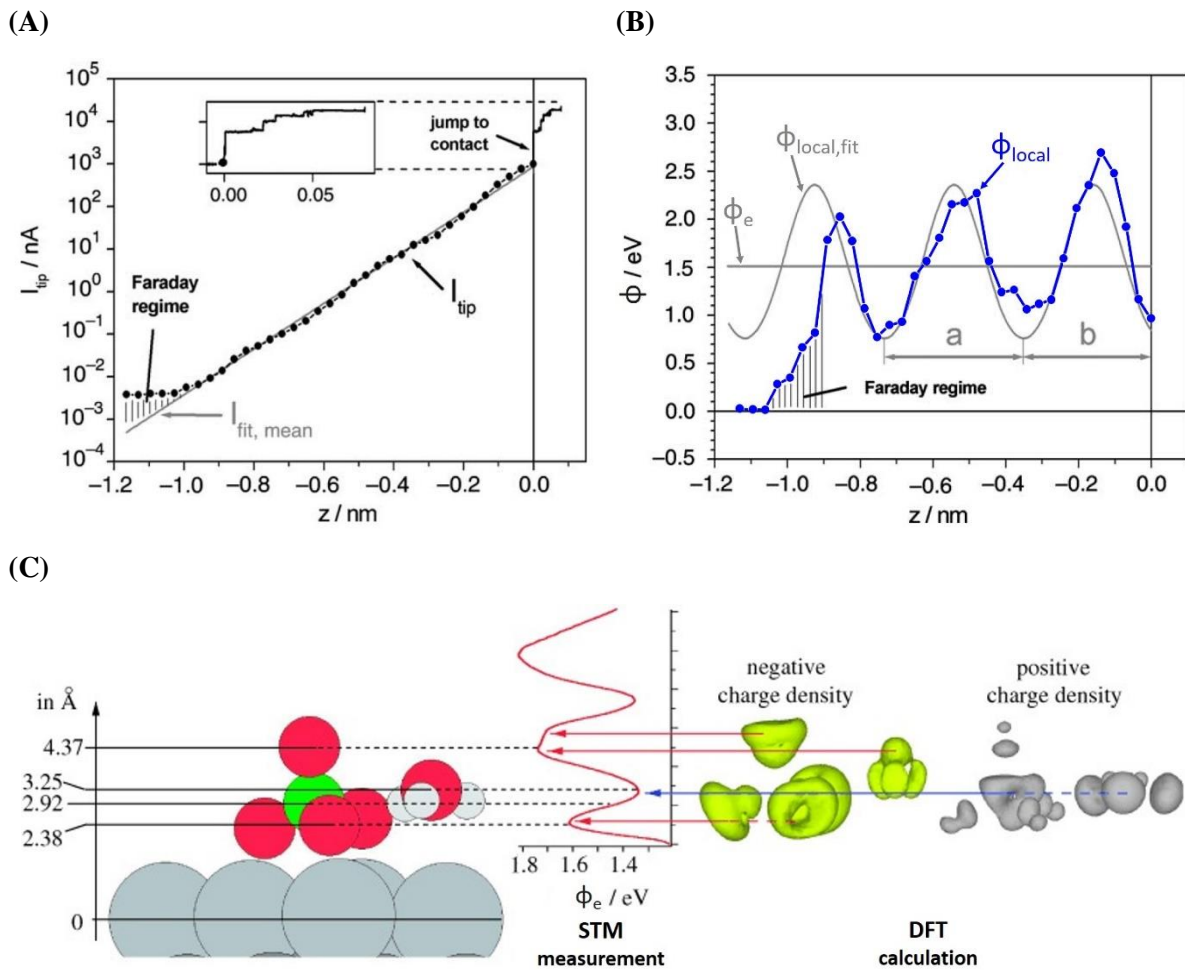


**Figure 4.3** (A) Semi-logarithmic plot of a DTS measurement between STM tip and sample (black dots). The strictly exponential dependence of tunneling current and barrier height is not given anymore (gray line). (B) The  $\phi_e$  data (blue dots), after subtraction of the exponential share, resembles a sinusoidal shape (the gray fit serves as a guide to the eye). The period of oscillation was related to the layers of water dipoles fitting into the tunneling gap. (A) and (B) adapted with permission from Ref. [173]. Copyright © 2003 Elsevier B.V. (C) Combining DTS measurements with DFT calculations explained the influence of coadsorbed sulfate and hydronium ions on the tunneling process. Maxima and minima in  $\phi_e$  were traced back to locally high positive and negative charge densities. Adapted with permission from Ref. [174]. Copyright © 2007, John Wiley and Sons.

The gray line was obtained by fitting Eq. 4.1. to the data. The strictly exponential behavior is not valid anymore. Instead, an oscillating dependence was observed. By collecting data from around 600 measurements, the following expression for the local effective barrier height in aqueous media was derived:<sup>[173,174]</sup>

$$\phi_{local} = \frac{\hbar^2}{8m} \left( \frac{\partial \ln I_T}{\partial z} \right)^2 \quad 4.2$$

Here, the factor  $\frac{\hbar^2}{8m}$  is constant and  $z$  denotes the tip-sample distance. Figure 4.3B shows a plot (blue data) created by inserting the DTS measurement in Figure 4.3A, after subtraction of the fitted exponential share of  $I_T$  (gray line in Figure 4.3A), in the above equation.  $\phi_{local,fit}$  represents a sinusoidal fit to the data, serving as a guide to the eye. The oscillations occur with a period of  $a \approx 0.35$  nm, which coincides remarkably well with the estimated size of water dipoles at the solid/liquid interface.<sup>[173]</sup> Thus, Hugelmann & Schindler suggested that the oscillatory behavior originates from the tunneling through a vacuum (increasing the barrier) and the hydrogen atoms of water molecules (lowering the barrier) depending on the number of molecules fitting within the gap. Each full period of oscillation corresponds to a completed layer of water molecules.

A separate study used this approach in combination with DFT calculations to interpret  $\phi_e$  for coadsorbed sulfate and hydronium ions on the Au(111) surface (see Figure 4.3C).<sup>[174]</sup> Here,  $\phi_e$  with respect to the distance between tip and sample was determined by STM measurements and Eq. 4.2. The minima and maxima of the resulting curve were precisely related to the calculated accumulations of positive and negative charges, confirming the significant impact of surface adsorbed species on the tunneling current.

In summary, the components of the liquid electrolyte have a significant influence on the effective barrier height and thus also on the tunneling current. Even slight variations of the medium within the tunneling gap can therefore create changes in an STM signal. This effect is a key element in n-EC-STM measurements, as will be shown in the following.

## 4.2 Identification of Active Sites

The identification of active sites using EC-STM (n-EC-STM) takes advantage of the strong dependence between tunneling current and aspects such as the LDOS and  $\phi_e$ . In principle, the WE surface is scanned while the potential is set such that a certain electrochemical reaction is stimulated.<sup>[47][166]</sup> If the tip is positioned over an active site, the tunneling barrier becomes dynamic due to the reaction processes occurring at this point. The perpetual ad-/desorption and diffusion of reaction species influence the effective barrier height, as well as the LDOS. In Figure 4.4, a sketch of an OER event taking place within the gap between tip and sample is given. The ordered network of water molecules is locally disrupted, and the composition of the tunneling barrier changes over time. As previously elaborated, even water molecules and the orientation of molecules within the tunneling gap influence the effective tunneling barrier.<sup>[173,174,177]</sup> Therefore, also the tunneling current gets disturbed, which produces noticeable peaks (noise) in the STM signal. The appearance of such noise features due to species

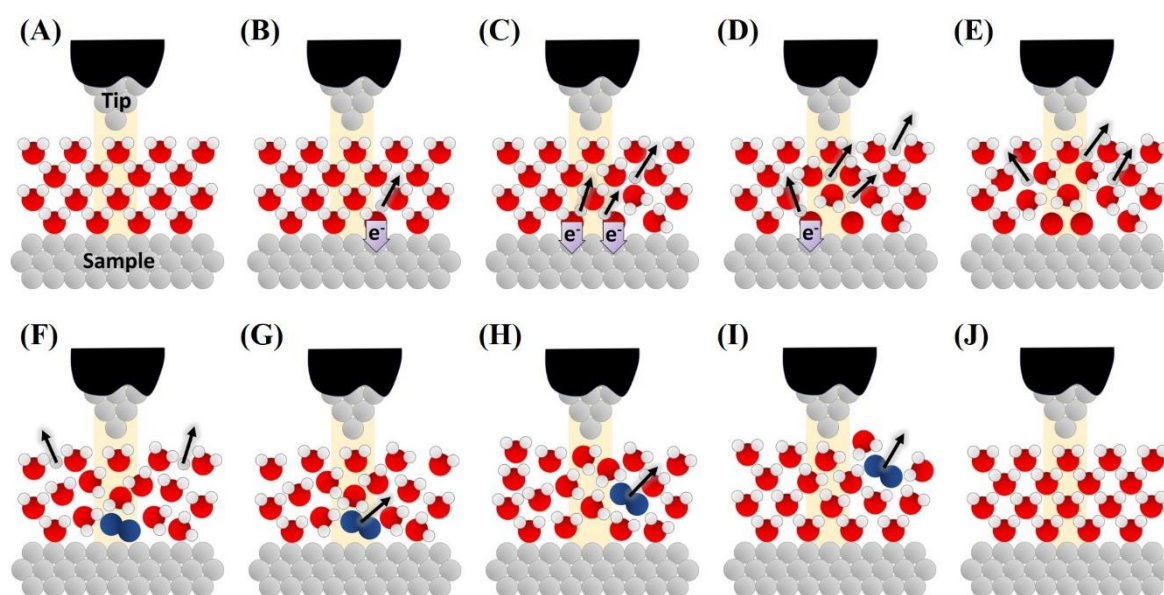


**Figure 4.4** Sketch of an OER process occurring between the sample and the tip of the STM. The ordered hydrogen network is disrupted and the composition of the tunneling barrier changes over time. It has been shown, that this influences the effective tunneling barrier and therefore also alters the tunneling current.<sup>[173,174,177]</sup> Color code: Red – oxygen in a water molecule, Blue – oxygen in an oxygen molecule, white – hydrogen, gray – tip/sample atoms. Adapted with permission from Ref. [195]. Copyright © 2020, John Wiley and Sons.

moving through the tunneling barrier is well-known in surface science and was already observed (in vacuum) shortly after the invention of the STM.<sup>[178,179,180,181]</sup>

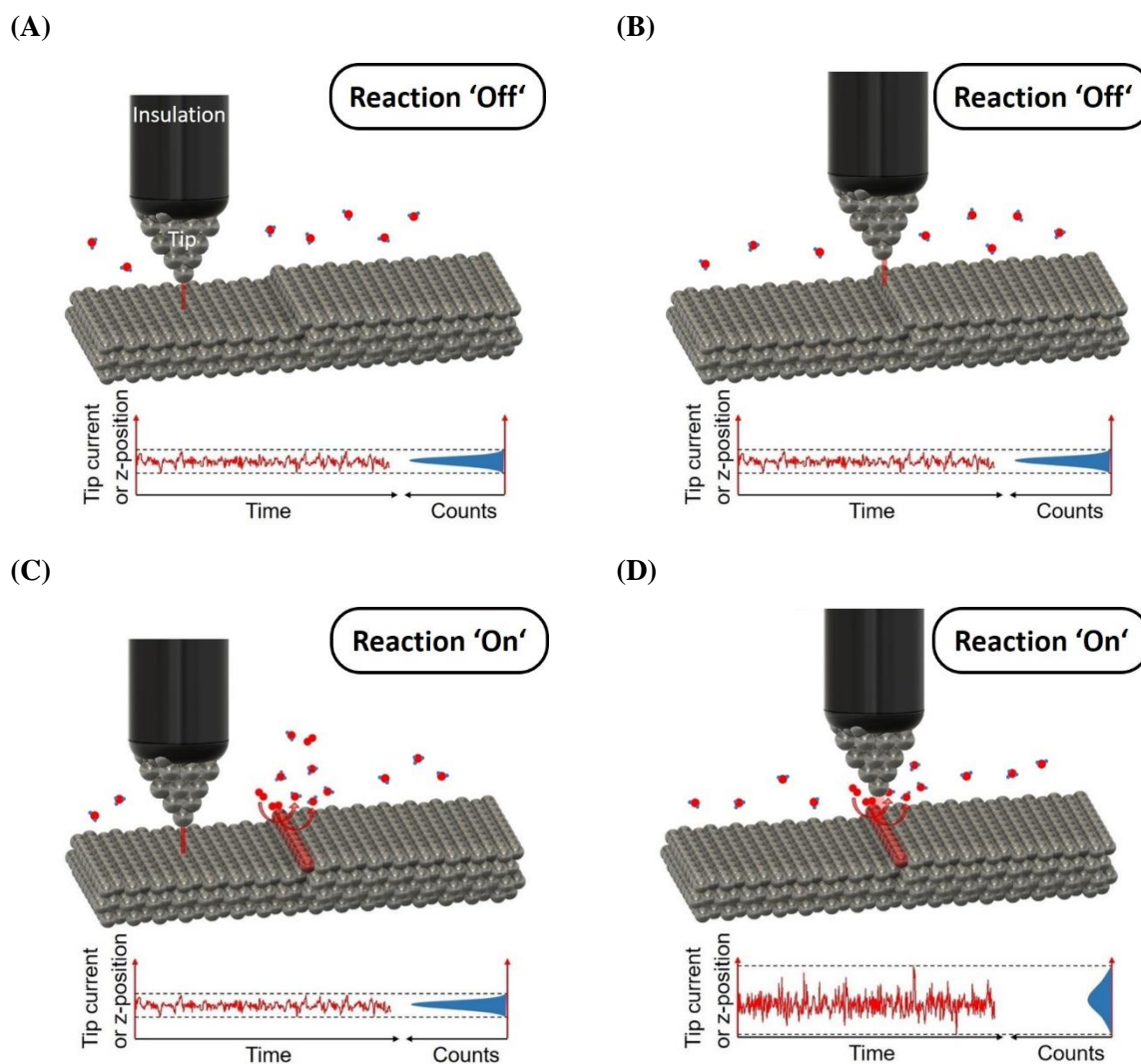


**Figure 4.5** Concept of n-EC-STM measurements. (A) and (B) reaction 'Off'. The tunneling current is stable and similar on the whole sample surface (red graph). This is reflected in a narrow distribution in the frequency count (blue graph) (C) Reaction 'On', tip over a non-active site. Locally, the situation at a non-active site is similar to reaction 'Off'. (D) Reaction 'On', tip over an active site. Due to reaction processes, the local environment is constantly changed, and the tunneling parameters vary over time. This causes fluctuations (noise) in the STM response. A frequency count of this signal will yield a broadened distribution. Adapted from Ref. [166].

## Electrochemical Scanning Tunneling Microscopy

The four key scenarios of n-EC-STM are depicted in Figure 4.5. In A and B, the WE potential does not support any reaction. Naturally, there are no active sites, and the tunneling barrier should be comparable on the whole surface. Keeping the tip fixed over any site leads to an almost constant tunneling current or z-position, depending on the chosen mode (see red graphs in Figure 4.5). The degree of noise in the measurement can also be reflected in a frequency count of  $I_T$  or z, which should yield a narrow peak for an undisturbed scan (see blue graphs in Figure 4.5). If a reaction is turned ‘On’, as illustrated in Figures 4.5C and D, there will be a visible difference in the STM response at non-active and active sites. In the first case, the behavior is comparable to a measurement where the reaction is ‘Off’ since the tunneling barrier remains mostly unchanged. In the second case, at an active site, the STM signal will become considerably noisier due to the constantly changing local environment. In the according frequency count, this is manifested in a broadened distribution. Thus, scanning the surface under reaction conditions can give a clear indication of electrocatalytically active sites by monitoring relative changes in the STM response. Figure 4.6A shows an exemplary n-EC-STM

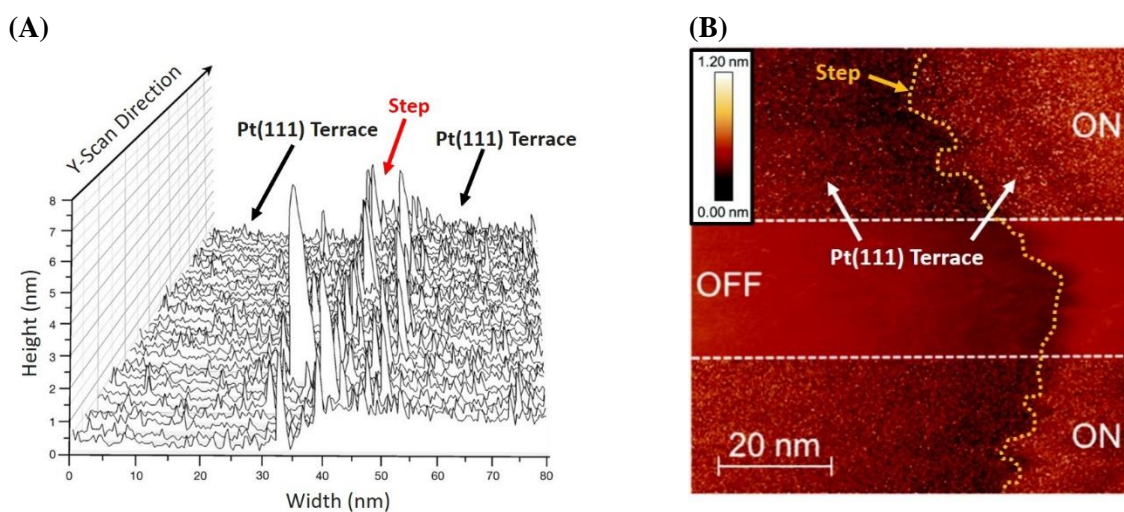


**Figure 4.6** Exemplary n-EC-STM measurements. (A) Pt(111) in 0.1 M HClO<sub>4</sub> under ORR conditions. The large noise features at the step indicate a higher local activity compared to adjacent terraces. Adapted with permission from Ref. [47] Copyright © 2017, Springer Nature. (B) Pt(111) in 0.1 M KOH under ORR conditions. Unlike the experiments in the acidic electrolyte, step and terrace appeared equally active in the alkaline electrolyte. During the scan, the reaction was turned ‘On’ and ‘Off’ as indicated, demonstrating the changes in the STM signal due to an ongoing reaction. Adapted with permission from Ref. [49] Copyright © 2019, Royal Society of Chemistry.

measurement on Pt(111) in 0.1 M HClO<sub>4</sub> (adapted from Ref. [47]). At ORR potentials, large noise features were observed near a step site, indicating a higher activity than on nearby terrace sites. In contrast, Figure 4.6B demonstrates that there is virtually no difference in the noise level of step and terrace on Pt(111) when using an alkaline electrolyte (adapted from Ref. [49]). In this case, the surface appeared homogeneously active towards the ORR. Furthermore, the image shows that the noise disappeared as soon as the reaction was turned ‘Off’, confirming the functionality of the measurements. The n-EC-STM technique has proven to be a remarkably versatile tool in the investigation of electrocatalytic hotspots. It has been successfully applied to many electrode materials, such as Pt and Pt-alloys, dichalcogenides, as well as metal oxides.<sup>[47,49,50,51,52,53,54]</sup> Since every electrode material has specific properties, the setup and measurement parameters need to be tailored to the explicit purpose and system.

### 4.3 Experimental Equipment

This chapter is dedicated to the experimental equipment used for the n-EC-STM measurements. First, the measurement devices, two Bruker MultiMode EC-STM/EC-AFM, are introduced. This is followed by an overview of the production and characteristics of the scanning probes.

#### 4.3.1 Bruker Multimode

The n-EC-STM measurements in this thesis were conducted using two Bruker MultiMode EC-STM/EC-AFM scanning probe microscopes. The feedback was regulated by a NanoScope IIID controller on one and a NanoScope V controller on the other device. The potentials were managed via the accompanying Universal Bipotentiostat from Bruker. The measurements parameters were controlled using the Nanoscope 5.31r1 and Nanoscope 9.70r1sr8 software, respectively. The recorded data were analyzed with Origin 2021 and the WSxM 5.0 software.<sup>[182]</sup> Figure 4.7A shows an image of one of the devices used for the experiments. It was mounted on an air table (Newport) and a large stone slab in order to minimize vibrations. The piezo system for vertical and lateral control of the scan is integrated into the stem of the device. In this type

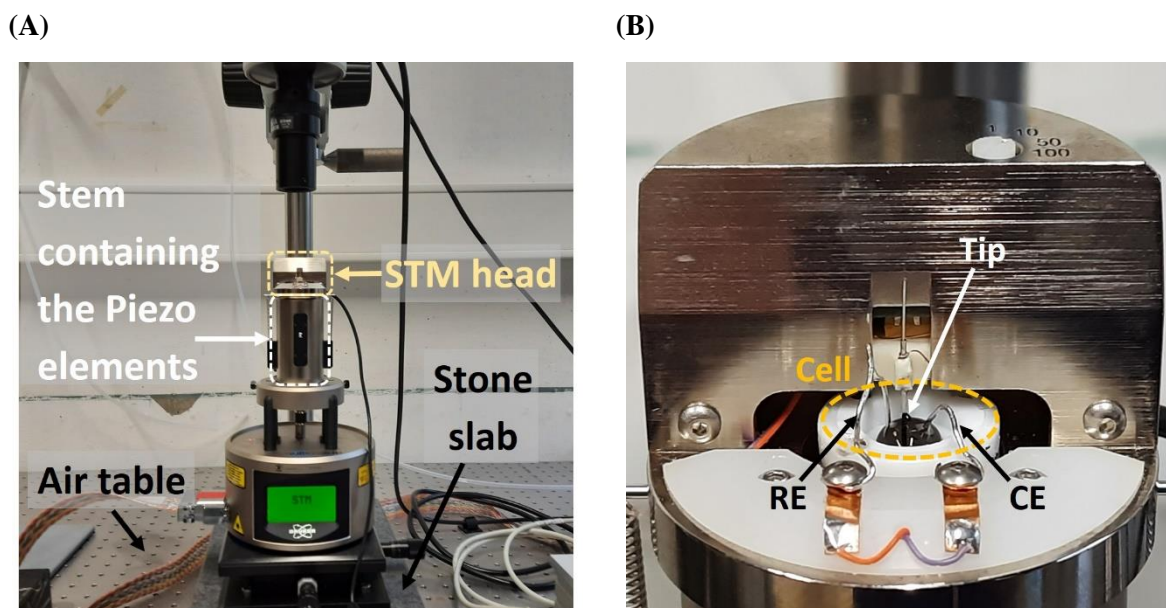


**Figure 4.7** (A) Image of the MultiMode EC-STM/EC-AFM used for the n-EC-STM measurements. The air table and stone slab underneath reduce vibrations. The piezo system is contained in the stem of the device, controlling the movement of the sample relative to the fixed tip. (B) Enlargement of the scanning head and sample holder/electrochemical cell. The reference (RE) and counter (CE) electrodes were positioned close to the scanning tip.

of the microscope, the sample is moved relative to a fixed tip. This setup does not change the scanning principle; however, it allows easy access to tip, cell, and electrodes and is therefore beneficial for electrochemical experiments. Figure 4.7B shows an enlargement of the scanning head and the EC-cell. The RE was placed close to the tip and sample to avoid the excessive ohmic drop. To have a reasonably large surface area of the CE, it was immersed into the electrolyte as much as possible. As the RE, a Pt wire (MaTecK,  $\phi = 0.5$  mm, > 99.99% purity) was employed. The CE was selected depending on the investigated sample. Since a large current may be flowing through the CE, particles could be shed off and deposited onto the sample surface. To avoid contamination by this effect, if possible, the same material was chosen as CE as for the WE. The used materials were a Pt wire (MaTecK,  $\phi = 0.5$  mm, > 99.99% purity) for measurements on Pt surfaces and a carbon rod (GoodFellow,  $\phi = 0.5$  mm, >99.95% purity) for investigations on the carbon-based samples. The scanning tip, arguably the most important component, needs to be prepared carefully, as will be discussed in the following chapter.

### 4.3.2 Tip Preparation

The quality of the scanning probe largely determines the possible resolution of the STM. It should be extremely sharp so that, ideally, just one atom interacts with the surface. In this study, the tips were mechanically ripped from a Pt80/Ir20 wire (GoodFellow and MaTecK,  $\phi = 0.25$  mm, >99.9+% purity) using a pair of pliers. Figure 4.8A shows a sketch of the procedure, and Figure 4.8B an image of an accordingly prepared tip, captured by scanning electron microscopy (SEM). The second common technique for tip fabrication is electrochemical etching. However, mechanical ripping is a faster process, without losing substantial quality.

Since the tip essentially acts as a fourth electrode in the EC-STM, the material and applied potential need to be chosen carefully. The Pt-Ir alloy works well for this purpose, with Pt being relatively inert in a sufficient potential range and Ir adding stiffness to the compound. Before the application in electrochemical measurements, the tips were insulated using Apiezon wax (Plano GmbH). This process is depicted in Figure 4.8C. The wax was heated to 150 °C – 200 °C using a soldering iron. The tip was slowly moved up and down through the liquid wax several times to ensure sufficient coverage of the surface. Only a small apex was left uncovered, as schematically shown in Figure 4.8D and indicated in the SEM image of a freshly prepared tip in Figure 4.8E. The smaller the uncovered apex, the less disturbance will be caused by faradaic reactions or the double layer capacity at the tip itself.<sup>[183]</sup> The exposed area depends *i.a.*, strongly on the viscosity of the wax, which can be tuned by adjusting the temperature.<sup>[184]</sup> Using the aforementioned temperature range, faradaic currents or offset currents of such tips in the EC-STM setup were typically between 50 pA and 200 pA. Selecting the tip potential and current setpoint accordingly allows high-resolution imaging in the electrochemical environment. The most critical parameters of the n-EC-STM experiments for the model systems in this thesis are given in Appendix B.

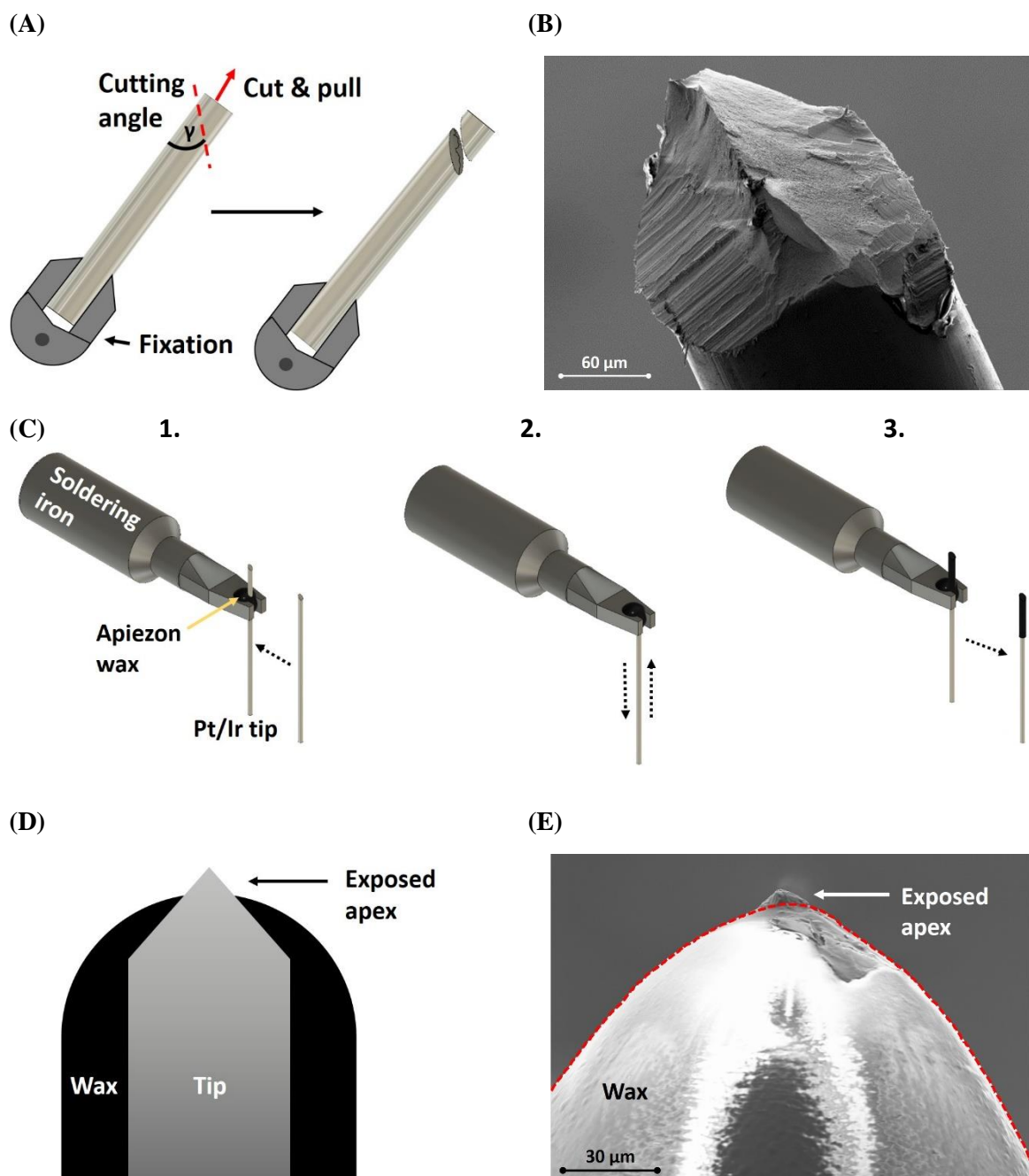


**Figure 4.8** (A) Tip cutting procedure. To ensure a sharp tip, the wire is cut at an angle of  $\sim 45^\circ$ . (B) SEM image of a mechanically fabricated tip, showing a sharp ridge caused by the ripping. (C) Insulation process. The tip is moved through the heated wax ( $150^\circ\text{C} - 200^\circ\text{C}$ ) several times to optimize the coverage. (D) Schematic cross-section of an insulated tip. Only a small apex is left uncovered and can contribute to the tunneling process. (E) SEM image of an insulated tip. The boundary of the Apiezon wax is marked in red. The exposed apex at the top is approximately  $15 \mu\text{m}$  wide. Adapted from Ref. [166].

## 5 Quantitative Determination of the Local Activity Using n-EC-STM

The capability of the n-EC-STM method to identify active catalytic sites has been demonstrated successfully on several model systems, as outlined in Chapter 4.<sup>[47,49,50,51,52]</sup> However, so far, the activity analysis was purely qualitative. In this chapter, a quantitative approach is developed, which extracts information about site-specific activity from the n-EC-STM data. The basic idea is to quantify the noise in the measurements at specific surface sites and relate it to the local turn-over frequency (TOF).

Pt(111) was chosen as the model system since its ORR characteristics in acidic electrolytes have been intensively studied.<sup>[185,186,187,188,189,190,191]</sup> Generally, it is believed that Pt(111) binds the ORR intermediate \*OH around 0.1 eV too strongly.<sup>[30]</sup> Therefore, the catalyst optimization focuses on engineering Pt surface sites that bind the intermediate slightly weaker than the (111) facet. It has been demonstrated that certain types of stepped crystals can achieve significantly higher ORR activities than the low-index planes.<sup>[36,76,190,192,191,193,194]</sup> However, these are usually measurements on extended surfaces, and the conclusions can only be drawn for the macroscopic ensemble. As a consequence, complications can arise when guidelines for nanoparticle design are derived from these observations.<sup>[194]</sup> Important questions still remain open, such as which surface sites contribute to what extent to the overall activity. In this light, being able to quantify the activity locally with the n-EC-STM method is particularly interesting and can result in more substantial design guidelines.

The content of this chapter was published in:

*Haid, R. W.<sup>1</sup>; Kluge, R. M.<sup>1</sup>; Liang, Y. and Bandarenka, A. S. In-situ quantification of the local electrocatalytic activity via electrochemical scanning tunneling microscopy, *Small Methods* 2021, 5, 2000710.<sup>[195]</sup>*

## 5.1 Preparation of the Pt(111) Single Crystals

The Pt(111) single-crystal disk electrode was purchased from MaTeck ( $\varnothing = 5$  mm). For its preparation, a three-electrode setup was used, as sketched in Figure 5.1A. Besides the main compartment, it features a preconditioning cell to control the gas saturation of the electrolyte. The RE was a mercury-mercurous sulfate electrode (MMS, SI Analytics) linked to the main compartment via a Luggin capillary. The potentials were converted to the RHE scale by:  $U(\text{RHE}) = U(\text{MMS}) + 0.66 \text{ V} + 0.059 \text{ V} * \text{pH}$ . As the CE, a Pt wire was employed. The electrodes were connected to a BioLogic VSP-300 potentiostat (BioLogic, EC-Lab<sup>®</sup> software V11.30). The glassware was frequently cleaned using ‘Caro’s acid’, a 3:1 mixture of  $\text{H}_2\text{SO}_4$  (96%, Roth) and  $\text{H}_2\text{O}_2$  (30%, Roth), and subsequently rinsed with boiling ultrapure water. For the electrochemical cleaning, the single crystal was immersed in the electrolyte in a hanging meniscus arrangement. The electrolyte, 0.1 M  $\text{HClO}_4$  (Merck Suprapur), was saturated with Ar

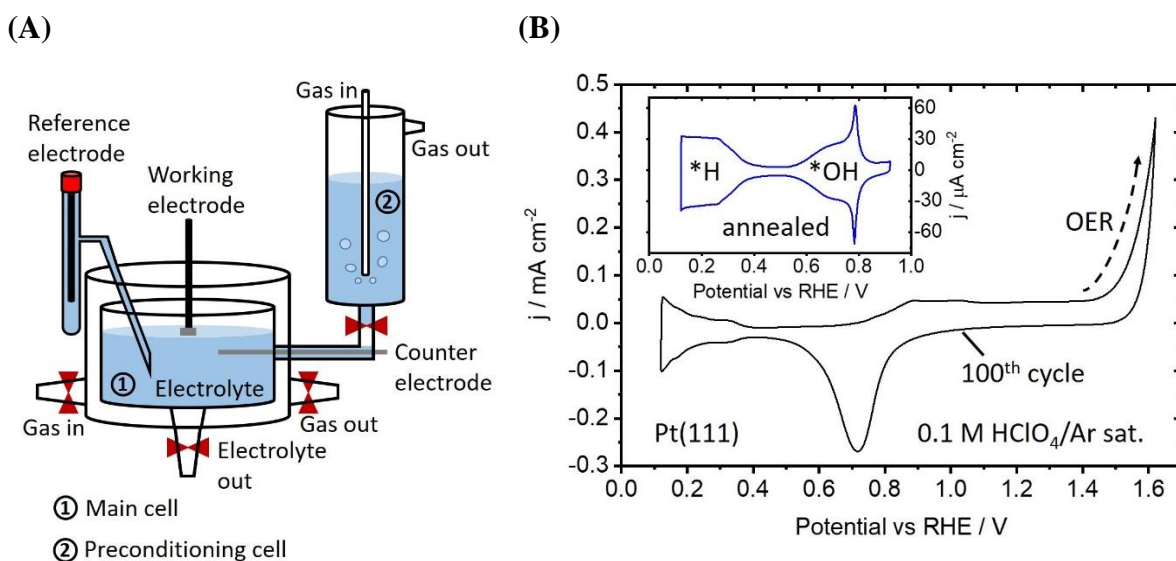


**Figure 5.1** (A) Schematic of the three-electrode cell used for the preparation of the Pt(111) single crystal. Besides the main compartment, it features a preconditioning cell for efficient purging of the electrolyte with gas. The crystal surface was immersed in the electrolyte in a hanging meniscus arrangement. (B) Electrochemical cleaning of the Pt(111) surface by cyclic voltammetry. After 100 cycles up to potentials of 1.6 V vs RHE, the surface structure was cleared from impurities, however, it was also roughened in the process. Annealing the crystal in Ar/CO atmosphere restored the (111) surface, as evident from the CV in the inset. Both CVs were taken in Ar-saturated 0.1 M  $\text{HClO}_4$  at a scan rate of 50 mV/s.

(Argon 5.0, Westfalen). By cycling the crystal up to potentials of 1.6 V vs RHE regime around 100 times (see Figure 5.1B), it was cleaned from surface impurities.

However, as has been visualized in-situ via EC-STM,<sup>[196][197]</sup> during this process, the (111) structure at the surface is roughened. To restore an atomically flat surface, the crystal was annealed at ~1000 °C using a butane gas burner (Leifheit Proline) and cooled in Ar/CO (Argon 5.0, CO 4.7 1000 ppm, Westfalen) atmosphere, following the method proposed by Kibler.<sup>[198]</sup> A CV of the crystal after annealing is given in the inset of Figure 5.1B. It showed the typical \*H and \*OH ad-/desorption features, confirming the restoration and quality of the (111) structure.<sup>[64][199][200]</sup> Using this method, the crystal was freshly prepared prior to each n-EC-STM experiment.

## 5.2 Establishing a Noise-Activity Relation on the Basal Plane

The general idea of the quantitative approach is sketched in Figure 5.2. In the first two steps, a linear relationship between the noise level in the STM signal and a measure of the local activity, the TOF (TOF<sub>b</sub>, b = basal plane), was established at the basal plane of the Pt(111) crystal. Subsequently, the noise level at step edges was quantified, and the respective TOF<sub>s</sub> (s= step) was extracted, assuming the same relation between noise and TOF as on the basal plane.

First, a linear potential sweep of the system was recorded in the EC-STM setup. As Figure 5.3A shows, the current resulting from the ORR increased linearly with decreasing potential between approx. 0.00 and -0.30 V<sub>Pt</sub>. Thereafter, the current converged to a constant value due to mass transfer effects in the air-exposed electrolyte. For the measurements, five potentials ranging from -0.05 to -0.25 V<sub>Pt</sub> (in 0.05 V steps) were selected. At -0.05 V<sub>Pt</sub> the reaction was essentially ‘Off’, whereas at -0.25 V<sub>Pt</sub> it was close to the mass transfer limit. The potentials in-between represented intermediate levels of ORR rates. To determine the noise level on the basal plane at each potential, n-EC-STM measurements were performed with the tip at a fixed position and height over an extended Pt(111) terrace. The tunneling current was recorded for 128 s at each potential. An excerpt (approx. 2 s) of such a measurement is given in Figure 5.3B. At more negative potentials, the STM signal became noisier.

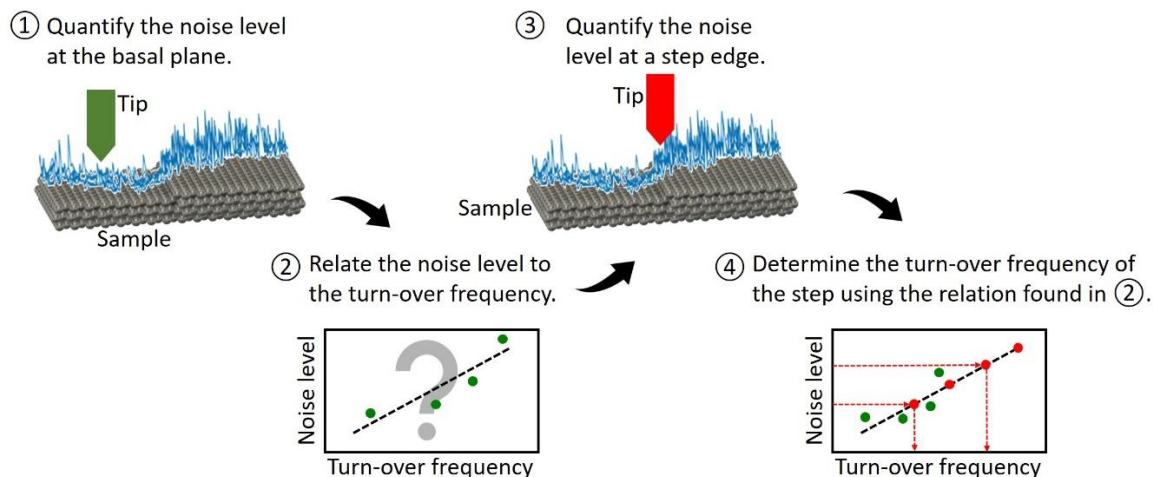


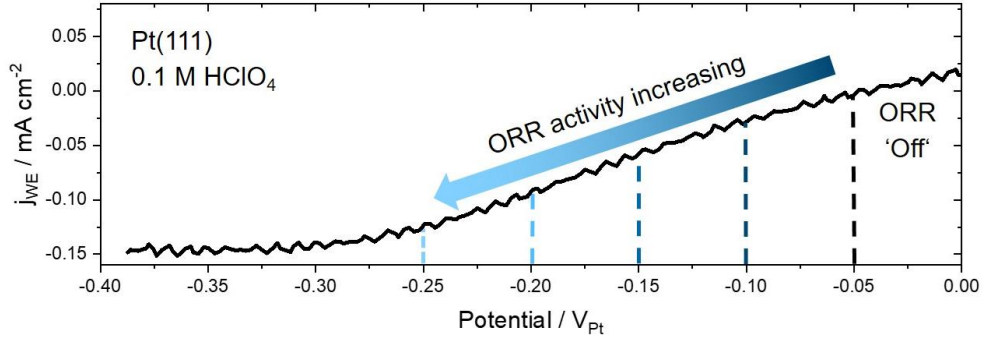
**Figure 5.2** Procedure of the quantitative n-EC-STM approach. At first, the noise level under reaction conditions is determined at the basal plane. In the second step, the noise level at the basal plane can be linearly related to the basal plane TOF. In the third step, the noise level of a step is recorded in the measurement. Finally, the TOF of steps can be extracted from the previously determined relation between the TOF and the noise level.

To quantify the noise level at a certain potential, the respective raw STM data (here the tunneling current  $I_T$ ) was derived with respect to adjacent data points (here the time  $t$ ), according to:

$$\left(\frac{dI_T}{dt}\right)_{t_1} = \frac{1}{2} \left( \frac{I_2 - I_1}{t_2 - t_1} + \frac{I_1 - I_0}{t_1 - t_0} \right) \quad 5.1$$

with the consecutive data points  $(I_a, t_a)$ ,  $a = 0, 1, 2$ . From the derivatives of the data in Figure 5.3B, histograms were rendered as shown in Figure 5.4A. In principle, the shape of the histogram gives a representation of the stability of the tunneling current during the measurement: a stable signal yields a sharp peak, whereas a noisy signal results in a broad peak. This is because a noisy signal with a higher number of fluctuations leads to a larger variety of signal derivatives (slopes in the line scans) and thus a broader distribution and histogram. In line with the expectations, in Figure 5.4A, the noisier STM signal at more negative potentials is reflected in the broader shape of the respective histogram.

(A)



(B)

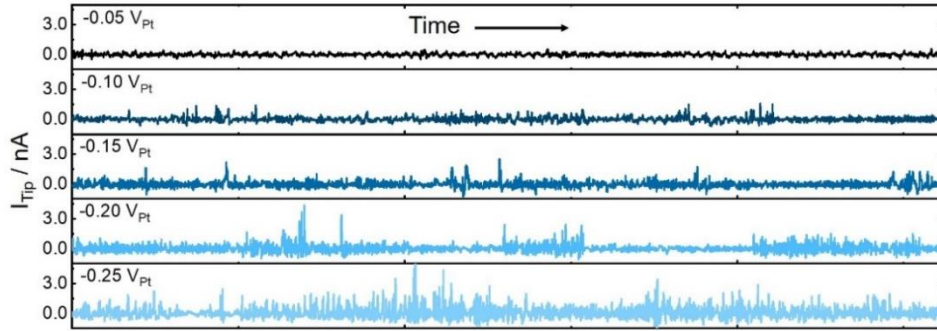


**Figure 5.3** (A) Potential sweep in the ORR region of Pt(111) in 0.1 M HClO<sub>4</sub>, recorded in the EC-STM setup at a scan rate of 50 mV/s. For the n-EC-STM measurements, five potentials between -0.05 and -0.25 V<sub>Pt</sub> were selected. (B) Excerpt of the n-EC-STM measurements on the basal plane. With decreasing potential, the noise in the STM signal, here the tunneling current, increases. Data published in Ref. [195].

To use the ‘broadness’ of a histogram for the quantification of the noise level, the histograms were fitted by a Gaussian curve (solid lines in Figure 5.4A):<sup>[201]</sup>

$$y = y_0 + \frac{A}{\omega\sqrt{\pi/2}} e^{-2\frac{(x-x_c)^2}{\omega^2}} \quad 5.2$$

With the offset  $y_0$ , the area  $A$ , the width  $\omega$ , and the center  $x_c$ . From this fit, the full width at half maximum (FWHM) was extracted. It can be calculated as follows:

$$\text{FWHM} = \sqrt{2\ln(2)\omega} \quad 5.3$$

The higher the noise level of a data set is, the larger the FWHM. In the next step, this value was related to the local activity. The local activity of a site can be expressed by a site-specific TOF. This is defined as the number of completed catalytic cycles at the investigated surface site per time unit.<sup>[202]</sup> The measurements herein were performed at the (111) basal plane of the single crystal, which, due to careful preparation of the sample (see Chapter 5.1), should possess only a low number of step edges, defects, and other non-basal surface sites.<sup>[198]</sup> Therefore, even though these sites might yield a higher local activity than terrace sites, it can be assumed that the overall activity was dominated by the basal plane. Consequently, the TOF<sub>b</sub> of the basal plane can be approximated as the TOF of the whole surface. This value can be calculated from the sample current recorded simultaneously during the n-EC-STM measurement. The equation for it reads as follows:

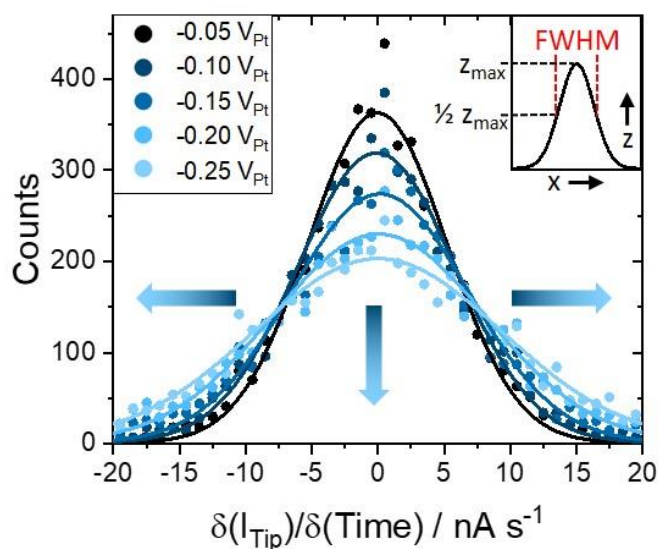
$$\text{TOF} = \frac{|j_{WE}| A_{WE}}{ne N_A} \quad 5.4$$

Here,  $j_{WE}$  and  $A_{WE}$  are the current density and the surface area (in this case 0.126 cm<sup>2</sup>) of the WE, respectively. Further,  $n$  is the number of electrons transferred per reaction event (for the ORR:  $n = 4$ ),  $e$  is the elemental charge, and  $N_A$  the number of atoms on the surface of the WE. The last parameter can be obtained using the following equation:

$$N_A = \frac{A_{WE}}{a_{pt(111)}\sin(\alpha)} \quad 5.5$$

The lattice parameters  $a_{pt(111)}$  and  $\alpha$  for the Pt(111) surface are 2.8 Å and 60°, respectively.<sup>[203]</sup> In Figure 5.4B, the determined FWHMs from Figure 5.4A were plotted against the TOF<sub>b</sub> values calculated from Eq. 5.4. The relation between the two values can be described as linear. A linear fit of the data in Figure 5.4B returned a slope of 0.14 (±0.02) nA s<sup>-1</sup> mHz<sup>-1</sup>. This experiment was performed nine times in total to substantiate the linear noise level-activity trend with statistical relevance (see Appendix C – Figure C.1 and Table C.1 for details).

(A)



(B)

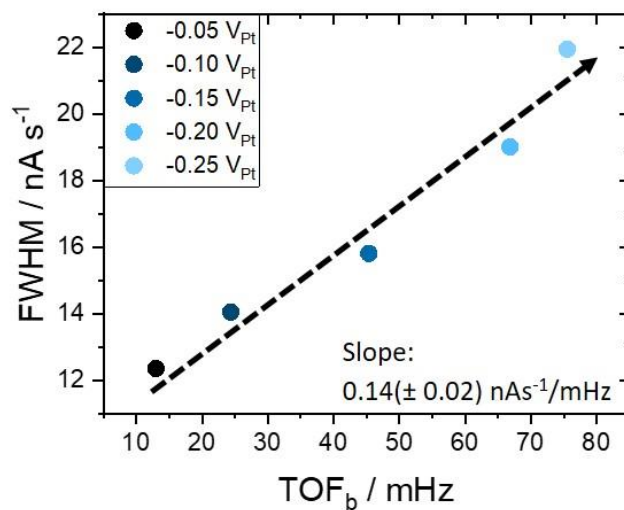


**Figure 5.4** (A) Histograms and Gaussian fits of the n-EC-STM data (as given in Figure 5.3) recorded over the Pt(111) basal plane in 0.1 M  $\text{HClO}_4$  at different ORR potentials. The histograms broaden with increasingly negative potential (higher ORR currents) as the STM signals show higher noise levels. The FWHM of the Gaussian fit (*cf.* inset) is chosen as the descriptor of the noise level. (B) The FWHM plotted versus the TOF at the basal plane reveals a linear relation. This suggests that the noise level in the STM signal is directly related to the local rate of the reaction. Data published in Ref. [195].

The relation between FWHM and TOF was linear in all cases, however, with different slopes. There are several possible reasons for this. First, it is worth noting that in the STM setup, the electrolyte can slowly evaporate during the measurement, resulting in slight changes in the concentration over time. To estimate the influence of the concentration changes on the linear noise level - activity trend, some of the experiments were performed in a reverse way, *i.e.*, starting at  $-0.25 V_{Pt}$  and increasing the potential stepwise to  $-0.05 V_{Pt}$ .

However, the resulting relation between noise and activity of these measurements was similar to the other experiments. Furthermore, most measurements were performed with a constant tip potential, and accordingly, the bias between tip and sample was different at each applied sample potential. To exclude this as the reason for the observed quantitative changes in the relation between noise and activity, the experiment was repeated with constant bias, *i.e.* changing the tip potential along with the sample potential. The result (see Appendix C - Figure C.2) was similar to the previously presented experiments; consequently, the influence of the potential bias can be neglected in this instance. After ruling out the minor influences of electrolyte concentration changes and the changes in the tip-sample potential during the measurement, it is most likely that the properties of the STM tip are responsible for the discrepancies in the slopes. It can be assumed that both the tip shape and the quality of the insulation influence the ‘sensitivity’ of the tip toward the recorded noise level without changing the general trend of the relation to the activity.

Additionally, the Pt(111) disk electrode was freshly prepared before each measurement series, which could lead to slight differences in the crystal surface quality, resulting in an over-/underestimation in the calculation of the TOF. Thus, both tip and sample preparation could lead to variations in FWHM and TOF values, respectively, and therefore, influence the slope value of their linear relationship. They do, however, not change the overall existence of such a linear trend.

In summary, the experiments showed a linear relationship between noise level and TOF for the ORR on Pt(111) in 0.1 M HClO<sub>4</sub>. With this in mind, it is possible to estimate the local activity at other surface sites, such as steps, where it is challenging to directly access the TOF.

### 5.3 Extracting the Site-Specific Turn-Over Frequency

According to literature reports, a higher ORR activity can be expected in the vicinity of step sites on Pt(111) due to a weakened and, thus, improved \*OH binding.<sup>[36,190,194]</sup> Usually, to evaluate the activity of step sites, it is necessary to perform measurements on stepped single crystals or to use theoretical approaches. In the former, the macroscopic activity is obtained, which also includes the basal plane and other surface sites. Here, a method is presented which offers a way of determining the local activity of step sites with a resolution in the nanometer

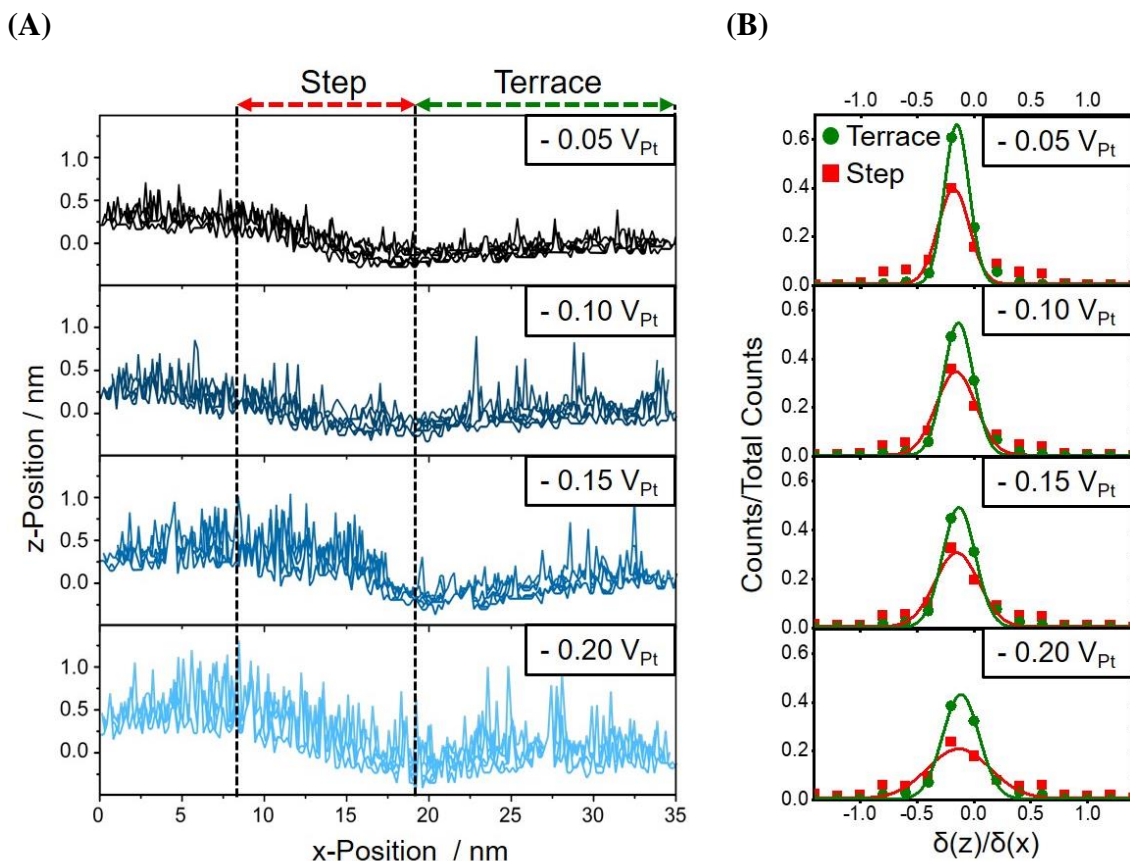


**Figure 5.5** (A) To identify the TOF<sub>s</sub> for the ORR on Pt step sites, n-EC-STM measurements were performed across step and terrace sites. The data was divided into the respective regions. (B) The histograms indicated a higher noise level at the step compared to terrace sites. In general, an increase in the noise with decreasing potential was observed. The local noise level can be extracted using the FWHM of the Gaussian fits for both step and terraces sites, respectively. Data published in Ref. [195].

regime. In Chapter 5.2, a linear trend between noise level and activity was established for basal planes. However, for step sites, the TOF cannot be calculated in the same way as for the basal plane (Eq. 5.4), since the sample current originates from the macroscopic ensemble. Still, the noise level at step sites of the Pt(111) single crystal can be quantified analogously to the basal plane, as described in Chapter 5.2. Assuming that the linear trend between activity and TOF is the same for all surface sites, the step site TOF ( $\text{TOF}_s$ ) can be extracted from the previously determined relation between noise level and  $\text{TOF}_b$  at the basal plane. As the previous experiments showed, the slope of the relation is specific to the set of measurement conditions, especially the tip and sample preparation. Consequently, a calibration curve needs to be rendered from data at a terrace site in the same experiment to determine the activity at a step. Therefore, the n-EC-STM measurement was designed such that the tip scanned along a trajectory including both a terrace and a step in the constant current mode. Figure 5.5A gives an example of such a measurement, showing several scans at sample potentials of -0.05, -0.10, -0.15, and -0.20  $V_{\text{Pt}}$ . The data was divided into ‘terrace’ and ‘step’ and subsequently transformed into histograms following the procedure in Chapter 5.3. Due to the different STM mode, the height data was now differentiated with respect to the x-scan direction (instead of tunneling current versus time in Eq. 5.1). As visible in Figure 5.5B, the histograms of step and terrace sites broadened with decreasing potential, indicating a gradual increase of activity with ‘overpotential’ at both types of sites. Moreover, at each potential, the FWHM of step sites was larger than at the terrace, indicating that the former were generally more active.

From the Gaussian fits of the ‘terrace’ data, the FWHM was extracted, and the noise-activity relation was rendered, as demonstrated in the previous section. The result is plotted in Figure 5.6A (circles). Subsequently, the FWHM of the fits for the step data was placed on this calibration curve (squares). This reveals the corresponding  $\text{TOF}_s$ , as indicated by the red arrows in Figure 5.6A. Evidently, the step sites had a higher TOF than the terraces at each potential. To account for statistics, the experiment was performed nine times in total, as collected in Appendix C - Figure C.3, Table C.1. The step sites appeared to be considerably more active than the adjacent terraces in most cases.

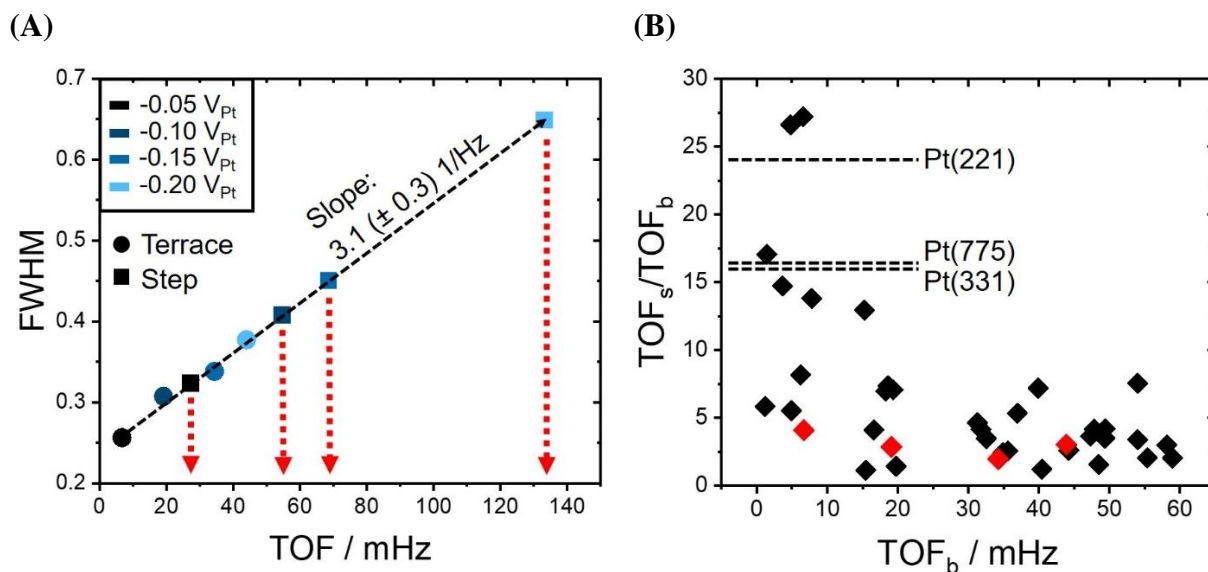


**Figure 5.6** (A) Noise-activity relation rendered from the FWHM and the TOF of the basal plane shown in Figure 5.5A (circles). Placing the FWHM of the step (squares) on this calibration curve returns the  $\text{TOF}_s$  values, as indicated by the red arrows. (B) Improvement factor  $\text{TOF}_s/\text{TOF}_b$  versus the  $\text{TOF}_b$ . The measurement data points shown in Figure 5.5 are highlighted in red. Step sites show higher activities than terraces, especially at potentials close to the reaction onset (lower  $\text{TOF}_b$ ). The improvement factors are in good agreement with the literature, and the highest factors are close to values expected from the best performing Pt facets. Data published in Ref. [195].

The enhancement factor  $\text{TOF}_s/\text{TOF}_b$  was calculated for each pair of data points (*i.e.*  $\text{TOF}_s$  and  $\text{TOF}_b$  at the same potential and from the same measurement) to analyze this effect more closely. In Figure 5.6B, all improvement factors were plotted versus the corresponding  $\text{TOF}_b$  (data of the plot can be found in Appendix C - Table C.2). One can see that, particularly at low  $\text{TOF}_b$ , the activity increase at steps compared to terraces was considerable. At higher  $\text{TOF}_b$ , the activity enhancement of step sites was lower, albeit still displaying around three times higher activity on average. In the following, the results will be discussed in more detail.

## 5.4 Discussion

The method presented here offers a way to quantify the local activity of specific surface structures under reaction conditions. The first set of measurements allowed the general

conclusion that the n-EC-STM technique is sensitive to the reaction rate. This was indicated by the proportional increase in the noise level of the STM signal at increased ‘overpotentials’. This can be used to quantify the local activity of surface structures via n-EC-STM. Performing a series of similar experiments revealed a linear relation between the noise level and the ORR activity of the Pt(111) basal plane in acidic electrolytes. The linear trend was universal. However, the absolute proportionality values were specific to the measurement conditions, most likely due to variations in tip and sample preparation.

The second set of measurements established a way to quantify the local activity at surface sites deviating from the (111) basal plane. This was demonstrated by analyzing the TOF of various step sites using the relation between noise and activity at the basal plane from the same measurement as a calibration curve. From the results, the improvement factors  $\text{TOF}_s/\text{TOF}_b$  for neighboring step and terrace sites were calculated. It is believed that sites in the vicinity of steps on Pt(111) can offer a more favorable binding of the reaction intermediates,<sup>[36,190,194]</sup> which is reflected in the improvement factors obtained *via* n-EC-STM. It is noticeable in Figure 5.6B that the difference between the step and the basal plane was particularly high at lower  $\text{TOF}_b$ , *i.e.*, close to the onset of the reaction. This suggests that here, mainly the step sites were active, while the contribution from the basal plane was low. With decreasing potential, the basal plane starts to ‘catch up’, albeit still showing less activity compared to step sites.

It is important to note that differences to standard activity tests, such as RDE measurements, arise due to the special requirements of the EC-STM setup. Firstly, the electrolyte was not saturated with oxygen during the experiments but exposed to air. Moreover, mass flow is limited in the confinement of the EC-STM cell. As a consequence, the here obtained TOF values will differ from conventional RDE measurements. Despite these differences, it is interesting to compare the here obtained local improvement factors between step sites and basal plane to macroscopic RDE activity measurements on stepped Pt single crystals from the literature. Although the orientation of the steps was not visible in the STM images, it can be assumed that steps of various coordinations were captured in the experiments. According to Kuzume *et al.* and Hoshi *et al.*, Pt(221), Pt(331), and Pt(775) show the highest ORR performances among the high-index planes.<sup>[36,76,193]</sup> For Pt(221), an improvement of around 6.2

is found compared to Pt(111). Assuming the activity originates predominantly from the step sites with increased coordination and taking into account the terrace width of four atoms, one can extrapolate an improvement factor of 24.8 for steps on the Pt(221) surface. This is remarkably close to the highest observed improvement factors in the n-EC-STM measurements (around 27). Furthermore, the next highest factors (between 13 and 17) are close to the improvement that would be expected from the steps of the Pt(331) and the Pt(775) structures.<sup>[36,76,193]</sup> Besides these particularly active facets, there are many others that offer only slight improvements compared to Pt(111). This is reflected in the n-EC-STM data by the many cases where the improvement factor lies between 1 and 10. The close similarities to the results from RDE measurements demonstrate the viability of this new quantitative n-EC-STM approach. Moreover, it indicates that the improvement factors that can be obtained by comparison of two surface sites with this method may offer additional, *in-situ* insight regarding the question to what extent specific sites contribute to the overall activity.

In summary, a method was developed which utilizes the extent of the registered noise level in the n-EC-STM system to assess the local activity at specific surface sites. With this novel approach, not only qualitative but also quantitative information about the local activity can be gathered. However, it is crucial to keep in mind that the STM cannot reveal the exact orientation of the investigated surface sites under the applied conditions. Therefore, the interpretation of the data needs to be supplemented by other approaches. In this aspect, it was found that the activity increase at step sites compared to the basal plane is in good agreement with literature reports, substantiating the functionality of the method. Since the technique can probe individual sites directly under the reaction conditions, the obtained information should apply to extended surfaces and nanoparticles.



## 6 Highly Resolved Active Sites for the Hydrogen Evolution at Model Carbon Surfaces

The commonly used catalyst material for the HER is platinum, mainly in the form of nanoparticles on carbon support (Pt/C).<sup>[204,205,206]</sup> However, recently, it has become apparent that it is possible to employ carbon itself as the catalyst.<sup>[207,208]</sup> Especially modifications of the graphene matrix via doping resulted in alternatives competitive with Pt/C.<sup>[209,210,211,212]</sup> On the other hand, there are many applications where carbon is part of an electrode on which hydrogen generation is undesired. For example, in batteries and supercapacitors, as well as electrolyzers involving the reduction of CO<sub>2</sub> or N<sub>2</sub>, the HER should generally be avoided.<sup>[213,214,215]</sup> It is therefore of interest to identify the origin of the HER activity on carbon so that it can be designed in a way that fits the desired application, either promoting or suppressing H<sub>2</sub> generation. In this chapter, the active sites of HOPG are determined via n-EC-STM. Particular attention was given to the spatial resolution of the measurements. The surface sites were monitored with down to atomic resolution under reaction conditions for the first time. In the resulting images, the active sites can be pinpointed individually on the graphene matrix. The experimental data was supported by a dedicated DFT study and discussed in the light of other research reports on this topic.

The herein presented results have been published in:

*Kluge, R.M.<sup>1</sup>; Haid, R. W.<sup>1</sup>; Stephens, I.E.L.; Calle-Vallejo, F. and Bandarenka, A. S. Monitoring the active sites for the hydrogen evolution reaction at model carbon surfaces, Physical Chemistry Chemical Physics* **2021**, 23, 10051-10058.<sup>[216]</sup>

## 6.1 The Structure of Highly Oriented Pyrolytic Graphite

HOPG is essentially a stack of graphene layers connected by van der Waals interaction. Its typical  $sp^2$  configuration results in a surface structure following a honeycomb pattern formed by the hexagonal arrangement of carbon atoms (see Figures 6.1A and B for details). Prior to the experiments, the samples (MikroMasch, spread  $3.5^\circ \pm 1.5^\circ$ ) were prepared by cleaving the top layers using scotch tape. In this way, a clean surface with few defects was ensured. Thus, it was possible to find large, mostly defect-free terraces on the sample. However, there will always be a certain amount of steps and defective sites in the carbon matrix.<sup>[217]</sup> Consequently, the HOPG can serve as a versatile model system and allow conclusions for other types of carbon materials.<sup>[218]</sup> In this chapter, the n-EC-STM technique was applied to probe the activity of these surface sites under HER conditions. As an electrolyte, 0.1 M  $HClO_4$ , prepared by diluting  $HClO_4$  (Merck Suprapur®, 70%) with ultrapure water (Evoqua, 18.2  $M\Omega$  cm), was used in the experiments. On the EC-STM setup, a Pt RE and carbon rod CE were installed. Importantly, the aim was not only to identify the active sites but also to capture them with high resolution. So far, n-EC-STM has only been used to distinguish different structures, such as *e.g.* terraces, steps, and islands. However, in principle, the STM was capable of resolving the electronic structure of surfaces atomically.<sup>[219]</sup> Consequently, it would be interesting to reach such high resolution under the application of a reaction potential and observe individual active sites on

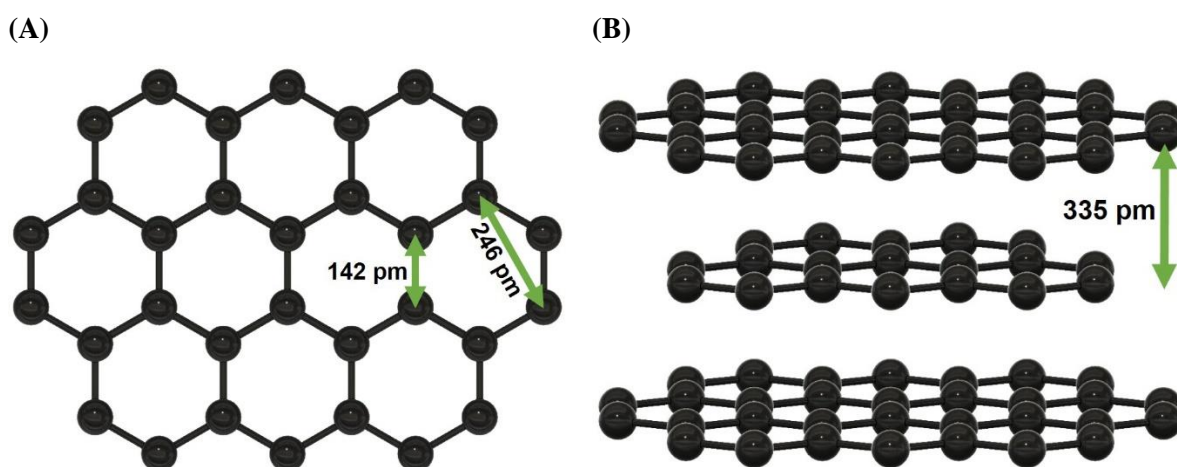


**Figure 6.1** (A) Model of the hexagonal ‘honeycomb’ structure of graphene. (B) Side view of HOPG. It is essentially a stack of graphene layers with a typical layer-to-layer distance of around 0.335 nm.<sup>[219]</sup>

the electrode surface. For this purpose, all images in this chapter were captured with the STM in constant height mode and with a small scan size, *i.e.*, 10 x 10 nm or less.

### 6.2 n-EC-STM at HOPG Terraces and Edges

To begin, a CV of the HOPG was recorded in the EC-STM setup (*cf.* Figure 6.2A). Potentials in the large double layer region (approx.  $-0.7 V_{Pt}$  to  $+0.7 V_{Pt}$ ) were considered as ‘Off’-condition for the EC-STM measurement. For HER ‘On’, potentials below  $-1.0 V_{Pt}$  were applied. Further details on the measurement parameters can be found in Appendix B. First, n-EC-STM was performed on a HOPG terrace, *i.e.*, the basal plane (see Figure 6.2B for a sketch of the basal and edge plane). Figures 6.3A and B show measurements resolving the typical atomic pattern of the HOPG basal plane for reaction ‘Off’ and ‘On’. After recording, the data were treated using the fast Fourier transformation (FFT) tool in the WSxM software to represent the structures more clearly. No significant impact of the reaction on the image was detected, suggesting that defect-free terraces are inactive. Therefore, the HER activity has to originate from other surface structures. Consequently, an area including a step was investigated. Figures 6.4A and B show the same position on the sample while the reaction was ‘Off’ and ‘On’,

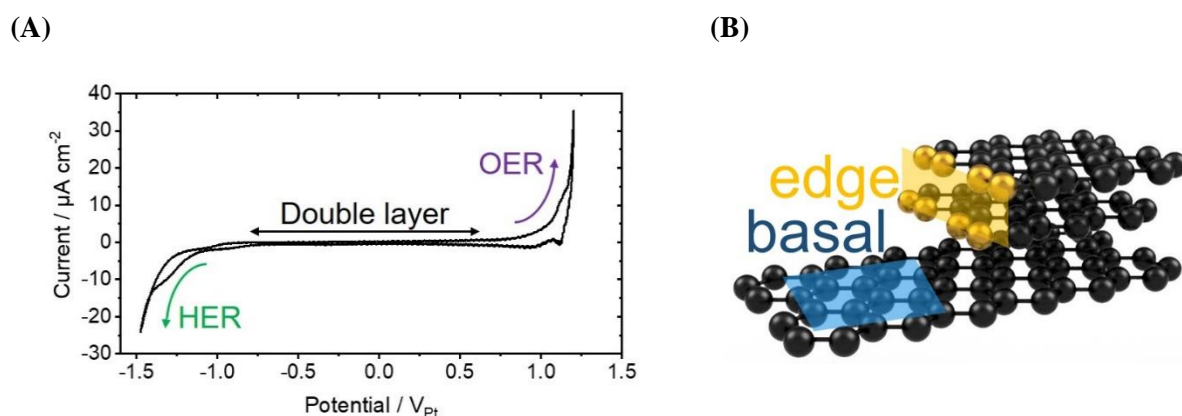


**Figure 6.2** (A) CV of HOPG in the EC-STM Setup (0.1 M HClO<sub>4</sub>, scan rate 50 mV/s). Potentials in the double layer region were used for reaction ‘Off’ and potentials below  $-1.0 V_{Pt}$  for HER ‘On’. Data published in Ref. [216] (B) Model of the basal and edge plane of HOPG. Reprinted with permission from Ref. [216]. Copyright © 2021, Royal Society of Chemistry.

## Highly Resolved Active Sites for the Hydrogen Evolution at Model Carbon Surfaces

respectively. Again, the images were FFT filtered. In both images, the atomic pattern is partially visible on the terraces.

(A)

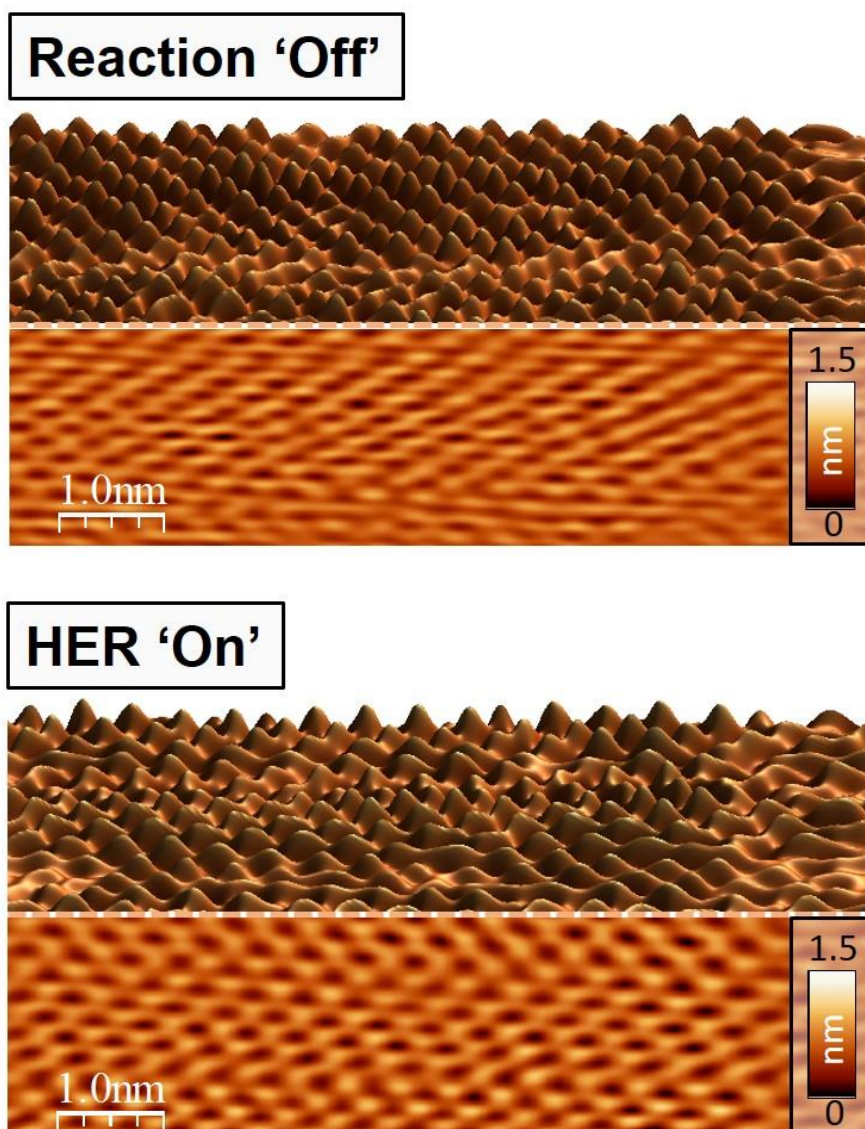


**Figure 6.3** (A) FFT filtered high-resolution EC-STM measurement of the basal plane of HOPG while the reaction was 'Off' ( $-0.5 V_{Pt}$ ). The top half shows a 3D, the lower half a 2D perspective. (B) Repetition of the measurement in (A) under HER conditions ( $-1.1 V_{Pt}$ ). No noise features were visible, suggesting that the basal plane remains inactive despite the applied reaction potential. Data published in Ref. [216].

## Highly Resolved Active Sites for the Hydrogen Evolution at Model Carbon Surfaces

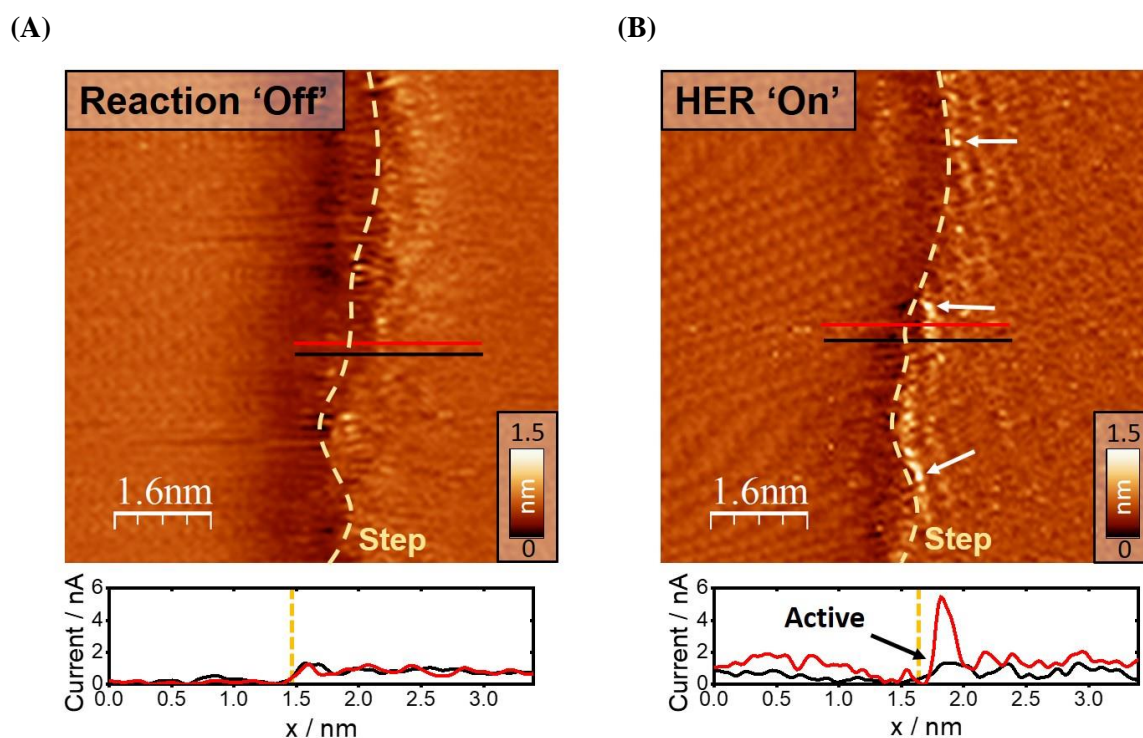


**Figure 6.4** n-EC-STM measurements of an area including a step edge while the HER is (A) ‘Off’ ( $-0.8 V_{Pt}$ ) and (B) ‘On’ ( $-1.1 V_{Pt}$ ). In part, the atomic structure of the surface was recognizable on the terraces. Noticeable noise features appeared along the step edge under reaction conditions, as indicated by the arrows. They were predominantly confined to the first two rows of atoms along the upper step edge. The difference between an active and an inactive site is illustrated by the profiles along the red and black lines given below the images. The active site is distinguishable by the large spike in the STM signal. Data published in Ref. [216].

In accordance with the measurements presented in Figures 6.3A and B, the terraces did not exhibit signs of activity. However, distinct white dots appeared scattered along the upper edge of the step under reaction conditions (marked by white arrows in Figure 6.4B). Below the images, tunneling current profiles along the red and black lines indicated in the images are given. While the reaction was ‘Off’, the step was traced accurately along both lines. Under HER conditions, on the other hand, this was only the case for the black line. The red line includes an active site at the step, which is reflected as a large spike in the signal. Judging from the scale of the image, the noise features were predominantly found within 0.5 nm (*i.e.* within two rows of atoms) along the edge of the upper terrace. To get a more comprehensive picture of the position

## Highly Resolved Active Sites for the Hydrogen Evolution at Model Carbon Surfaces

of the active sites, the measurement under reaction conditions was repeated for several steps with even higher resolution.

### 6.3 High-Resolution of Active Sites

The atomic pattern of HOPG was already recognizable in Figure 6.4. To elicit this structure more clearly and to get more substantial information about the position of active sites, the resolution was further increased while applying an HER ‘On’ potential. In Figures 6.5A and B, two examples of n-EC-STM measurements at a single step edge are displayed. The images were processed with FFT filtering to obtain a clear rendition of the surface structures.

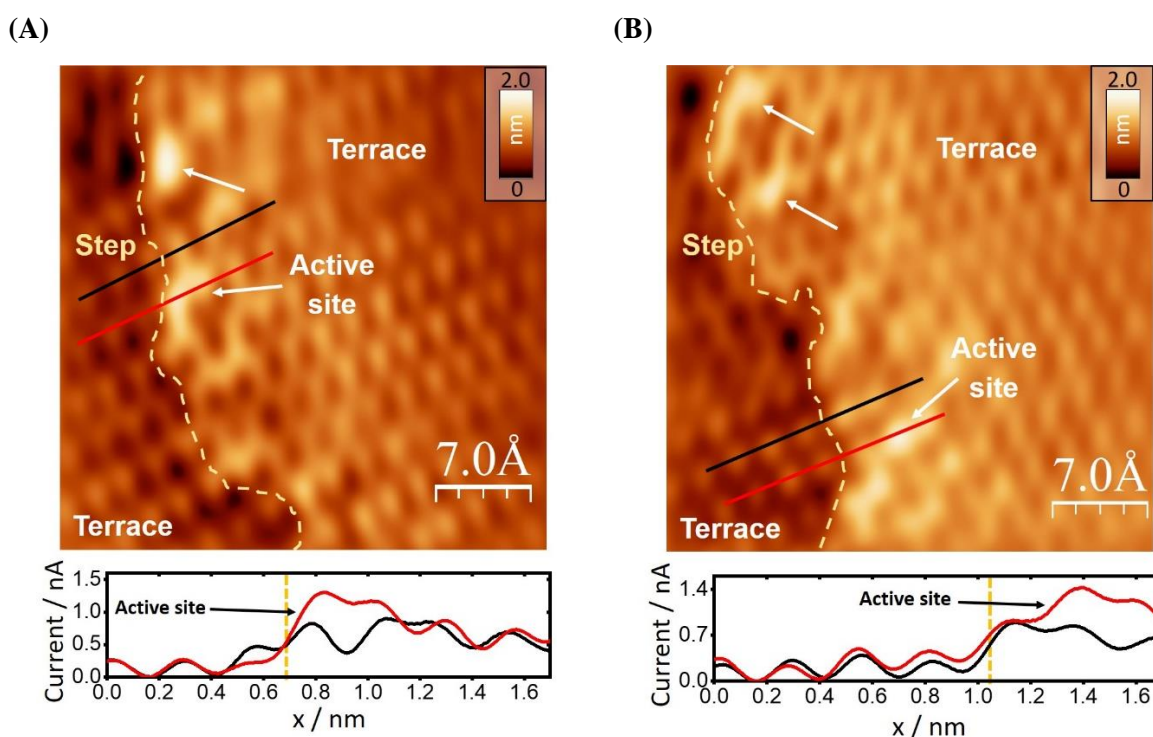


**Figure 6.5** High-resolution n-EC-STM measurements under HER conditions ( $-1.20 \text{ V}_{\text{Pt}}$ ) (A) In this image, the atomic pattern of HOPG was visible. The active sites were close to the step edge, while the terraces were inactive. (B) Like in (A), the noise features appear close to the upper edge of the step. As the profile given below the image indicates, in some cases, the most active centers were not directly at the edge yet still next to an edge site. Data published in Ref. [216].

## Highly Resolved Active Sites for the Hydrogen Evolution at Model Carbon Surfaces

The graphs below the images give example profiles along a line with no active sites (black) and a line including an active step site (red). The atomic pattern of HOPG was recognizable in both images. Here, noise features were located either directly on the upper edge of the step (*e.g.*, as in the profile along the red line given below Figure 6.5A) or in the second row of atoms along the edge (*e.g.*, as in the profile along the red line given below Figure 6.5B).

Further experiments are provided in Figure 6.6A. Figure 6.6A shows a double step, where the upper edge was full of active sites. Interestingly, the first step does not appear to be particularly active; only a few noise spikes can be found along its edge. The graph below gives an exemplary profile along the black line in the image. It shows four noise spikes within the first nanometer of the upper edge, indicating again that the most active sites can be found in the vicinity of steps. Similar to Figures 6.5A and B, the single step in Figure 6.6B was active along the edge.

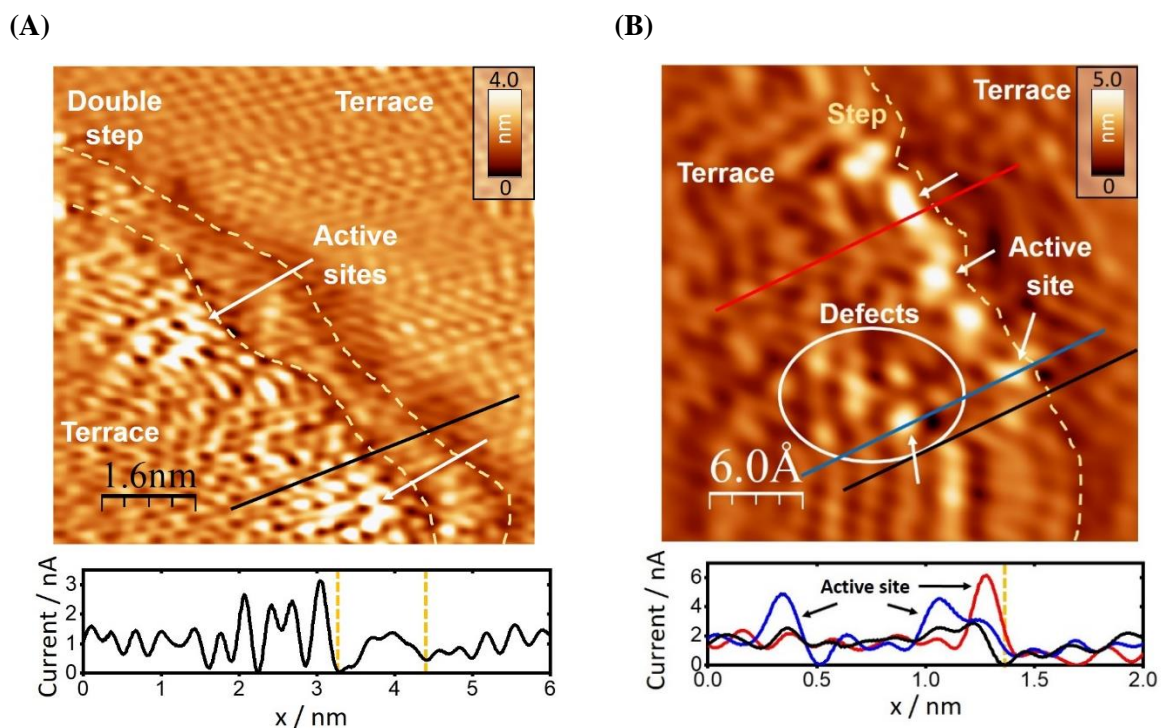


**Figure 6.6** High-resolution n-EC-STM measurements under HER conditions (A:  $-1.15 \text{ V}_{\text{Pt}}$ , B:  $-1.20 \text{ V}_{\text{Pt}}$ ). (A) In this image, many active sites can be found along the upper edge of a double step. The terraces show the typical atomic pattern of the HOPG. (B) Besides active step sites, this image captures a defective area. As the blue profile below the image shows, defective sites can be active, similar to the step sites. Data published in Ref. [216].

Additionally, in this image, an area with some defects was captured (marked by a white circle in the picture). Interestingly, there are several noise peaks in this area, indicating the presence of active sites. As the graph below this image shows, the defective area (as in the blue profile) exhibited a noise feature very similar to an active edge site (compare the blue and red profiles). To summarize, the images suggest that the most active sites are located close to the step edges and defects, while the basal plane is mainly inactive. In the following, the results will be discussed utilizing extensive DFT calculations on this specific model system.

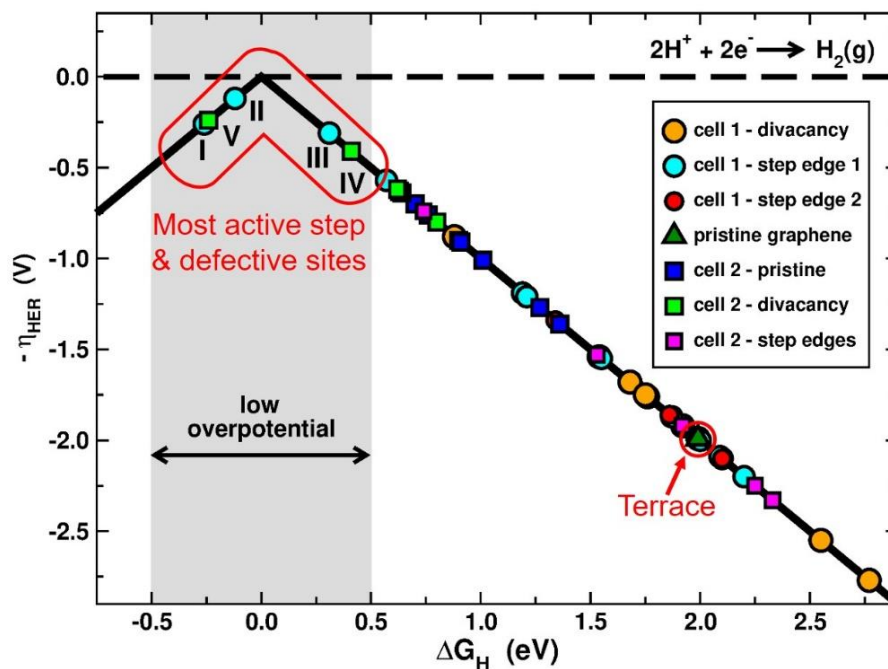
### 6.4 Discussion

In order to serve as a catalyst for the HER, carbonaceous materials are usually modified via heteroatom doping.<sup>[209,210,211,212]</sup> Consequently, examination of the active sites on pure carbon electrodes has so far not received much attention. Especially since the basal plane of graphene is commonly considered mostly inert.<sup>[220,221,222,223]</sup> Yu *et al.*<sup>[222]</sup> and Laasonen *et al.*<sup>[224]</sup> both evaluated the Gibbs free energy of hydrogen adsorption ( $\Delta G_{\text{H}}$ ) on the pristine graphene surface, obtaining a value of 1.15 eV. Since an ideal catalyst, in this case, would have a  $\Delta G_{\text{H}}$  of 0 eV, these results indicated that  $\text{H}^+$  is not able to adsorb to the surface easily.<sup>[225]</sup> This assumption is reflected by the experiments presented in this chapter, which did not pick up any activity on the HOPG terraces. On the other hand, it is not definitively settled yet, whether the basal plane is completely inefficient as a catalyst, with Unwin *et al.* arguing that it is in principle capable of fast electron transfer.<sup>[226]</sup>

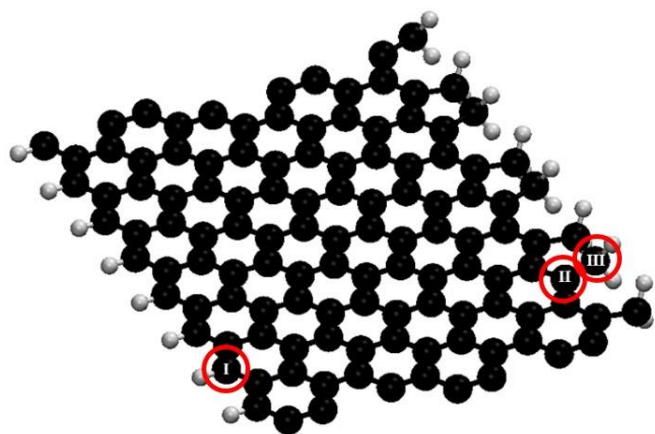
Less is known about the properties of carbon edge and defect sites for hydrogen evolution. Still, there are a few studies that examine these types of sites on related structures such as carbon nanotubes and graphene networks.<sup>[220,222,224,227,228]</sup> For instance, Compton *et al.*<sup>[220]</sup> and Yu *et al.*<sup>[222]</sup> recognized an increased HER performance in their model systems when more edge sites were available. Yu *et al.*<sup>[222]</sup> calculated values of  $\Delta G_{\text{H}}$  as low as -0.38 eV for certain graphene edges, which is considerably closer to the optimum than at the basal plane.

# Highly Resolved Active Sites for the Hydrogen Evolution at Model Carbon Surfaces

(A)



(B)



(C)

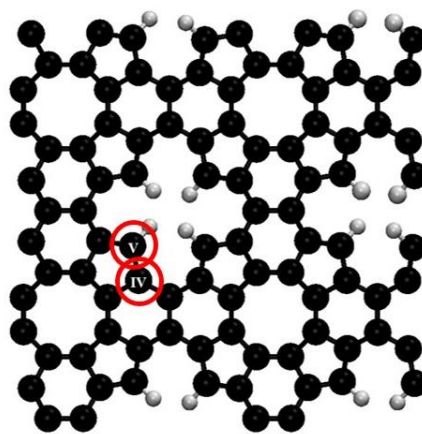


**Figure 6.7** (A) Volcano plot showing the computationally obtained HER overpotential versus  $\Delta G_{\text{H}}$  for various types of sites on graphene. The basal plane (green triangle) is far from the optimum value of  $\Delta G_{\text{H}} = 0$  eV. The sites closest to the optimum are sketched in (B) and (C), with the color code: black - carbon, white - hydrogen. The data suggests that the best positions for HER catalysis on graphene are found near step edges and certain types of defects. Adapted with permission from Ref. [216]. Copyright © 2021, Royal Society of Chemistry.

## Highly Resolved Active Sites for the Hydrogen Evolution at Model Carbon Surfaces

---

To gain a more comprehensive understanding of the nature of the active sites and to support the herein presented experimental data, extensive DFT calculations for the HER on HOPG were provided by Dr. Federico Calle-Vallejo from the Universitat de Barcelona. The results were reported in Ref. [216], in which the properties of numerous edge and defect sites were analyzed. Figure 6.7A shows a volcano plot summarizing the data. Here, the theoretical overpotential for the HER was plotted against  $\Delta G_{\text{H}}$ . As evident, the pristine graphene, *i.e.*, the basal plane of HOPG, is far from the optimum of  $\Delta G_{\text{H}} = 0$  eV. However, there are several sites that reside close to the top of the volcano. These are mainly edge sites as sketched in Figure 6.7B and certain defects as sketched in 6.7C. At these sites,  $\Delta G_{\text{H}}$  values between -0.5 eV and +0.5 eV are predicted. The position of these active sites is in very good agreement with the experimental observations. In fact, the calculations suggest that the best performing site (labeled ‘II’ in Figure 6.7) should be close to but not directly at the edge. Several instances of this case can be identified in the presented n-EC-STM images. Furthermore, it can be assumed that the several rows of active sites in Figure 6.6A did not originate just from the edge but also from defective sites close to the step. According to the calculations, there are also many step and defective sites that do not offer beneficial binding conditions, which could be the reason why in most of the images, only a few sites showed activity.

Besides the insight regarding the catalysis of the HER, this is the first study to visualize active sites with atomic resolution using n-EC-STM. The presented images showed the typical ‘honeycomb’ structure of HOPG and elicited the position of the active sites thereon. The DFT calculations complemented the experimental observations, confirming that the most active sites should indeed be expected at the locations determined by the n-EC-STM measurements.

In summary, the active sites of HOPG for the HER were identified near steps and certain defects. DFT calculations were used to support the experimental results. With these insights, it is possible to tailor the HER activity of carbon electrodes for the desired purpose, *i.e.*, either promoting or suppressing the reaction. According to the investigated HOPG model system, carbon-based catalysts should be designed involving many defects and step edges. In contrast, carbon utilized as a conductive agent in, *e.g.*, battery applications should be mostly defect-free. Moreover, the results demonstrated the ability of the n-EC-STM technique to reveal the active

## Highly Resolved Active Sites for the Hydrogen Evolution at Model Carbon Surfaces

---

centers with unrivaled atomic precision. This is yet another valuable asset for the experimental analysis of catalytic systems.

Highly Resolved Active Sites for the Hydrogen Evolution at  
Model Carbon Surfaces

---

## 7 Active Sites for Alkaline Oxygen Reduction and Evolution Catalysis on Graphite

Carbon-based materials are a promising class of electrocatalysts for oxygen reduction and evolution reactions in an alkaline environment. The prospect of using them as bifunctional catalysts makes them a captivating subject for research purposes. Current studies in this area cover a wide range of structures, from pure to doped variants.<sup>[151,153,208,229,230,231,232,233,234]</sup> In this chapter, n-EC-STM was employed to in-situ discover the active sites for ORR and OER on pure HOPG samples. The investigation probed the electrocatalytic behavior of the basal plane, edge plane, and defective sites in alkaline solution. The results are discussed with the aid of literature reports on similar model systems.

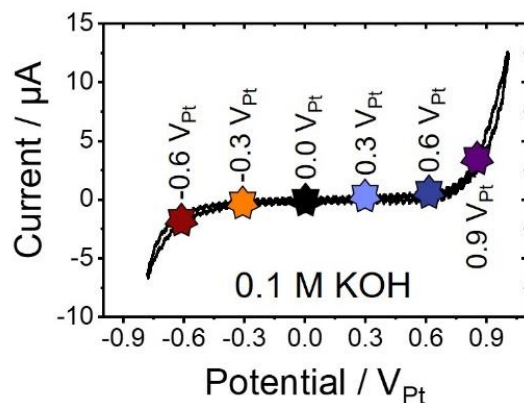
Major parts of this chapter are based on the publication:

*Haid, R. W.<sup>1</sup>; Kluge, R.M.<sup>1</sup>; Schmidt, T.O. and Bandarenka, A. S. In-situ detection of active sites for carbon-based bifunctional oxygen reduction and evolution catalysis, *Electrochimica Acta* **2021**, 382, 138285.<sup>[235]</sup>*

### 7.1 n-EC-STM at Terraces and Step Sites

For the intended measurements, the electrochemical setup in the EC-STM was equipped with a Pt quasi-RE and a carbon CE. The electrolyte used for the experiments was 0.1 M KOH, which was prepared by dissolution of potassium hydroxide pellets (Sigma Aldrich, 99.99% trace metal basis) in ultrapure water (Evoqua, 18.2 M $\Omega$  cm). The sample preparation followed the procedure outlined in Chapter 6.1. As a first step, a CV of the HOPG was recorded in the EC-STM setup to determine the potential regions for ORR ‘On’, OER ‘On’ and reactions ‘Off’. Figure 7.1A shows the CV and marks several potential levels between -0.6 V<sub>Pt</sub> and +0.9 V<sub>Pt</sub>. At 0.0 V<sub>Pt</sub>, the current was practically zero, and therefore one can assume all reactions are ‘Off’ at

(A)



(B)

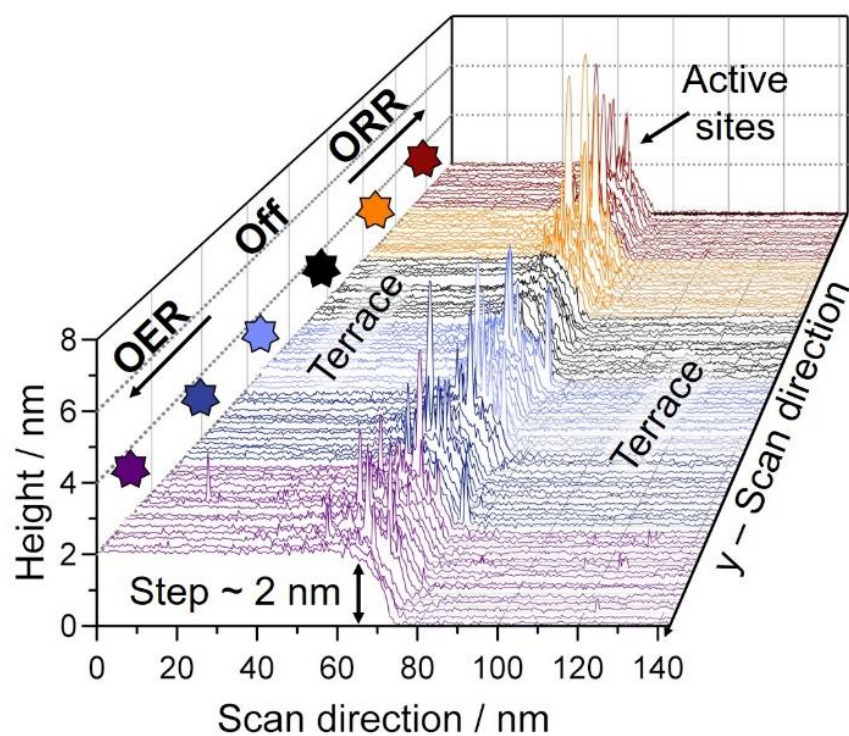
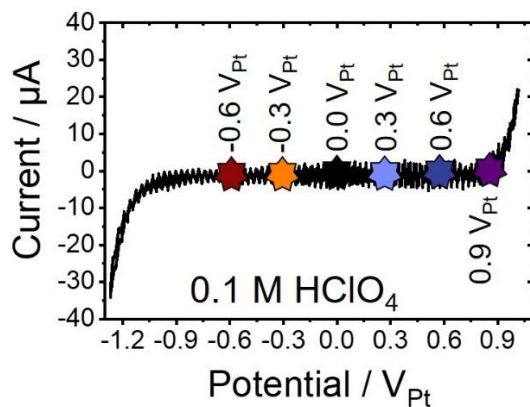


**Figure 7.1** (A) CV of HOPG in the EC-STM setup in 0.1 M KOH (scan rate 50 mV/s). The indicated potential levels between  $-0.6 V_{Pt}$  and  $+0.9 V_{Pt}$  were used for the experiments. (B) n-EC-STM data of a typical surface structure. The color of the scan lines indicates the applied potential, as marked by the stars in the CV in (A). Under ORR and OER conditions, the step edge showed large noise spikes, while the terraces remained largely noise-free. Data published in Ref. [235].

## Active Sites for Alkaline Oxygen Reduction and Evolution Catalysis on Graphite

(A)



(B)

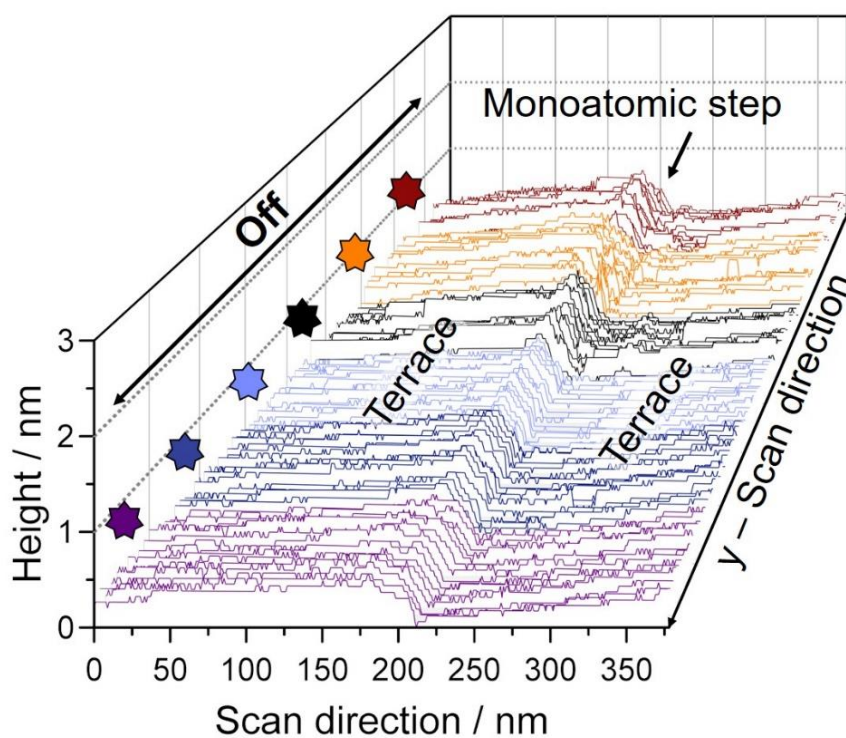


**Figure 7.2** (A) CV of HOPG in the EC-STM setup in 0.1 M  $\text{HClO}_4$  (scan rate 50 mV/s). Contrary to the alkaline environment, HOPG showed no activity in the investigated potential range ( $-0.6 V_{\text{Pt}}$  to  $+0.9 V_{\text{Pt}}$ ) in the acidic electrolyte. (B) As expected, neither terrace nor step displayed noise at the applied potentials. Consequently, one can assume that the spikes in the STM signal in (B) were triggered by the ongoing electrochemical processes. Data published in Ref. [235].

this point. Moving toward negative potentials resulted in currents that originate from the ORR, whereas the current increase at positive potentials was connected to the OER. Higher positive and negative potentials were avoided in the experiments, resulting in large current densities, which could damage the sample and scanning probe. In Figure 7.1B, n-EC-STM scans at each of the indicated potentials are shown for two large terraces interrupted by an approx. 2 nm high step (~6 layers of graphene). Comparing the structures at 0.0 V<sub>Pt</sub> (reactions ‘Off’) to the other potentials, large noise spikes at the top of the step edge are noticeable under the reaction conditions. On the other hand, the terraces exhibited no noise when going to reaction conditions except at the highest applied potential.

Before continuing this line of investigation with further experiments, it is necessary to exclude that the noise at the step edge is simply a measurement artifact not connected to interfacial processes. For this purpose, the experiment was repeated with identical settings in an acidic electrolyte (0.1 M HClO<sub>4</sub>). In this case, the HOPG should be inactive in the applied potential range (*cf.* CV in Figure 7.2A). Indeed, as shown in Figure 7.2B, a similar surface structure exhibited neither noise on the terraces nor at the step. Furthermore, it should be noted that the scans were always taken with the tip moving from the upper terrace towards the lower terrace. This way, artificial noise caused by an ‘overshoot’ of the feedback system at the step edge should be minimized.

## 7.2 Monitoring a Larger Surface Area

Having shown that the noise in Figure 7.1B can be assumed to be related to the electrochemical processes, the experiment was repeated over a larger surface region. The images in Figure 7.3A-F extended over an area of 500 x 500 nm and were taken at approximately the same position. They show a surface structure comprising several distinct features, such as steps, terraces, and defects. For more clarity, Figure 7.3G provides line scans at roughly the same position for each sub-image, indicated by the black dotted lines in Figures 7.3A-F. The active sites were identified by comparing the images under reaction conditions to the scan at 0.0 V<sub>Pt</sub> (Figure 7.3C), where the reactions are ‘Off’. At negative potentials (ORR conditions), the most

## Active Sites for Alkaline Oxygen Reduction and Evolution Catalysis on Graphite

active sites were found at the step edge and defects. The noise at these sites became more intense at the more negative potential (Figure 7.3B), accounting for the higher activity at this point.

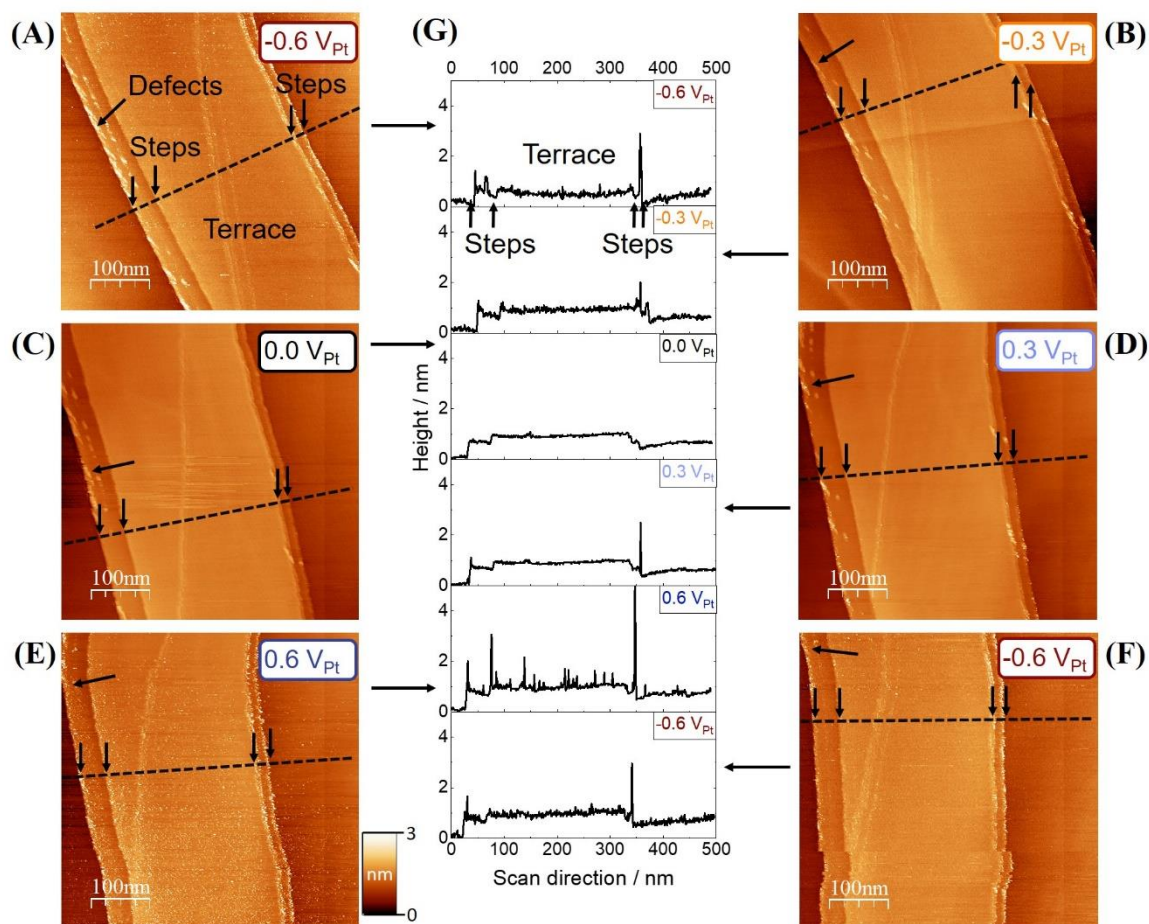


**Figure 7.3** n-EC-STM images of a surface structure including several steps, terraces, and defects at different potentials. (A) At  $-0.6 \text{ V}_{\text{Pt}}$ , the noise was predominantly found at the steps and defects. (B) At  $-0.3 \text{ V}_{\text{Pt}}$ , the noise was at the same position as in (A); however, less intense. (C) When the applied potential was  $0.0 \text{ V}_{\text{Pt}}$ , all reactions were ‘Off’, and the surface was completely noise-free. (D) At  $0.3 \text{ V}_{\text{Pt}}$ , noise spikes were again found at the steps and defects. (E) At a potential of  $0.6 \text{ V}_{\text{Pt}}$ , the noise started to spread over the entire image. To test the impact of this activity on the surface quality, the potential was changed back to  $-0.6 \text{ V}_{\text{Pt}}$  for image (F). The resulting image showed no apparent difference to (A). Thus, it can be assumed that the surface is not corroded at the potential applied in (E). For clarity, the graphs in (G) provide line scans taken from approximately the same position in (A)-(F), as indicated by the black dotted line in the respective image. Data published in Ref. [235].

The noise was again found in the positive potential region, mainly at the step edges and defects (*cf.* Figure 7.3D). However, at 0.6 V<sub>Pt</sub>, the activity started to spread over the entire surface. It needs to be considered that this noise could be connected to oxidation of the surface resulting in corrosion. The potential was changed back to ORR conditions (-0.6 V<sub>Pt</sub>, Figure 7.3F) to test this. Suppose the surface was corroded at the positive potentials. In that case, this should be visible either directly in the surface quality or by a higher ORR activity due to an increased number of defective sites (which are active ORR sites). However, comparing Figure 7.3F and A, neither seems to be the case, which leads to the assumption that there is a potential where the OER takes place on the surface of HOPG without causing corrosion.

### 7.3 High-Resolution of ORR Active Sites

After establishing the positions of the most active sites, it would be interesting to monitor their behavior under reaction conditions more closely. To this end, some surface sites, including step edges, were recorded with higher resolution (in the constant height mode) under ORR conditions. Figure 7.4A shows a very defective/irregular step, where various active sites can be found at the upper edge. In Figure 7.4B, an area with several steps in a row was captured. The bright noise spots indicate that the edge plane (stepped area) is considerably more active than the basal plane (terraces). Figures 7.4C and D were recorded at approximately the same position, once at -0.5 V<sub>Pt</sub> and once at -0.7 V<sub>Pt</sub>. It becomes apparent that close to the onset, only a few sites were active, such as the 'α'-site indicated in the image. At the higher potential, more surface sites became active, such as the 'β'-site in the images. The difference in the signal at this site for the two potentials can be seen in the graph below the images, which gives the current profile along the black line in the respective image. At -0.5 V<sub>Pt</sub>, the tip tracked the step accurately at this position, while at -0.7 V<sub>Pt</sub>, the edge site was superimposed by a noise spike. These findings are in line with the observations made in Figures 7.3A and B, where more sites were active at a more negative potential. All images in Figure 7.4 were treated with the FFT tool in the WSxM software to elicit the surface structures more clearly.

## Active Sites for Alkaline Oxygen Reduction and Evolution Catalysis on Graphite

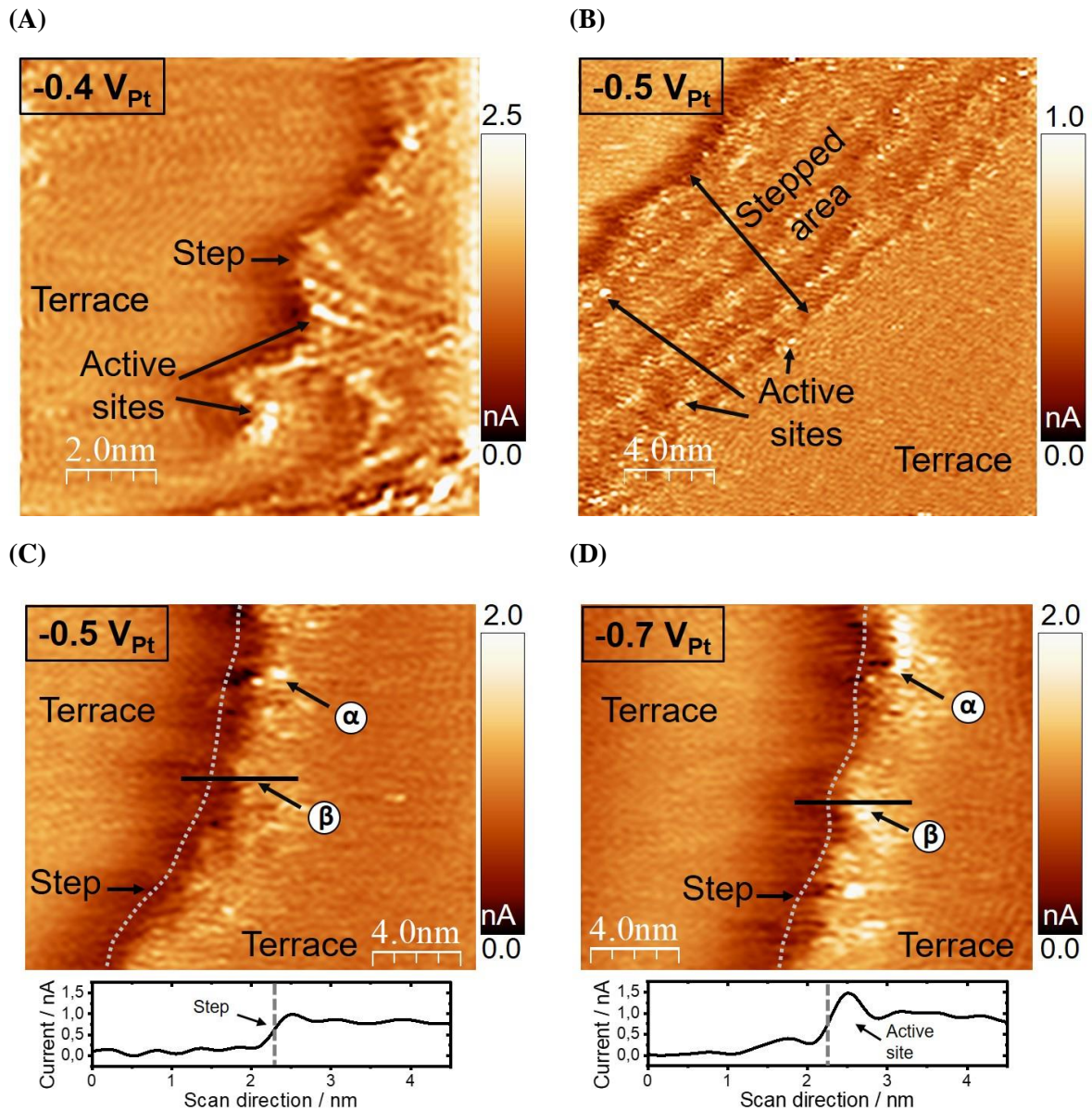


**Figure 7.4** High-resolution n-EC-STM images of step edges under ORR conditions. (A) A defective/irregular step with active sites at the upper edge, as indicated in the image. (B) Image of a stepped area next to a large terrace. The edge plane (stepped area) showed activity, while the basal plane (terraces) were largely inactive. (C) and (D) show measurements of the same step at two different potentials in the ORR region. At the potential closer to the reaction onset ( $-0.5 \text{ V}_{\text{Pt}}$ ), fewer sites were active than at a potential deeper in the ORR region ( $-0.7 \text{ V}_{\text{Pt}}$ ). For instance, the site indicated as ‘ $\alpha$ ’ was active in both cases, whereas the site ‘ $\beta$ ’ only became active at the more negative potential. Data published in Ref. [235].

## 7.4 Discussion

Based on the results presented in this chapter, several discussion points regarding the active sites for the ORR and OER on HOPG can be addressed. Generally speaking, the active sites can be directly identified in the n-EC-STM images by the increased noise level under reaction conditions compared to the scans at 0.0 V<sub>Pt</sub> (reaction ‘Off’). With this in mind, the data suggested that the active sites for the ORR/OER are located close to edge sites and defects. The terraces were inactive for the ORR. However, they played a role in the OER at higher potentials. Furthermore, comparing Figures 7.3A and B, an increasing intensity in the noise level was observed when the current resulting from the ORR was higher. This was confirmed by the high-resolution images in Figures 7.4C and D. Here, it became clear that not the entire step is active at every potential. It rather appears with increasing potential, more and more edge sites are activated to participate in the catalysis. A similar effect can be seen for the OER in Figures 7.3D and E.

These findings agree well with other experimental and theoretical studies on similar systems.<sup>[208,229,236,237,238,239,240,241]</sup> In the experimental studies, it was suggested that the edge plane is considerably more active towards the ORR than the basal plane.<sup>[236,237,238]</sup> Additionally, several groups used DFT approaches to predict which surface sites should be most active on graphitic materials.<sup>[208,229,239,240,241]</sup> To help this discussion, Figure 7.5 shows sketches of some of the most common types of defects and edges on HOPG. The underlying reason for the different properties of these surface sites seems to be the modification of the sp<sup>2</sup> matrix of the

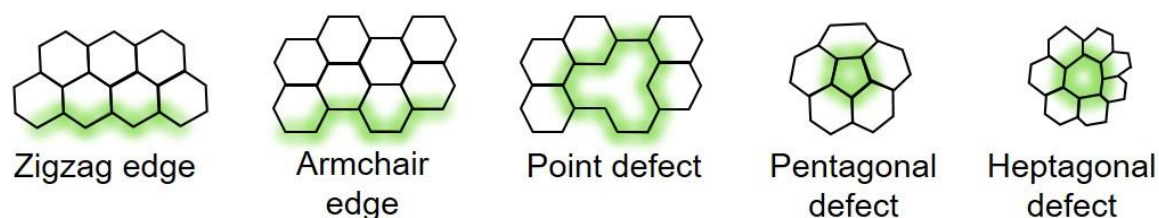


**Figure 7.5** Most common edges and topological defects on HOPG. Due to the modification of the electronic properties at these sites, the catalytic activity towards ORR and OER can be considerably higher compared to the basal plane.

## Active Sites for Alkaline Oxygen Reduction and Evolution Catalysis on Graphite

---

carbon resulting in higher spin and charge densities.<sup>[240]</sup> DFT calculations suggested that particularly zigzag edges, pentagonal, and heptagonal defects are active for the ORR.<sup>[208,229,239,240]</sup> For instance, Hu *et al.* claimed that zigzag edges and pentagonal defects are beneficial for the ORR with theoretical overpotentials of even less than 0.11 V vs the normal hydrogen electrode.<sup>[239]</sup> It is believed that both the two-electron and the four-electron pathways can occur simultaneously at these types of sites. Furthermore, they showed that armchair edges and hole defects are more difficult to activate for the reaction, albeit still preferable to the pristine graphene. With this in mind, the activity at the steps in the n-EC-STM images can be attributed mainly to zigzag edges and ring defects. According to the DFT calculations, it is no surprise that activity can be found close to these sites, even at low overpotentials. Moreover, the cited literature explains the observations in Figures 7.4C and D since various types of edge and defective sites become active for the ORR at different applied potentials.

Similarly, the OER activity on graphene is dominated by edge effects.<sup>[208,229,242]</sup> It has previously been shown that the zigzag edge is more beneficial towards the OER than the armchair edge.<sup>[242]</sup> Furthermore, topological defects can promote the evolution of oxygen. For example, DFT calculations by Wei *et al.* revealed that a combination of pentagonal and heptagonal ring structures can achieve OER overpotentials down to 0.21 V.<sup>[229]</sup> Yao *et al.* reported a theoretical and experimental analysis of defective graphene, concluding that the topological defects lead to low overpotentials for oxygen evolution.<sup>[208]</sup> Both studies obtained OER activities comparable to commercial Ir/C catalysts by designing graphene materials with a large number of defective sites. In this context, the presented n-EC-STM measurements under oxygen evolution conditions complement the literature well. The results directly confirmed that the position of the active sites for the OER is predominantly near edge and defective sites. However, at higher potentials, the images suggested activity on the basal plane too. In this context, it is essential to consider the possibility of surface degradation, which is often caused by the OER.<sup>[242,243,244]</sup> Judging from the comparison of Figures 7.3A and F, which show the surface under ORR conditions before and after going to OER potentials, it is likely that the surface was not damaged in this instance. Besides, the introduction of defects due to surface

## Active Sites for Alkaline Oxygen Reduction and Evolution Catalysis on Graphite

---

roughening should increase the ORR activity, which did not appear to be the case. Therefore, it can be assumed that the surface is stable in this setup in the applied potential range.

In summary, the ORR and OER active sites of HOPG were identified using n-EC-STM. For both reactions, the highest activity was found along step edges and defective sites. The basal plane remained largely inactive in the applied potential range. The results were compared and discussed utilizing theoretical and experimental studies on related model systems. It can be concluded that graphene can be designed to serve as an excellent bifunctional ORR/OER catalyst with commensurate durability in alkaline solution by the introduction of highly active topological defects.

## 8 Monitoring the Oxygen Evolution on Manganese Oxide Nanosheets

In nature, manganese oxides ( $\text{MnO}_x$ ), in the form of  $\text{CaMn}_4\text{O}_5$ , are a fundamental component for water splitting in photosystem II. Consequently, this material class has attracted much attention in the search for suitable OER catalysts.<sup>[245,246,247,248,249]</sup> In comparison to the state-of-the-art OER catalysts such as  $\text{RuO}_2$  and  $\text{IrO}_2$ , it possesses the additional advantage of a relatively high abundance and, therefore, low cost. However,  $\text{MnO}_x$  has many structural variations, complicating the analysis of its inherent activity towards a given reaction.<sup>[250]</sup> Researchers have tested the properties of a wide variety of  $\text{MnO}_x$  complexes, of which some turned out as insufficient OER catalysts, while others were competitive to  $\text{RuO}_2$  and  $\text{IrO}_2$ .<sup>[251,252,253,254,255,256,257,258,259]</sup> According to the general consensus, the key components for high electrocatalytic activity are, in most cases, the  $\text{Mn}^{3+}$  oxidation state and lattice vacancies.<sup>[248,253,257,260]</sup> Close to the OER onset,  $\text{Mn}^{3+}$  is formed by charge comproportionation from  $\text{Mn}^{2+}$  and  $\text{Mn}^{4+}$  ( $\text{Mn}^{2+} + \text{Mn}^{4+} \rightarrow 2 \text{Mn}^{3+}$ ).<sup>[260,261]</sup> It is believed that this configuration is beneficial for both charge transfer and adsorption of reaction intermediates. However, it is also often deficient in stability, especially in acidic and neutral solutions.<sup>[248,262]</sup> In contrast to the available studies on the most active oxidation states, much less attention has been given to the influence of morphological features on the catalytic performance of  $\text{MnO}_x$  complexes. With this in mind, the following experiments target the elucidation of the structure-activity relationship for the OER on  $\text{MnO}_2$  nanosheets ( $\text{MnO}_2\text{-NS}$ ), deposited on a modified HOPG substrate. The results are obtained by n-EC-STM measurements and discussed using related literature reports.

## 8.1 *Ex-situ* Characterization of the Sample System

The here-investigated samples were kindly prepared by the group of Jun Maruyama at the Osaka Research Institute of Industrial Science and Technology, following the procedure outlined in Ref. [263]. In short, a pristine HOPG surface was modified by a carbonaceous iron-porphyrin film (HOPG-CFePc) and subsequently decorated with MnO<sub>2</sub>-NS (HOPG-CFePc-MnO<sub>2</sub>-NS). It is important to note that after the application of the FePc film, the soluble

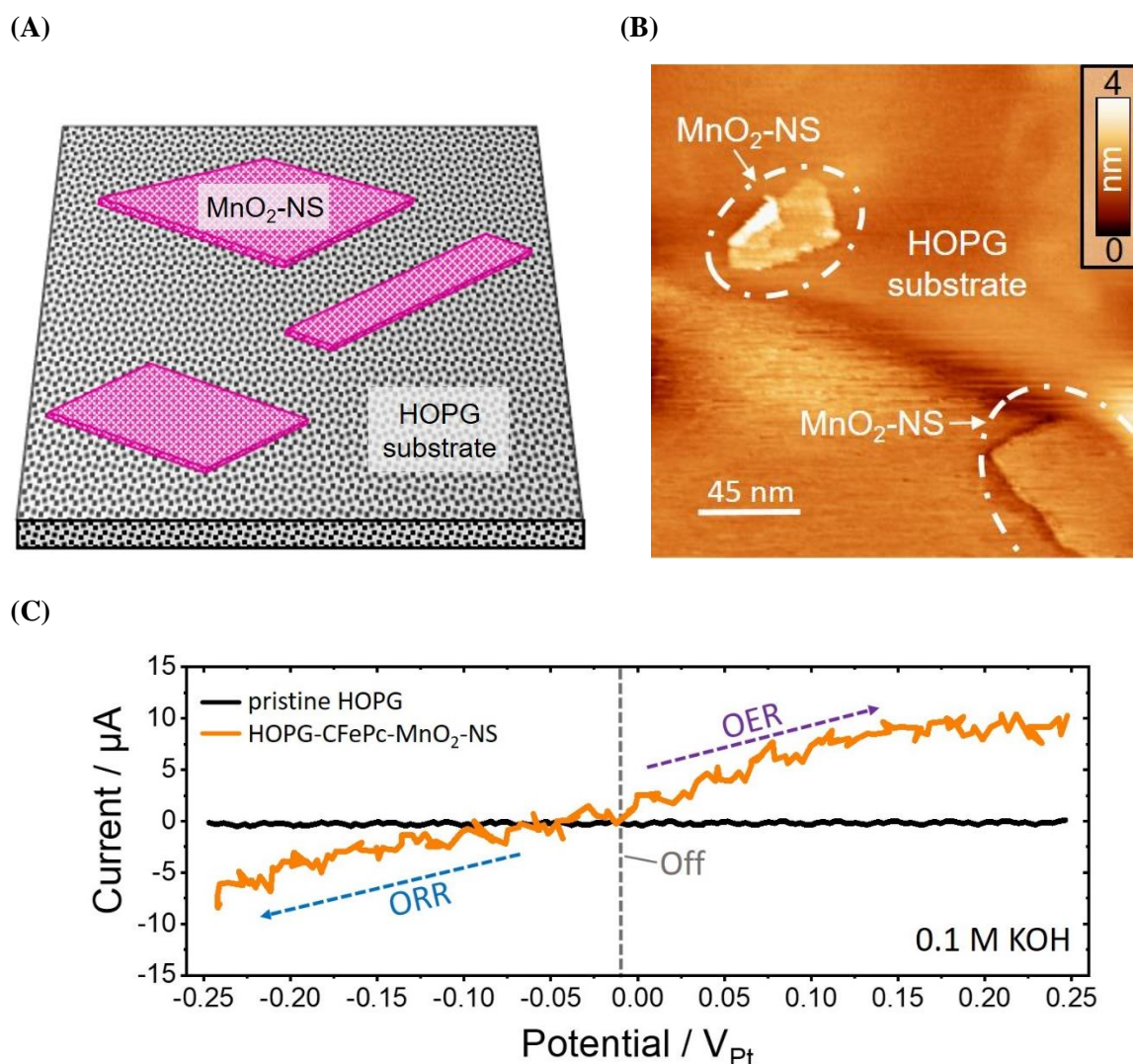


**Figure 8.1** (A) Sketch and (B) STM image of the MnO<sub>2</sub>-NS on the HOPG substrate. (C) LSV of the sample system and a pristine HOPG reference in the EC-STM setup (0.1 M KOH, scan rate 50 mV/s). The HOPG-CFePc-MnO<sub>2</sub>-NS exhibited a notably higher current than the pristine HOPG already at low positive potentials, which according to Ref. [263] can be ascribed to the OER.

## Monitoring the Oxygen Evolution on Manganese Oxide Nanosheets

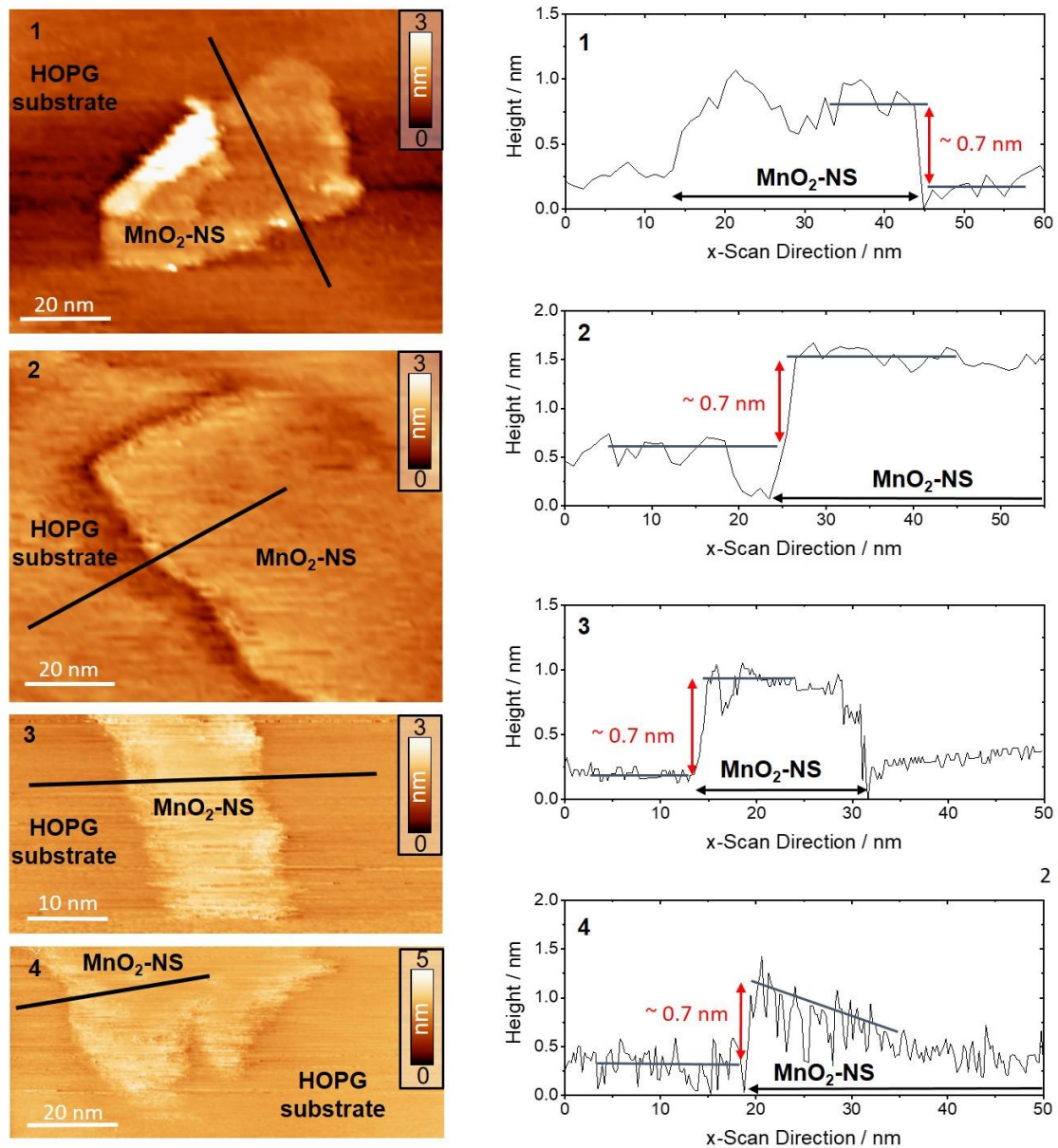


**Figure 8.2** Ex-situ STM images of MnO<sub>2</sub>-NS on the modified HOPG substrate. The NS showed a typical height of approximately 0.7 nm.

Fe species were effectively removed by an acid treatment. Apart from the intrinsic activity of the coating, it mainly acts as an anchor to stabilize the MnO<sub>2</sub>-NS on the HOPG surface. Figure 8.1A gives a schematic representation of the sample structure, and Figure 8.1B provides an STM image of the as-prepared sample, showing the nanosheets on the carbon surface. The EC-STM experiments were carried out in 0.1 M KOH solution with a carbon CE, to avoid the

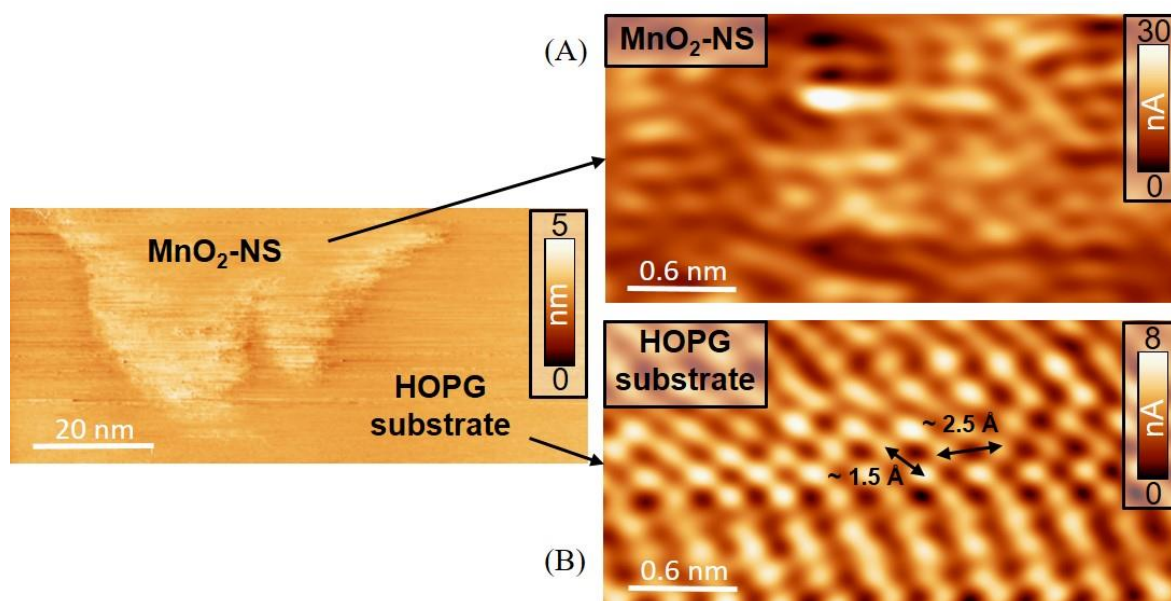


**Figure 8.3** To further differentiate between HOPG and  $\text{MnO}_2\text{-NS}$ , the atomic pattern of the two materials were analyzed with high-resolution scans. (A) On the  $\text{MnO}_2$ , the structure could not be fully resolved. Still, a clear difference was recognizable in comparison to (B) the HOPG substrate. Here, the typical atomic pattern was visible.

deposition of foreign species. According to the RDE activity tests in Ref. [263], the samples with  $\text{MnO}_x$  exhibited high OER performances compared to pure HOPG, particularly at low overpotentials. As Figure 8.1C shows, this behavior was also observed in the EC-STM setup. The LSV curve suggests that already at low positive potentials ( $< 0.3 \text{ V}_{\text{Pt}}$ ) some activity can be expected at the  $\text{MnO}_2\text{-NS}$ . Higher potentials were avoided during the LSV in order to prevent degradation or corrosion of the sample. It should be noted that the CFePc itself also affects the OER activity, which is briefly addressed in Appendix D.

In the STM measurements, it is not straightforward to distinguish chemical species. Therefore, one of the major challenges of using samples with multiple elements, such as in this case the HOPG and the  $\text{MnO}_2$ , is to identify them in the scans. The most meaningful way is to evaluate their structural properties, especially the typical layer size and the atomic pattern. For the  $\text{MnO}_2\text{-NS}$ , the height of one monolayer equals around 0.7 nm.<sup>[256,262,264,265]</sup> With this in mind, Figure 8.2A gives a collection of STM images showing sheet-like surface structures and provides an individual line scan across each structure.

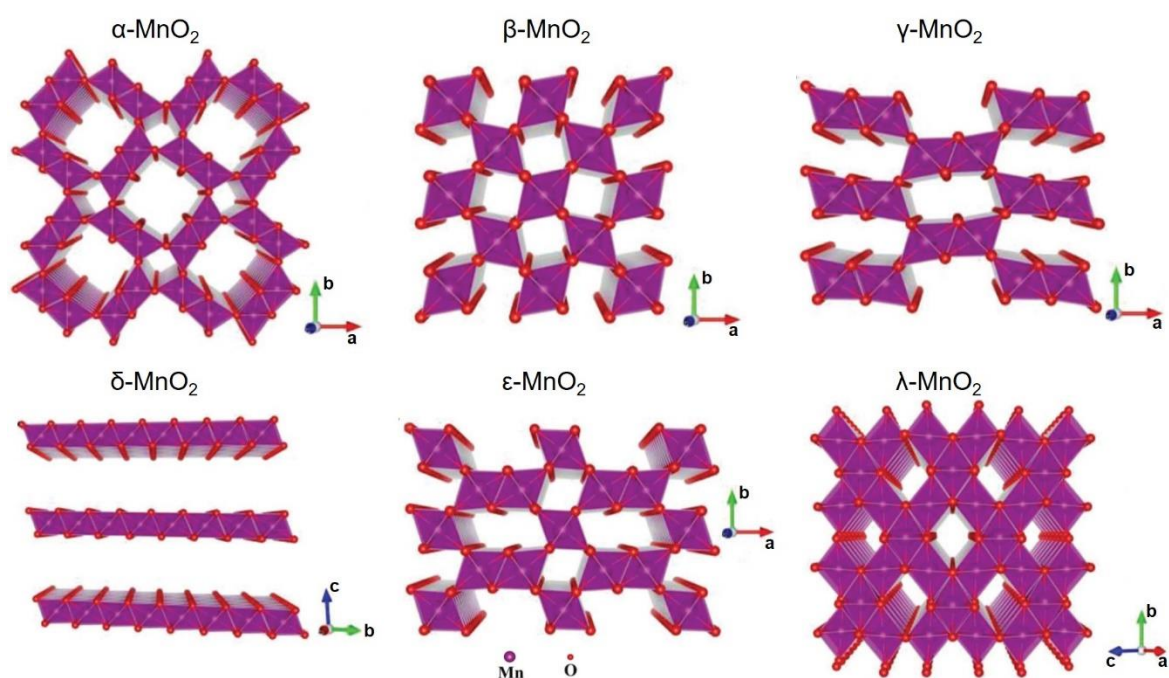


**Figure 8.4** There are many ways in which  $\text{MnO}_x$  can arrange.<sup>[250]</sup> Here, the typical configurations of  $\alpha$ -,  $\beta$ -,  $\gamma$ -,  $\delta$ -,  $\epsilon$ -, and  $\lambda$ - $\text{MnO}_2$  are summarized. As it was not possible to resolve the pattern and periodicity of the  $\text{MnO}_2$ -NS clearly in the STM images, there might have been a combination of several structures present. Adapted with permission from Ref. [267] Copyright © 2018, John Wiley and Sons.

The shapes of the captured structures closely resembled the ones of similar model systems found by other research groups.<sup>[264,265,266]</sup> Moreover, in all cases, the height of the sheets was approximately 0.7 nm. Still, these indicators are not sufficient evidence to distinguish the NS from the HOPG, as a double step on the latter would be of a similar height (0.67 nm). It is, however, noteworthy that HOPG steps typically take the form of sharp edges extending several micrometers laterally, unlike the sheet-like structures found in Figure 8.2. Still, the atomic pattern of the two surfaces was probed to provide additional confirmation of the correct distinction. Figure 8.3A and B show high-resolution STM images of the presumed  $\text{MnO}_2$ -NS and HOPG areas of the structure in Figure 8.3 (left). The pattern in Figure 8.3B closely resembled HOPG, albeit with some lattice distortions. These can be attributed to the preparation process of the sample. Figure 8.3A shows a decidedly different arrangement, although a clear atomic pattern could not be discerned in this case. It is, therefore, likely that the surface of the NS was partially disordered and consisted of a combination of typical  $\text{MnO}_2$  structures.

The most common variations of  $\text{MnO}_2$  are sketched in Figure 8.4. The inter-atomic distances of these structures range from 0.19 nm to 0.46 nm, which is in general agreement with the scale of the features in Figure 8.3A.<sup>[267]</sup> Following this clarification of the specifications of the sample components, the activity of the  $\text{MnO}_2$ -NS was investigated with the n-EC-STM technique.

### 8.2 Active Sites of $\text{MnO}_2$ -NS under Oxygen Evolution Conditions

In Figure 8.5A, an n-EC-STM image of an  $\text{MnO}_2$ -NS is given. As indicated, the upper part of the image was taken under the application of an OER potential ( $0.6 V_{\text{Pt}}$ ), while for the lower part the reaction was switched ‘Off’. Figure 8.5B shows the same structure, however, in this case, the potential sequence was reversed, *i.e.* for the upper part the reaction was ‘Off’ and in the lower part, it was switched ‘On’. In these 3D perspectives, the noise spikes appearing under reaction conditions at the  $\text{MnO}_2$ -NS were visible, indicating its activity. The HOPG substrate on the other hand remained largely inactive at the applied potentials. As would be expected,

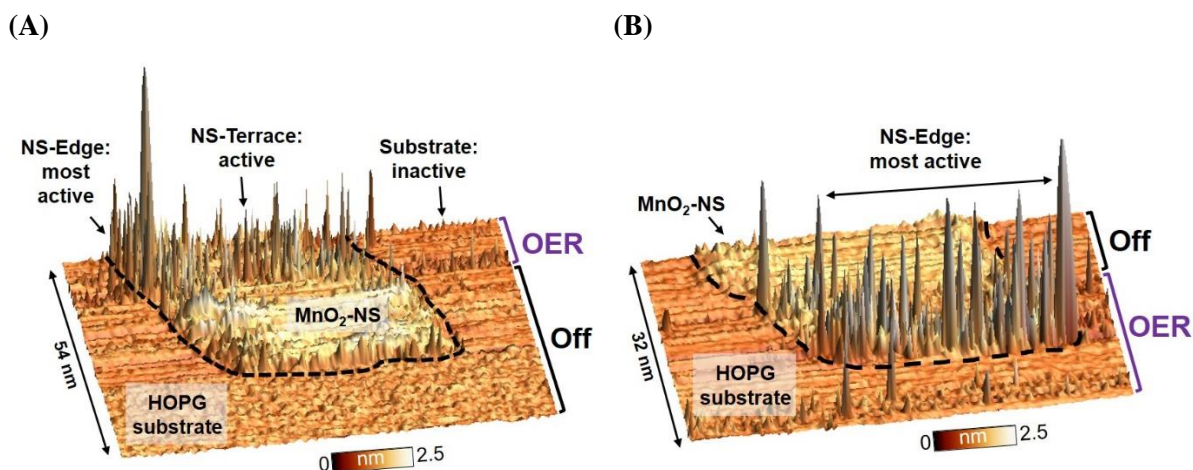


**Figure 8.5** n-EC-STM measurements of a  $\text{MnO}_2$ -NS under OER conditions ( $0.6 V_{\text{Pt}}$ ). (A) Here, the upper part of the image was taken while the OER was occurring. Noise spikes can be found on the NS terrace and at the NS edge, while the HOPG substrate was largely inactive. Once the reaction was turned ‘Off’, the noise subsided *i.e.* everything was noise-free. (B) The image shows the same structure as in (A), however, in this case, the reaction ‘On’ and ‘Off’ sequence was reversed. Again, while there is no reaction enforced, the surface was noise-free. After switching the OER ‘On’, noise appeared on the  $\text{MnO}_2$ -NS, where particularly along the edge high spikes in the signal were observed.

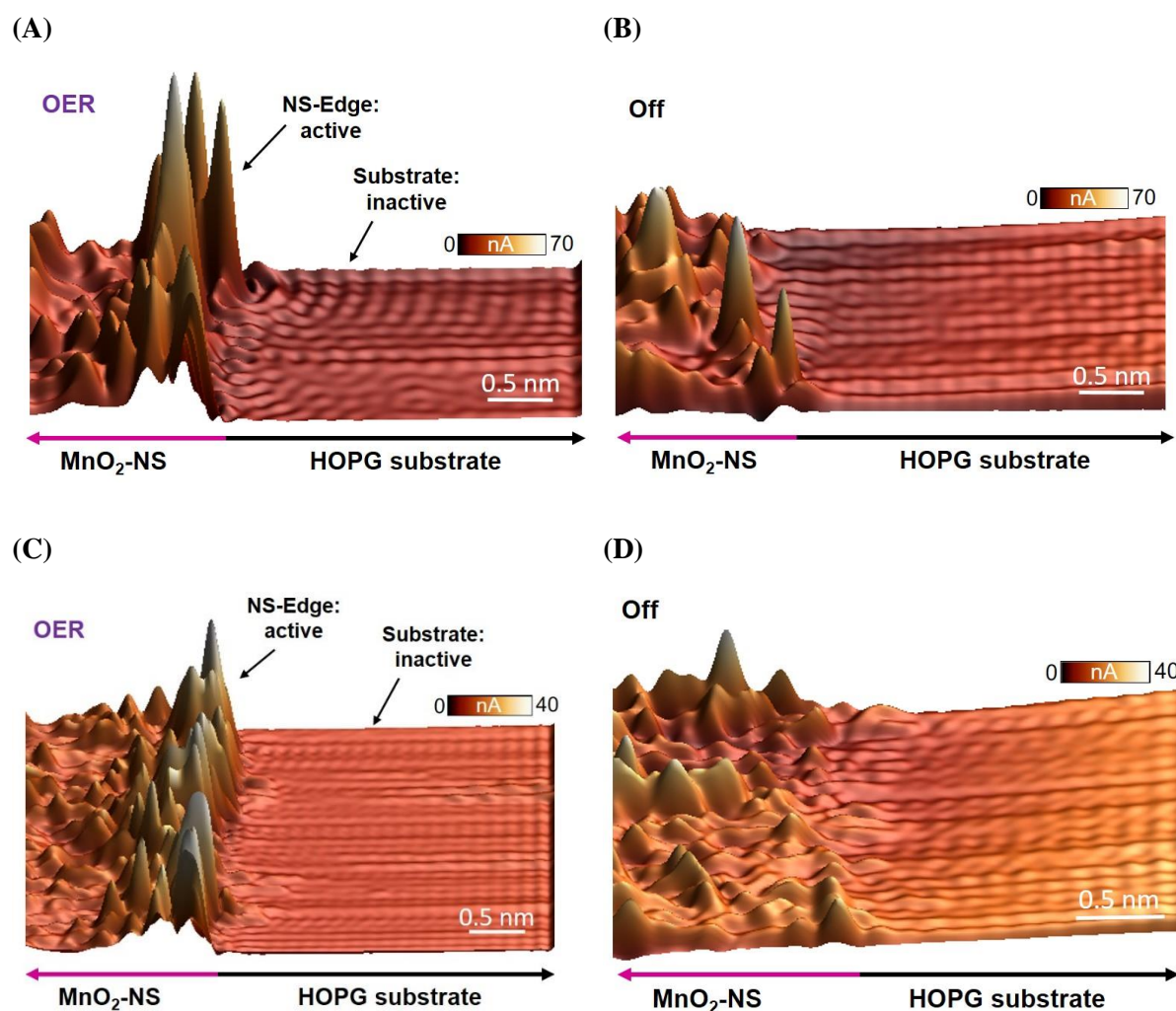


**Figure 8.6** High-resolution n-EC-STM measurements of a MnO<sub>2</sub>-NS edge. (A) Under OER conditions (0.3 V<sub>Pt</sub>), noise spikes were observed at the edge of the NS, which disappeared when the reaction was turned ‘Off’ as is visible in (B). The atomic pattern, especially of the HOPG substrate, was recognizable in both images. (C) and (D) show a repetition of the experiment. Again, the noise was observed predominantly at the edge under OER conditions, suggesting active sites at this position.

when the reaction was turned ‘Off’, the signal was noise-free since the reaction was suppressed. Besides these observations, the figures suggest a higher OER activity along the edges of the NS, as here the noise spikes are higher and more intense than at the terrace of the NS. To further investigate the activity of the edge sites, high-resolution measurements across MnO<sub>2</sub>-NS edges were carried out. Figure 8.6 shows a MnO<sub>2</sub>-NS edge (A) under OER conditions and (B) with the reaction switched ‘Off’. In both cases, the atomic pattern of the HOPG substrate adjacent

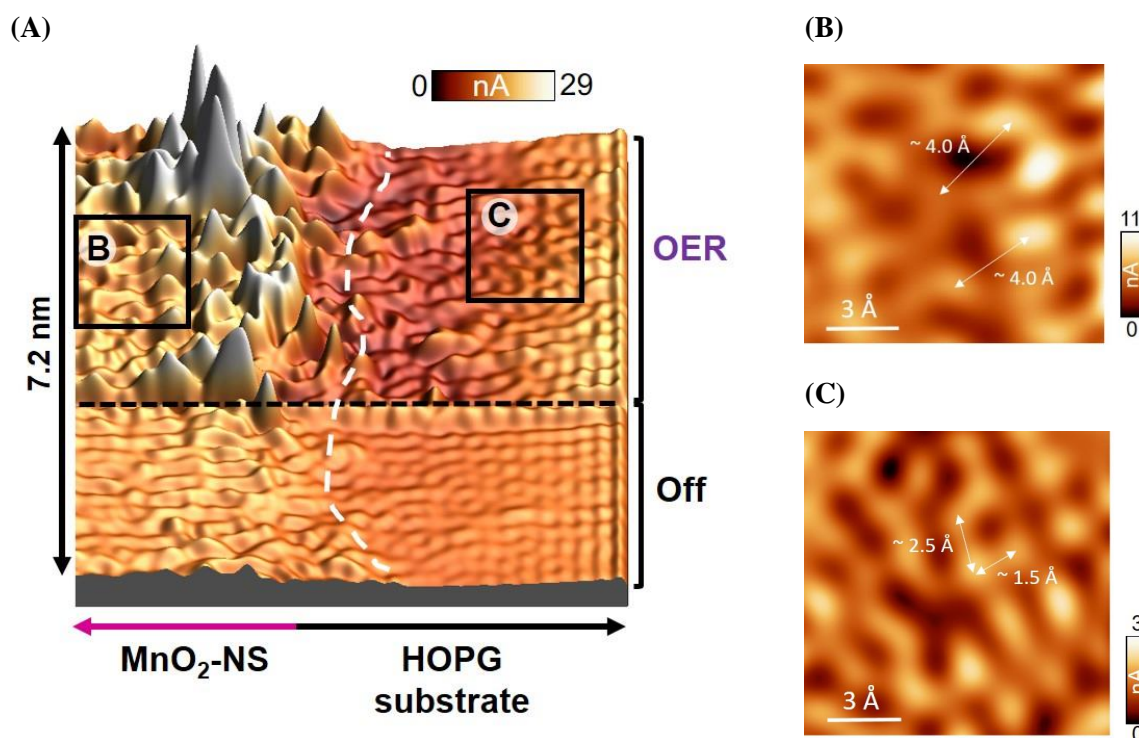


**Figure 8.7** High-resolution of an  $\text{MnO}_2$ -NS edge where the reaction was switched from ‘On’ ( $0.3 V_{\text{Pt}}$ ) to ‘Off’ during the scan. The difference of the signal for the two cases provides direct evidence of the active sites along the edge. In (B) and (C) a small section from the  $\text{MnO}_2$  and HOPG areas was analyzed to confirm the material components. As in the preliminary analysis in Figure 8.3, the HOPG pattern can be recognized fairly well, while the structure of the  $\text{MnO}_2$  was not entirely resolvable. Still, the general shape and inter-atom distances resembled typical  $\text{MnO}_2$  configurations, as *e.g.*, shown in Figure 8.4.

to the  $\text{MnO}_2$ -NS edge can be readily distinguished. In line with Figure 8.5, under reaction conditions, high noise spikes appeared at the NS edge. This behavior was confirmed by the repetition of the experiment in Figure 8.6C (OER ‘On’) and D (OER ‘Off’). Again, noise spikes along the  $\text{MnO}_2$ -NS edge reflect the local activity, while the HOPG substrate remained inactive.

Figure 8.7 provides further analysis of the active sites and the atomic structure of the surface components. In this case, to directly demonstrate the effect of the reaction, the OER was switched ‘Off’ during the recording in the lower part of the image. As evident, the noise spikes at the edge immediately vanished, and the entire surface turned inactive. Figures 8.7B and C were cut from Figure 8.7A to compare the atomic arrangements of a  $\text{MnO}_2$  and a HOPG section. As visible, the HOPG substrate was well-ordered, and the inter-atomic distances were within

the expectations.<sup>[267]</sup> The MnO<sub>2</sub> part was less easy to characterize. However, the structure was different from the HOPG substrate and more in line with the typical MnO<sub>2</sub> configurations displayed in Figure 8.4.

To recap, the n-EC-STM experiments recorded high noise levels at the MnO<sub>2</sub>-NS while the HOPG substrate remained inactive. The NS edges exhibited an increased noise level compared to the terraces. Following this, edge sites were imaged with high resolution, showing the electronic structures of HOPG and MnO<sub>2</sub>. Under reaction conditions, large noise spikes again appeared at the edges, confirming them as excellent areas for OER catalysis.

### 8.3 Discussion

The presented n-EC-STM measurements targeted the identification of the active sites for the OER on MnO<sub>2</sub>-NS in an alkaline solution. The results indicated activity already at low positive potentials (*vs* the Pt quasi-reference) on the surface of the NS. Using an O<sub>2</sub> sensing technique it has been shown by Maruyama *et al.* that this current is indeed caused by the evolution of oxygen.<sup>[263]</sup> Moreover, the high OER activity of the MnO<sub>2</sub> sheets is in accordance with other studies showing the exceptional performance of MnO<sub>x</sub> based systems.<sup>[251,252,254,255,256,257,264,268]</sup> The origin of this behavior has been extensively analyzed in the literature.<sup>[247,253,254,257,265,268]</sup> Most often, two key factors are pointed out as conditions for efficient OER catalysis. Firstly, the oxidation state of Mn is important, with Mn<sup>3+</sup> being particularly beneficial, introducing a half metallicity to the material.<sup>[249,265,266]</sup> It has been found that under OER conditions, this state is naturally formed by charge comproportionation from Mn<sup>2+</sup> and Mn<sup>4+</sup> ( $\text{Mn}^{2+} + \text{Mn}^{4+} \rightarrow 2 \text{Mn}^{3+}$ ).<sup>[260,261]</sup> It is worth noting that the stability of this configuration depends on the pH of the electrolyte. According to Takashima *et al.*, the stability in acidic and neutral solutions is considerably worse than in alkaline environments.<sup>[262]</sup> Secondly, slight modifications of the electronic structure, particularly variations in the Mn – Mn, and Mn – O bond length, *e.g.*, due to oxygen vacancies (V<sub>O</sub>), can shift the binding of the reaction intermediates favorably.<sup>[248,265,269,270]</sup> Combined, these two factors result in an optimization of the reaction intermediate adsorption and improved charge transfer properties on the MnO<sub>x</sub> surface. As

mentioned during the characterization of the MnO<sub>2</sub>-NS in the STM images, the herein analyzed structures seemed to be relatively disordered and likely contained a large number of vacancies and distortions. Accordingly, it is not unexpected to find active sites across the surface. In comparison, the adjacent HOPG substrate remained largely inactive. It is unclear how much of this part was pure HOPG and how much was left of the CFePc coating in these areas. Still, the observations were in line with expectations, as the experiments in Chapter 7 showed that the HOPG basal plane should be inactive at the here applied potentials, and the CFePc film requires a combination of planar and edge sites for efficient oxygen evolution (for more details, please see Ref. [263] and Appendix D). All in all, the n-EC-STM data corroborated the literature views regarding the OER activity on MnO<sub>2</sub> complexes.

Most importantly, the n-EC-STM images indicated a probably even higher OER activity at the edges of the NS. This kind of morphological influence has so far received little attention in MnO<sub>x</sub> materials. Nevertheless, Maruyama *et al.* came to a similar conclusion in their analysis of the sample system.<sup>[263]</sup> Besides, facet-dependent activities of MnO<sub>x</sub> complexes have been reported by several groups.<sup>[252,256,260,271]</sup> From the here presented n-EC-STM measurements, it was not possible to exactly characterize the structure around the edge, even with high-resolution imaging. Therefore, the reasons for this enhancement at the edges cannot be directly revealed. However, with the previously introduced conditions for high OER activity on MnO<sub>x</sub> in mind, it can be assumed that the edges possess superior binding and charge transfer properties due to a modification of the local electronic structure. This is supported by the findings of Li *et al.*, who investigated some MnO<sub>2</sub> systems by DFT calculations.<sup>[270]</sup> Their results suggested a configuration beneficial for OER catalysis at edges which include lattice vacancies. From the disordered structure of the NS observed in the here presented images, it is reasonable to assume that such configurations were abundantly present in the model system. Based on these observations, it can be concluded that the edges of the MnO<sub>2</sub>-NS tend to offer the most suitable catalytic sites for the evolution of oxygen in alkaline media. To obtain further confirmation, DFT calculations are undertaken in collaboration with the research group of Prof. Egill Skúlason at the University of Iceland. Preliminary results indicate a favorable charge distribution at the edge sites, corroborating the experimental observations.

In summary, the electrocatalytic properties of MnO<sub>2</sub> sheets were characterized under OER conditions using the n-EC-STM technique. The measurements indicated active sites on the terraces of the thin nanosheets, as could be expected according to the discussed literature. What is more, the edges of the sheets exhibited even higher activities than the basal plane. It can be assumed that due to favorable structural configurations, such as the oxidation state of Mn and lattice vacancies, the interplay of intermediate adsorption and charge transfer speed is particularly beneficial for the OER at these centers. To create optimized MnO<sub>x</sub> based OER catalysts, it is therefore essential to consider the high activity of edge sites towards this reaction.

## Monitoring the Oxygen Evolution on Manganese Oxide Nanosheets

## 9 Outlook: Influence of the Electrolyte Species

The studies in this thesis demonstrate the importance of identification and understanding of the active sites on an electrode surface. However, the electrocatalytic efficiency is not only regulated by the structural properties of the electrode. An often overlooked component of the electrified solid/liquid interface is the so-called ‘spectator’ species in the electrolyte. It has been found that this can significantly impact catalyst performance.<sup>[73,272,273,274,275]</sup> In this outlook, current research regarding this electrolyte effect will be briefly outlined.

The outlook is based on the following publications:

*Haid, R. W.<sup>1</sup>; Ding, X.<sup>1</sup>; Sarpey, T. K.; Bandarenka, A. S. and Garlyyev, B. Exploration of the electrical double-layer structure: Influence of electrolyte components on the double-layer capacitance and potential of maximum entropy, Current Opinion in Electrochemistry 2022, 32, 100882.*<sup>[276]</sup>

*Ding, X.<sup>1</sup>; Scieszka, D. <sup>1</sup>; Watzele, S.; Xue, S.; Garlyyev, B.; Haid, R.W. and Bandarenka A.S. A systematic study of the influence of electrolyte ions on the electrode activity, ChemElectroChem 2022, 9, e202101088.*<sup>[277]</sup>

In principle, the ‘spectator’ species in the electrolyte, such as alkali metal cations, are not considered part of the reaction process. However, it has been observed that the nature of the electrolyte species does affect the electrocatalytic activity.<sup>[73,272,273,274,275]</sup> It has been proposed that this influence is mainly due to non-covalent interactions between solvated alkali metal cations and adsorbed species on the electrode surface.<sup>[278,279]</sup> This is schematically represented in Figure 9.1A, where non-covalent interactions between metal cations and adsorbed \*OH are depicted. These clusters at the electrode surface influence the availability of active sites, the movement of reactive species, and the strength of interfacial bonds. Consequently, a direct impact originating from the ‘spectator’ species on the electrocatalytic activity can be expected. For instance, Xue *et al.* demonstrated the effect of alkali metal cations on the HER of Pt electrodes in several alkaline electrolytes, as shown in Figure 9.1B.<sup>[280]</sup>

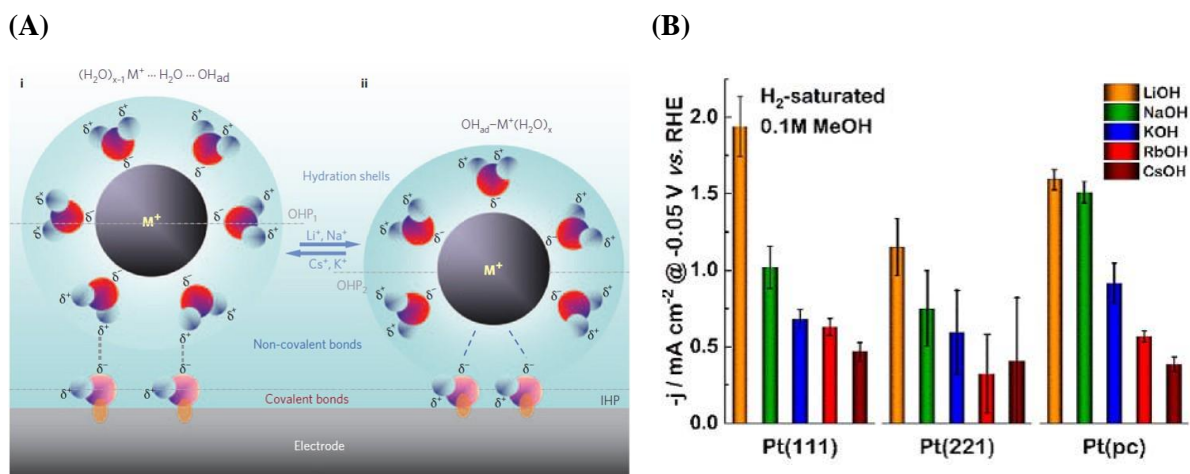


**Figure 9.1** (A) Schematic representation of the interactions at the electrified electrode/electrolyte interface. It has been suggested that non-covalent interactions between the ‘spectator’ species and surface-adsorbates influence electrocatalytic activity. Reprinted with permission from Ref. [278] Copyright © 2009, Springer Nature. (B) RDE measurements of the HER activities of Pt(111), Pt(221), and Pt(pc) in different alkaline electrolytes. The highest current densities at the applied potential of  $-0.05\ V$  vs RHE were recorded in LiOH. The activity decreased with decreasing hydration energy of the alkali metal cation in the solution. Reprinted with permission from Ref. [280] Copyright © 2018, John Wiley and Sons.

The order of the activities followed:  $LiOH > NaOH > KOH > RbOH > CsOH$ , which correlates with the hydration energy of the alkali metal cations in the solution. According to their report, the trends were practically independent of the surface structure. However, they reversed for materials on the weak binding site of the ‘volcano’ plot, such as Au and Ag. Recently, the effect of electrolyte species was systematically analyzed by Ding *et al.*, relying on a novel experimental approach, the laser-induced current transient technique (LICT).<sup>[277]</sup> In short, this technique utilizes a laser to momentarily heat up and disturb the electrode surface, disrupting the order of the electrolyte network at the interface. The ensuing rearrangement of the interfacial species results in a measurable current spike. With this technique, the potential of maximum entropy (PME) can be determined. At this potential, the current transient will disappear, as the species are already in a state of maximum disorder. Here, the electrolyte species possess the most freedom, which can be considered beneficial for reaction kinetics. With this in mind, the study, for example, showed the PME dependence on the nature of the alkali metal cations in the electrolyte for a polycrystalline (pc) Pt electrode (Figure 9.2A- D). In the plots, the y-axis represents the maximum value of the current transient, which crosses zero at the PME. As

## Outlook: Influence of the Electrolyte Species

Figure 9.2E illustrates, the PME correlated linearly with the hydration energies of the alkali metal cations.

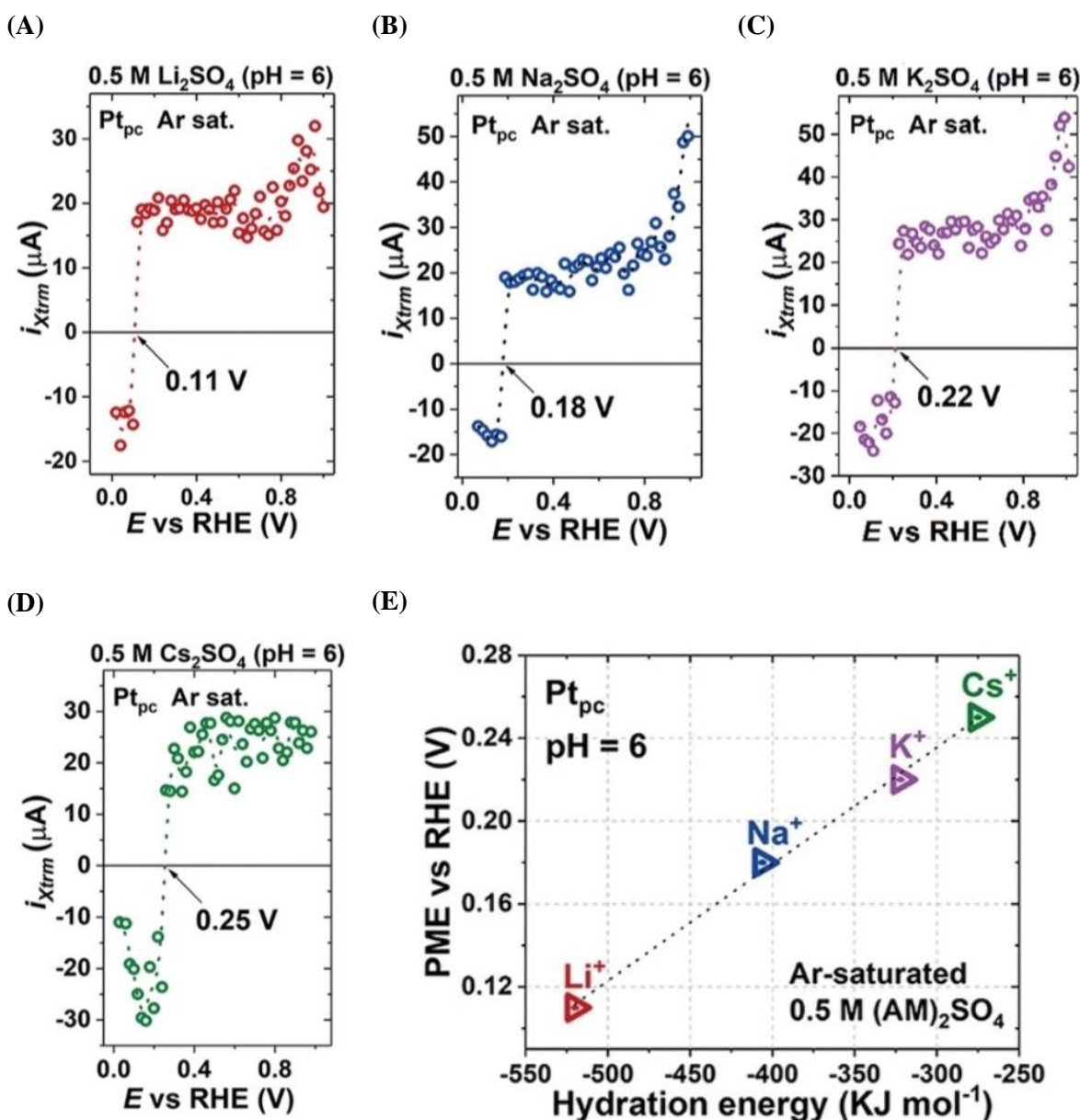


**Figure 9.2** (A-D) LICT data of Pt(pc) in 0.5 M (A)  $\text{Li}_2\text{SO}_4$ , (B)  $\text{Na}_2\text{SO}_4$ , (C)  $\text{K}_2\text{SO}_4$ , and (D)  $\text{Cs}_2\text{SO}_4$ , On the y-axis, the maximum of the current transient is given. At the potential where this value crosses zero, the PME is reached. As evident, the PME depended on the nature of the alkali metal cations in the electrolyte solution. (E) The PME was correlated to the hydration energy of the alkali metal cations, revealing a linear dependence. Reprinted with permission from Ref. [277] Copyright © 2022, John Wiley and Sons.

## Outlook: Influence of the Electrolyte Species

---

These studies demonstrate the importance of the ‘spectator’ species in the electrocatalytic processes. Therefore, to improve reaction kinetics, it is essential to consider not only electrode composition and structure but also the electrolyte components. The full extent of the electrolyte effects is far from understood, making it an exciting avenue for future research, especially using the n-EC-STM technique.

## 10 Summary and Conclusion

Improving the efficiency of electrocatalytic processes is essential to ensure a stable, sustainable energy supply in the future. To achieve this goal, the key component is a fundamental understanding of the dynamics at the electrified electrode/electrolyte interface. However, the implicated reaction mechanisms and the adsorbate-surface interactions are highly complex. Consequently, special experimental and theoretical approaches that can evaluate these intricate systems need to be developed. This thesis focuses on one particularly promising experimental technique in this regard, the n-EC-STM. This technique aims to identify the active electrocatalytic centers on the electrode surface. The advantage of the approach is that the structure of the catalyst surface can be probed *in-situ* and with a high spatial resolution. Essentially, it allows to create a map of the surface morphology and ‘see’ the active sites thereon. The reason for this is that noise spikes in the STM signal are caused locally by variations in the tunneling barrier due to the reaction processes. Consequently, the structural motifs responsible for the activity of an electrode can be directly revealed under reaction conditions. With this knowledge, well-founded design principles for highly efficient catalysts can be formulated.

This thesis explores novel methodological aspects of n-EC-STM and addresses several model systems that play a central role in energy conversion and storage, *e.g.*, in devices such as fuel cells, electrolyzers, and metal-air batteries.

- **Developing a framework for quantitative n-EC-STM studies:**

Since its inception, the main purpose of the n-EC-STM has been to determine the position of active sites on electrode surfaces qualitatively. However, on Pt(111) it was observed that at ORR potentials, step sites exhibit a higher noise level than adjacent terrace sites.<sup>[47]</sup> This echoes previous experimental and theoretical evidence, which suggested that although both types of sites are active, the steps should, in many cases, be superior.<sup>[36]</sup> This circumstance leads to the question: could the n-EC-STM provide quantitative information about the activity of specific surface sites? Based on this contemplation, a framework to perform quantitative analysis using n-EC-STM was developed in this thesis. For this purpose, a well-defined model system, Pt(111) in an acidic electrolyte (0.1 M HClO<sub>4</sub>), was investigated for the ORR. In the first step, the

noise level in dependence of the applied potential was investigated at the basal plane. For this, the relative change with time of the STM signal at several potentials was plotted as histograms. The data were fitted by a Gaussian curve, and the FWHM was introduced as a descriptor of the noise level. Simultaneously to the STM measurement, the sample current was recorded, which provides the TOF of the basal plane. This serves as the descriptor for the local activity. The experiments suggested a linear relationship between the two values, implying that the extent of the noise in the STM signal is directly related to the local rate of the reaction. However, due to influences from *e.g.* the tip shape and the electrolyte concentration, the relation cannot be generalized so far. Nonetheless, the method was subsequently extended to step sites on the Pt(111) crystal. Here, it is not possible to obtain the TOF directly. Therefore, the noise-activity relation of the basal plane was utilized to gauge the activity at steps. This was done by gathering data from the basal plane and step site within the same measurement. The former gives the noise level-activity relation of the specific measurement, and the TOF of the latter can thus be estimated from its noise level. Generally, the step sites exhibited a higher activity than the basal plane. To analyze this observation more deeply, the improvement factor of the steps in comparison to the basal plane was calculated. The obtained values are in good agreement with literature reports on the improvement that can be expected from certain high-index planes of Pt. This confirms the accuracy of the here developed method and warrants its application to even more complex systems in the future.

- **Visualizing active sites with atomic resolution:**

One of the major advantages of STM compared to other microscopy techniques is the outstanding resolution that can be reached. Already shortly after the first device was developed, its capability to obtain information on the atomic arrangement of surfaces was demonstrated.<sup>[157]</sup> Achieving this kind of resolution while performing n-EC-STM measurements would yield valuable knowledge about the atomic configurations that form the active sites. With this objective in mind, the HER was herein investigated on HOPG in an acidic electrolyte (0.1 M HClO<sub>4</sub>). First, it was established that the active sites are located near step edges, while the basal plane is mainly inactive. Subsequently, several step edges and defective sites were imaged with high resolution. After

processing the data by FFT, the active sites were clearly distinguished on the regular atomic lattice of the graphite surface as spots with a higher intensity of the STM signal. Their position was predominantly in the first two rows of atoms along the upper edge of steps, as well as in the vicinity of defective sites. The experimental insight was confirmed and substantiated by a dedicated DFT study, which calculated the binding energy of the reaction intermediate  $^*H$  at various types of sites on the HOPG lattice, such as terraces, steps, and vacancies. In accordance with the experimental data, the DFT results predicted the most active centers in the immediate vicinity to certain steps and defects. In combination, the approaches provide conclusive evidence for the position of the active sites and demonstrate the capability of the n-EC-STM technique to locate them with atomic resolution.

- **Evaluating a bifunctional carbon-based electrode:**

The operation of devices such as metal-air batteries and regenerative fuel cells relies on bifunctional catalysts. As these materials need to be able to promote two reactions, the active sites of both reactions need to be determined to create an efficient catalyst. In this thesis, the n-EC-STM technique was applied to analyze the active sites of such a system, in particular, the ORR and OER on HOPG in an alkaline environment (0.1 M KOH). For both reactions, the highest activity was found at step edges and defects. The basal plane was mostly inactive, only at higher overpotentials, some OER activity was observed. In this aspect, the experiments suggested that the surface quality was not influenced significantly. Notably, the catalytic behavior towards the ORR was unchanged after applying the OER potentials, indicating commensurate surface stability. Furthermore, by high-resolution imaging, the active sites for the ORR were analyzed more closely. From the images, it was deduced that the active centers are in close vicinity to the upper step edge. Noticeably, the potential at which the sites became active depended on the local atomic configuration. These conclusions were supported by predictions from theoretical calculations found in literature reports on related model systems. The results demonstrate the versatility of the n-EC-STM technique and shed further light on the important role of structural defects in electrocatalysis.

- **Exploring a manganese oxide nanostructure:**

In nature,  $\text{MnO}_x$  is the component of photosystem II responsible for water splitting. Consequently, it has become a focal point in the search for efficient, affordable ORR and OER electrocatalysts. However, many structural variations of  $\text{MnO}_x$  exist. It is still debated which configurations are most active and for which reasons. Herein, a  $\text{MnO}_2$  electrode in the form of nanosheets deposited on a HOPG surface (covered by a carbonaceous iron porphyrin film) was investigated for the OER in 0.1 M KOH. One of the major challenges of the experiments was to differentiate between the sheets and the substrate in the STM. For this reason, structural parameters such as monolayer height and inter-atom distances were evaluated. The subsequent n-EC-STM measurements revealed activity over the entire surface area of the  $\text{MnO}_2$ , while the carbon support showed no participation in the reaction. The edges of the sheets appeared to be particularly beneficial for OER catalysis. This was further demonstrated using high-resolution imaging. It can be imagined that the edges offer an abundance of favorable electronic configurations, resulting in a superior OER activity compared to the basal plane. All in all, the study demonstrates the abilities of n-EC-STM on a more complex model system and contributes to a deeper understanding of the reaction kinetics on  $\text{MnO}_x$  electrodes.

In conclusion, the herein collected results represent fundamental progress in two aspects. On the one hand, the capabilities of the n-EC-STM technique are further developed, paving the way for a more substantial analysis of electrode activity. On the other hand, the technique was applied to elucidate the active sites of several model systems, which are important for energy conversion, with a resolution close to the atomic one. Since the experiments were performed under reaction conditions, the gained insight can be turned into fundamental guidelines for catalyst structures and, for example, indicate how nanoparticles should be shaped to maximize the activity. As highlighted in the outlook, besides structural properties, it is essential to also keep other aspects of the electrocatalytic system in mind. Especially the influence of the seemingly ‘inert’ electrolyte species still presents many unexplored possibilities for future studies with n-EC-STM.

## Appendix A: Acknowledgements

I could not have realized this project without all the support I received throughout my four years at the ECS chair. First and foremost, I would like to thank **Prof. Dr. Aliaksandr Bandarenka** for accepting me first as a master student and afterward as a Ph.D. candidate. I thoroughly enjoyed the research topic, especially because of the combination of electrochemistry and physics. The project gave me the opportunity and freedom to pursue many interesting aspects of electrocatalysis.

I especially thank **Dr. Regina Kluge** for the wonderful teamwork on the experiments and publications. I was always able to rely on her and benefitted greatly from her ability to tackle problems head-on. I would like to extend my gratitude to **Dr. Yunchang Liang** for teaching me not only how to conduct EC-STM measurements but, more importantly, how to conduct serious research in general. My thanks also go to **Thorsten Schmidt** for his meticulous work on our projects and all the effort he put into the installation of the second STM device.

I thank my officemates **Dr. Batyr Garlyyev**, **Dr. Sebastian Watzele**, and **Dr. Elena Gubanova** for creating a productive yet fun work atmosphere, for always sharing their expertise when I had questions, and especially for the much-needed coffee breaks.

Thank you to **Xaver Lamprecht**, **Theophilus Sarpey**, **Leon Katzenmeier**, **Peter Schneider**, **Leif Carstensen**, **Kun-Ting Song**, **Rainer Götz**, **Göktug Yesilbas**, **Eleftherios Psaltis**, **Dr. Johannes Fichtner**, **Philipp Marzak**, **Dr. Jeongsik Jun** and **Dr. Daniel Scieszka** for always lending a helping hand when I needed it and for letting me be part of some of their projects.

A special thanks to all my Chinese colleagues, particularly **Dr. Xing Ding**, **Shujin Hou**, **Dr. Song Xue**, **Xiaoxin Ma**, and **Prof. Weijin Li**, not only for the cooperation on several topics but also for patiently helping me to learn Chinese.

Thank you to **Manuela Ritter** and **Siegfried Schreier** for taking care of the administrative and technical issues, especially during the installation of the new STM in the Glovebox.

Furthermore, I owe thanks to our collaboration partners, **Dr. Jun Maruyama**, **Dr. Federico Calle-Vallejo**, **Prof. Ifan Stephens**, **Prof. Egill Skúlason**, and **André Wark**, who provided samples, theoretical calculations, and valuable scientific expertise.

Last but not least, I thank **my family** for all the support throughout my studies.



**Appendix B: EC-STM Measurement Parameters**

Figure	STM Mode	Current Setpoint [nA]	Scan Rate [mHz]	Tip Potential [mV <sub>Pt</sub> ]
<b>5.4B, C.1A-I</b>	ch*	2.0	4.0	-50
<b>5.6A, C.3A-I</b>	cc**	1.5	1.5	0
<b>6.3A,B</b>	ch	6.0	30	-50
<b>6.4A</b>	ch	3.0	60	-225
<b>6.4B</b>	ch	3.0	30	-225
<b>6.5A</b>	ch	2.0	30	-600
<b>6.5B</b>	ch	4.0	60	-225
<b>6.6A</b>	ch	4.0	60	-225
<b>6.6B</b>	ch	6.0	60	-600
<b>7.1B</b>	cc	1.0	1.0	0
<b>7.2B</b>	cc	2.0	0.5	-50
<b>7.3A-F</b>	cc	2.0	0.5	-50
<b>7.4A</b>	ch	2.0	20	-50
<b>7.4B</b>	ch	0.5	20	-50
<b>7.4C,D</b>	ch	2.0	20	-50
<b>8.1B, 8.2-1, 8.2-2</b>	cc	2.0	1.0	0
<b>8.2-3</b>	cc	2.5	2.0	0
<b>8.2-4</b>	cc	4.0	2.0	0
<b>8.3A</b>	ch	6.0	60	0
<b>8.3B</b>	ch	6.0	60	300
<b>8.5A,B</b>	cc	2.0	2.5	-25

## Appendix B: EC–STM Measurement Parameters

<b>8.6A,B</b>	ch	15	60	-50 (Off) / 250 (On)
<b>8.6C,D</b>	ch	10	60	-50 (Off) / 250 (On)
<b>8.7</b>	ch	15	60	-150 (Off) / 300 (On)
<b>C.2</b>	ch	2.0	4.0	-50, -100, -150, -200
<b>D.1A,B</b>	cc	2.0	0.5	45
<b>D.2A,B</b>	cc	5.0	0.5	25

\*ch = constant height; \*\*cc = constant current

## Appendix C: Additional Data of the Quantitative n-EC-STM Method

In this appendix, additional measurements that supplement the results presented in Chapter 5 are collected. Figure C.1 shows the datasets relating the noise level and the TOF obtained from nine individual n-EC-STM measurements over the Pt(111) basal plane. In this data, each measurement includes several data points taken at potentials below  $-0.25 V_{Pt}$ . Here, the sample current reached a mass-limit plateau (*cf.* Figure 5.3A), and accordingly, the relation between noise and activity stagnated in this region.

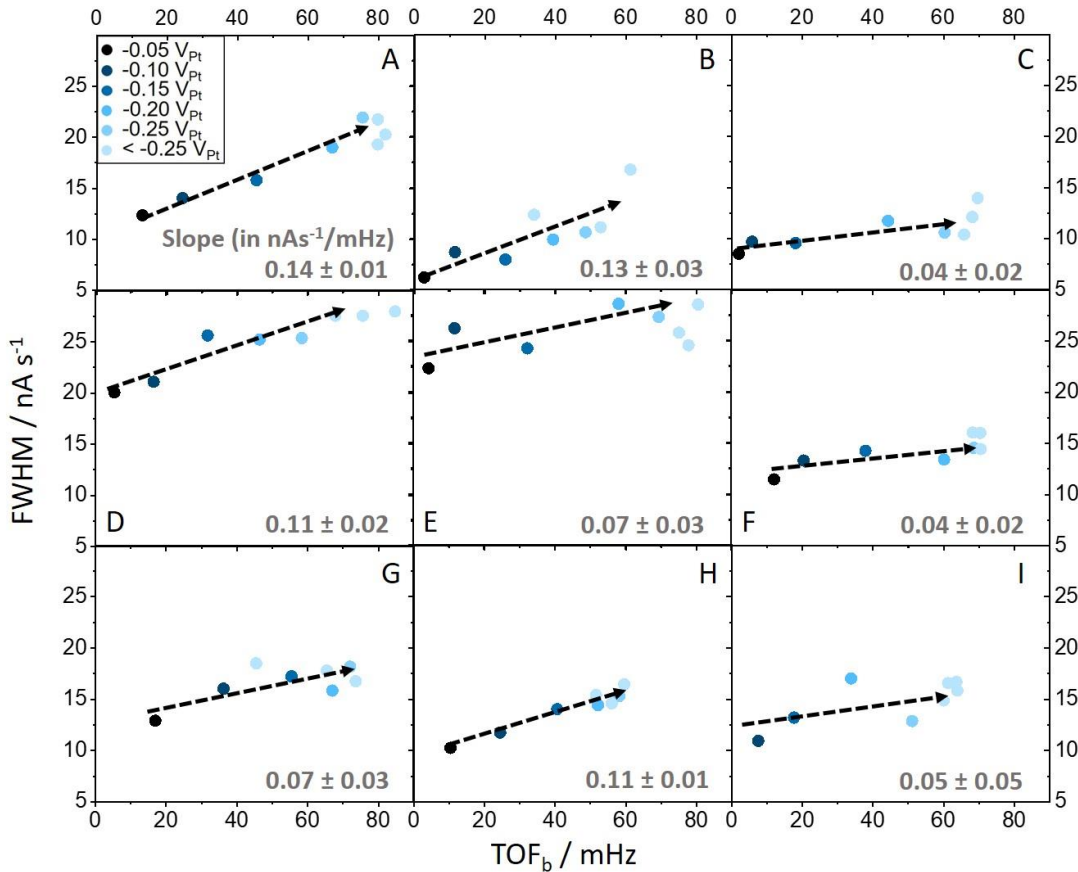


**Figure C.1** Noise level-activity relation of nine separate sets of n-EC-STM measurements over the Pt(111) basal plane. The noise level is represented by the FWHM, which was determined as described in Chapter 5.2. The local activity is reflected by the TOF at the basal plane ( $TOF_b$ ). In all cases, a linear trend can be observed between the two parameters, however, with varying slopes. Data published in Ref. [195].

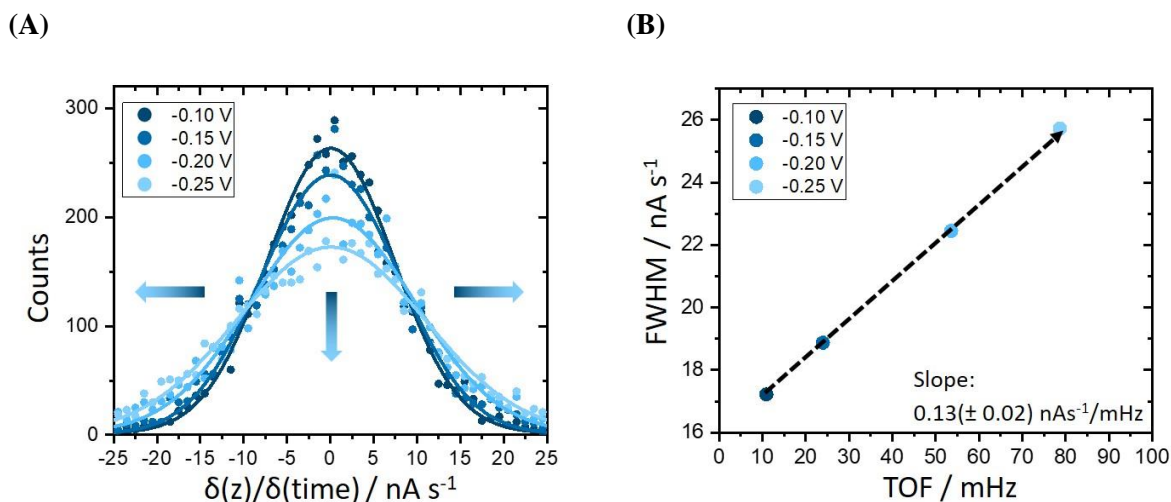


**Figure C.2** To confirm that the tip potential does not have a significant effect on the observed trends, a measurement with a constant potential bias between tip and sample was performed. In (A), the histograms and Gaussian fits of the measurements are given. In (B), the resulting noise level-activity relation is displayed. The trends were similar to the experiments where the tip potential was kept constant. Data published in Ref. [195].

Figure C.2 gives an example of a measurement performed with a constant potential bias throughout the experiment. In this case, the bias between tip and sample was kept at 0.05 V, *i.e.* the tip potential was decreased from -0.05 V<sub>Pt</sub> to -0.20 V<sub>Pt</sub> along with the decreasing sample potential. The measurement was done to confirm that the observed activity trends are not caused artificially by the changing bias between tip and sample potential during the measurements presented in Chapter 5.2. As one can see, the results were very similar to the ones with changing bias, so it can be assumed that the effect from the tip potential is negligible in this case.

Figure C.3 shows the noise-activity relations deduced from nine individual measurements of surface areas, including a step. Using the data of a (111) terrace next to the step, the linear relation was rendered. Extracting the noise level of the step site and extrapolating it on this relation reveals its local TOF. This data is the basis of the improvement factors  $\text{TOF}_s/\text{TOF}_b$  plotted in Figure 5.5B.

Appendix C: Additional Data of the Quantitative n-EC-STM Method

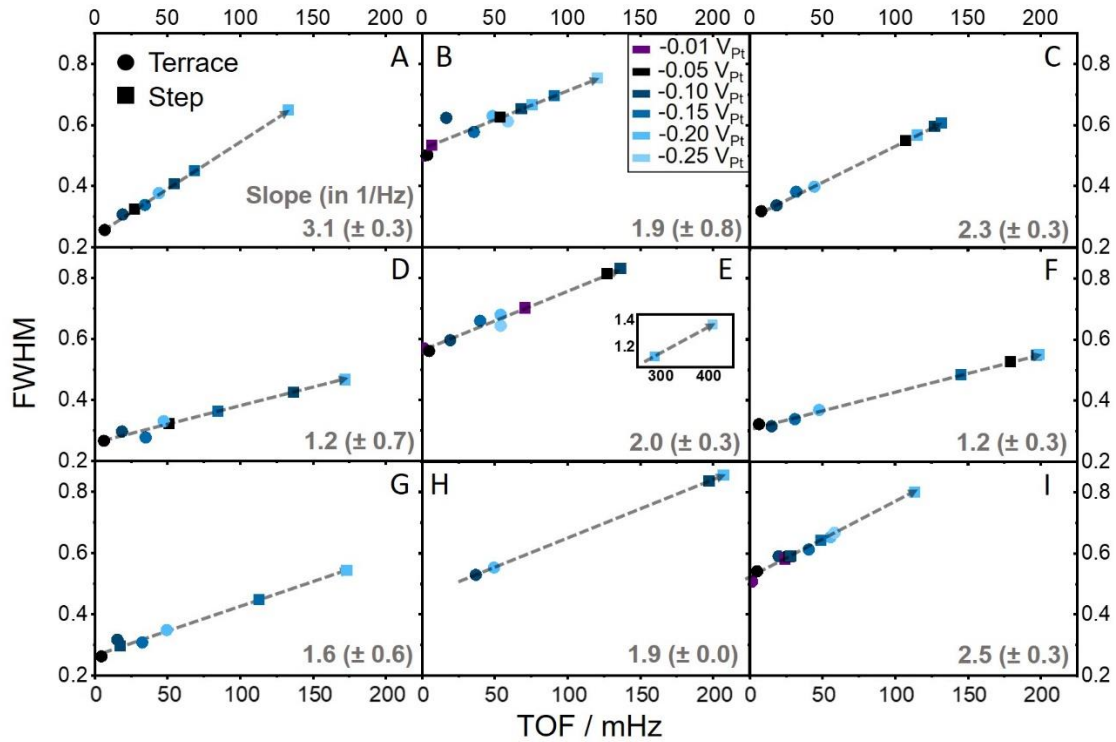


**Figure C.3** Noise level - activity relation of nine separate sets of n-EC-STM measurements. Data from a (111) terrace is recorded as a ‘calibration curve’ to extract the activity data of an adjacent step site. The local TOF<sub>s</sub> of the latter can be obtained using the FWHM of the Gaussian fit to their histograms, and the noise-activity correlation, as detailed in Chapter 5.3. Data published in Ref. [195].

Appendix C: Additional Data of the Quantitative n-EC-STM  
Method

**Table C.1** Averaged sample current (in  $\mu\text{A}$ ), recorded simultaneously to the n-EC-STM measurements. The errors represent the standard deviation.

Potential [V <sub>ps</sub> ]	0.01	0.05	0.10	0.15	0.20	0.25	0.30	0.35	0.40
<b>Figure 5.4B/ C.1A</b>	-	-1.5 ( $\pm 1.4$ )	-2.8 ( $\pm 1.4$ )	-5.3 ( $\pm 1.4$ )	-7.8 ( $\pm 1.7$ )	-8.8 ( $\pm 1.8$ )	-9.3 ( $\pm 1.8$ )	-9.5 ( $\pm 1.7$ )	-9.3 ( $\pm 1.6$ )
<b>C.1B</b>	-	-0.3 ( $\pm 0.3$ )	-1.3 ( $\pm 0.3$ )	-2.9 ( $\pm 0.3$ )	-4.4 ( $\pm 0.3$ )	-5.5 ( $\pm 0.3$ )	-6.0 ( $\pm 0.3$ )	-3.8 ( $\pm 0.8$ )	-6.9 ( $\pm 0.2$ )
<b>C.1C</b>	-	-0.2 ( $\pm 0.3$ )	-0.7 ( $\pm 0.2$ )	-2.1 ( $\pm 0.2$ )	-5.1 ( $\pm 0.4$ )	-7.0 ( $\pm 0.6$ )	-7.6 ( $\pm 0.4$ )	-7.9 ( $\pm 0.4$ )	-8.1 ( $\pm 0.3$ )
<b>C.1D</b>	-	-0.6 ( $\pm 0.3$ )	-1.9 ( $\pm 0.3$ )	-3.7 ( $\pm 0.3$ )	-5.4 ( $\pm 0.3$ )	-6.8 ( $\pm 0.3$ )	-7.9 ( $\pm 0.3$ )	-8.8 ( $\pm 0.3$ )	-9.8 ( $\pm 0.3$ )
<b>C.1E</b>	-	-0.5 ( $\pm 0.3$ )	-1.4 ( $\pm 0.3$ )	-3.7 ( $\pm 0.3$ )	-6.7 ( $\pm 0.5$ )	-8.1 ( $\pm 0.6$ )	-8.7 ( $\pm 0.5$ )	-9.0 ( $\pm 0.4$ )	-9.4 ( $\pm 0.4$ )
<b>C.1F</b>	-	-1.4 ( $\pm 1.2$ )	-2.4 ( $\pm 1.2$ )	-4.4 ( $\pm 1.2$ )	-7.0 ( $\pm 1.3$ )	-8.0 ( $\pm 1.6$ )	-8.2 ( $\pm 1.8$ )	-8.2 ( $\pm 1.5$ )	-7.9 ( $\pm 1.4$ )
<b>C.1G</b>	-	-2.0 ( $\pm 1.6$ )	-4.2 ( $\pm 1.6$ )	-6.4 ( $\pm 1.6$ )	-7.8 ( $\pm 1.8$ )	-8.4 ( $\pm 1.8$ )	-8.6 ( $\pm 1.7$ )	-7.6 ( $\pm 1.7$ )	-5.3 ( $\pm 1.4$ )
<b>C.1H</b>	-	-1.2 ( $\pm 0.3$ )	-2.8 ( $\pm 0.3$ )	-4.7 ( $\pm 0.3$ )	-6.1 ( $\pm 0.3$ )	-6.8 ( $\pm 0.3$ )	-6.9 ( $\pm 0.3$ )	-6.5 ( $\pm 0.3$ )	-6.0 ( $\pm 0.3$ )
<b>C.1I</b>	-	-0.9 ( $\pm 0.3$ )	-2.1 ( $\pm 0.3$ )	-3.9 ( $\pm 0.5$ )	-5.9 ( $\pm 0.6$ )	-7.0 ( $\pm 0.6$ )	-7.4 ( $\pm 0.5$ )	-7.4 ( $\pm 0.4$ )	-7.1 ( $\pm 0.5$ )
<b>C.2</b>	-	-	-1.3 ( $\pm 0.4$ )	-2.9 ( $\pm 1.1$ )	-6.5 ( $\pm 0.7$ )	-9.5 ( $\pm 1.2$ )	-	-	-
<b>Figure 5.6A/ C.3A</b>	-	-0.8 ( $\pm 0.2$ )	-2.3 ( $\pm 0.2$ )	-4.1 ( $\pm 0.2$ )	-5.3 ( $\pm 0.3$ )	-	-	-	-
<b>C.3B</b>	-0.1 ( $\pm 0.2$ )	-0.4 ( $\pm 0.2$ )	-2.0 ( $\pm 0.3$ )	-4.3 ( $\pm 0.3$ )	-5.9 ( $\pm 0.3$ )	-7.1 ( $\pm 0.4$ )	-	-	-
<b>C.3C</b>	-	-0.9 ( $\pm 0.1$ )	-2.2 ( $\pm 0.2$ )	-3.8 ( $\pm 0.2$ )	-5.3 ( $\pm 0.2$ )	-	-	-	-
<b>C.3D</b>	-	-0.8 ( $\pm 0.2$ )	-2.2 ( $\pm 0.2$ )	-4.2 ( $\pm 0.2$ )	-5.7 ( $\pm 0.3$ )	-	-	-	-
<b>C.3E</b>	-	-0.6 ( $\pm 0.3$ )	-2.3 ( $\pm 0.3$ )	-4.8 ( $\pm 0.3$ )	-6.5 ( $\pm 0.3$ )	-6.5 ( $\pm 0.9$ )	-	-	-
<b>C.3F</b>	-	-0.8 ( $\pm 0.2$ )	-1.8 ( $\pm 0.2$ )	-3.8 ( $\pm 0.3$ )	-5.8 ( $\pm 0.6$ )	-	-	-	-
<b>C.3G</b>	-	-0.5 ( $\pm 0.2$ )	-1.9 ( $\pm 0.2$ )	-3.9 ( $\pm 0.2$ )	-6.0 ( $\pm 0.3$ )	-	-	-	-
<b>C.3H</b>	-	-	-	-4.5 ( $\pm 0.6$ )	-	-6.0 ( $\pm 1.5$ )	-	-	-
<b>C.3I</b>	-0.2 ( $\pm 0.3$ )	-0.6 ( $\pm 0.3$ )	-2.4 ( $\pm 0.3$ )	-4.9 ( $\pm 0.3$ )	-6.7 ( $\pm 0.3$ )	-7.0 ( $\pm 1.0$ )	-	-	-

## Appendix C: Additional Data of the Quantitative n-EC-STM Method

---

**Table C.2** Data points in Figure 5.5B.

$j_{WE}$ [mA cm <sup>-2</sup> ]	TOF <sub>s</sub> /TOF <sub>t</sub>	Figure	Potential [V vs Pt]
-0.001	5.84	C.3B	-0.01
-0.002	17.06	C.3I	-0.01
-0.003	14.73	C.3B	-0.05
-0.005	26.61	C.3E	-0.05
-0.005	5.53	C.3I	-0.05
-0.006	8.17	C.3D	-0.05
-0.006	27.22	C.3F	-0.05
-0.006	4.07	C.3A	-0.05
-0.007	13.81	C.3C	-0.05
-0.014	12.94	C.3F	-0.10
-0.015	1.13	C.3G	-0.10
-0.016	4.11	C.3B	-0.15
-0.017	6.96	C.3C	-0.10
-0.017	7.36	C.3D	-0.10
-0.018	2.86	C.3A	-0.10
-0.018	7.06	C.3E	-0.10
-0.019	1.42	C.3I	-0.10
-0.030	4.64	C.3F	-0.15
-0.030	4.14	C.3C	-0.15
-0.031	3.47	C.3G	-0.15
-0.033	1.99	C.3A	-0.15
-0.033	2.43	C.3D	-0.15
-0.034	2.56	C.3B	-0.15
-0.036	5.34	C.3H	-0.15
-0.038	7.19	C.3E	-0.15
-0.039	1.21	C.3I	-0.20
-0.042	3.02	C.3A	-0.20
-0.042	2.60	C.3C	-0.20

Appendix C: Additional Data of the Quantitative n-EC-STM  
Method

---

-0.045	3.64	C.3D	-0.20
-0.046	4.16	C.3F	-0.20
-0.047	1.56	C.3B	-0.20
-0.048	3.50	C.3G	-0.20
-0.048	4.19	C.3H	-0.25
-0.052	7.55	C.3E	-0.20
-0.052	3.39	C.3E	-0.25
-0.053	2.05	C.3I	-0.20
-0.056	2.04	C.3B	-0.25

## Appendix D: n-EC-STM of the HOPG Modified by a Carbonaceous Iron Porphyrin Film

To complement the experiments on the HOPG-CFePc-MnO<sub>2</sub>-NS samples in Chapter 8, n-EC-STM measurements were also carried out on the substrate material. The samples were also produced and provided by the group of Dr. Jun Maruyama at the Osaka Research Institute of Industrial Science and Technology. Details on the fabrication process can be found in Ref. [263]. It should be noted that in this case, the HOPG surface was submitted to an etching treatment prior to the application of the CFePc film in order to create more exposed edge sites.

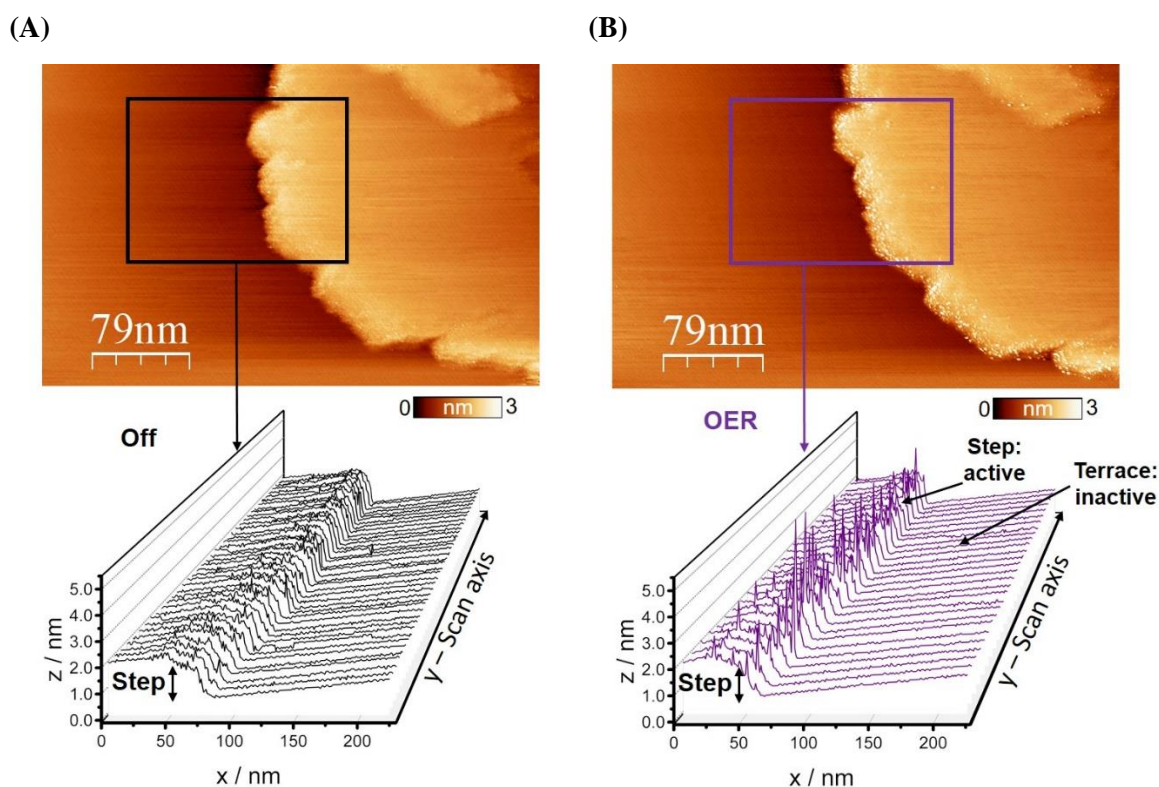


**Figure D.1** n-EC-STM measurements of the HOPG-CFePc substrate. (A) Reaction ‘Off’, showing a jagged edge site. In the waterfall plot below, several line scans are given. (B) OER ‘On’. Here, noise spikes along the edge reveal the position of the active sites. The terraces do not appear active at the applied potential (0.3 V<sub>Pt</sub>).

## Appendix D: n-EC-STM of the HOPG Modified by a Carbonaceous Iron Porphyrin Film

These are of particular interest, as according to the DFT calculations in Ref. [263], the optimal sites for oxygen evolution consist of a combination of edge and planar sites.

In Figures D.1A and B, respectively, n-EC-STM images of a step under OER conditions ( $0.3 V_{Pt}$ ) and while the reaction was ‘Off’ are given. Below the image, a section (as marked) of a step is shown as a waterfall plot. Under reaction conditions, noise spikes covered the region along the edge, which disappeared once the reaction was switched ‘Off’. Repetition of the experiment at other edge sites, as exemplarily shown in Figure D.2A and B, led to the same outcome. These observations are in line with the suggested position of the active sites in Ref. [263], *i.e.*, a combination of edge and planar sites as found at steps, whereas sites on the pure basal plane are less beneficial for the OER.

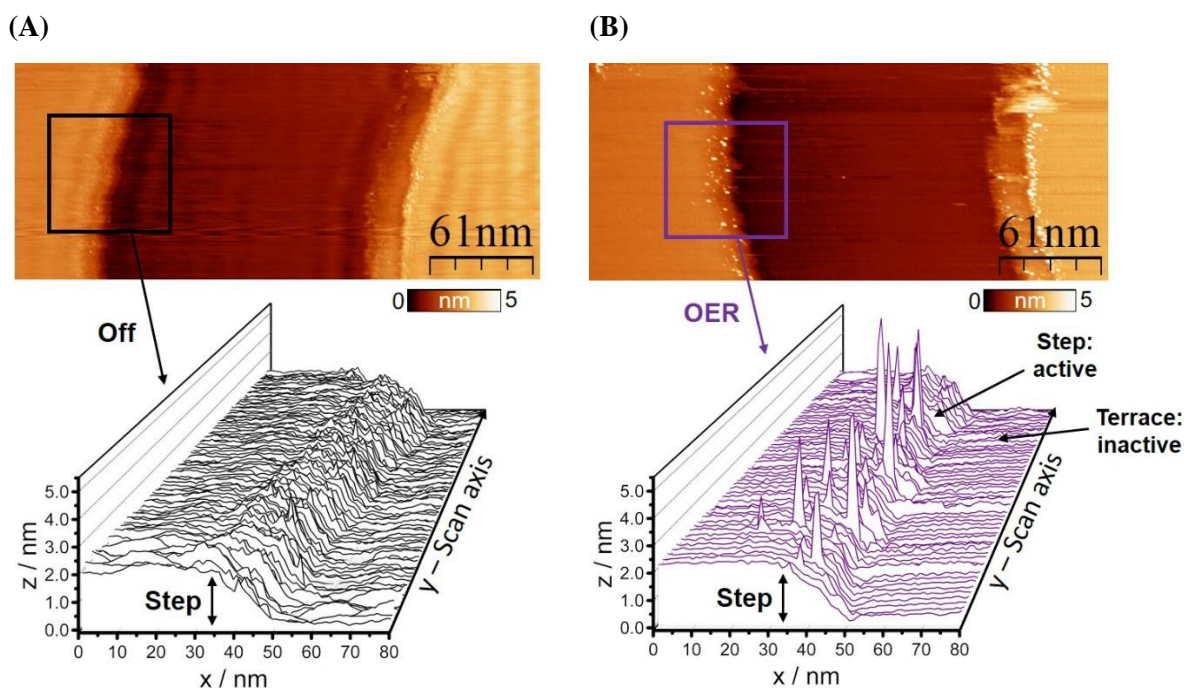


**Figure D.2** Further n-EC-STM investigation of the edge and basal plane on CFePc-HOPG. (A) Reaction ‘Off’. In this image, several steps are present; a particular focus was set on the area marked by the black square, which is also given as a waterfall plot below. (B) After the OER is turned ‘On’ ( $0.3 V_{Pt}$ ), various step sites become active. This is in line with the suggestion in Ref. [263] of improved reaction kinetics at a combination of edge sites and basal plane on this sample.

## Appendix E: Symbols and Abbreviations

---

<b>AFM</b>	atomic force microscopy
<b>Ar</b>	argon
<b>AuOx</b>	gold oxide
<b>CE</b>	counter electrode
<b>CFePc</b>	carbonaceous iron porphyrin
<b>CO</b>	carbon monoxide
<b>CU</b>	control unit
<b>CV</b>	cyclic voltammetry
<b>DFT</b>	density functional theory
<b>DTS</b>	distance tunneling spectroscopy
<b>EC-TERS</b>	electrochemical tip-enhanced Raman spectroscopy
<b>EDL</b>	electrical double layer
<b>EXAFS</b>	extended X-ray absorption fine structure
<b>FFT</b>	fast Fourier transformation
<b>FWHM</b>	full width at half maximum
<b>GGA</b>	generalized gradient approximation
<b>H</b>	hydrogen
<b>H<sub>2</sub></b>	hydrogen molecule
<b>H<sub>2</sub>O</b>	water molecule
<b>H<sub>2</sub>SO<sub>4</sub></b>	sulfuric acid

## Appendix E: Symbols and Abbreviations

---

<b>HClO<sub>4</sub></b>	perchloric acid
<b>HER</b>	hydrogen evolution reaction
<b>HOPG</b>	highly oriented pyrolytic graphite
<b>HOR</b>	hydrogen oxidation reaction
<b>IHP</b>	inner Helmholtz plane
<b>IrO<sub>2</sub></b>	iridium dioxide
<b>KOH</b>	potassium hydroxide
<b>LDOS</b>	local density of states
<b>LICT</b>	laser-induced current transient
<b>LSDA</b>	local spin density approximation
<b>LSV</b>	linear sweep voltammetry
<b>M, Me</b>	metal
<b>MnO<sub>x</sub></b>	manganese oxide
<b>MnO<sub>2</sub></b>	Manganese dioxide
<b>MMS</b>	mercury-mercurous sulfate
<b>MoS<sub>2</sub></b>	molybdenum disulphide
<b>n-EC-STM</b>	noise electrochemical scanning tunneling microscopy
<b>NS</b>	nanosheet
<b>O</b>	oxygen
<b>O<sub>2</sub></b>	oxygen molecule
<b>OER</b>	oxygen evolution reaction
<b>OHP</b>	outer Helmholtz plane

---

## Appendix E: Symbols and Abbreviations

---

---

<b>ORR</b>	oxygen reduction reaction
------------	---------------------------

---

<b>pc</b>	polycrystalline
-----------	-----------------

---

<b>PEM</b>	proton-exchange membrane
------------	--------------------------

---

<b>PME</b>	Potential of maximum entropy
------------	------------------------------

---

<b>Pt</b>	platinum
-----------	----------

---

<b>RDE</b>	rotating disk electrode
------------	-------------------------

---

<b>RE</b>	reference electrode
-----------	---------------------

---

<b>RHE</b>	reversible hydrogen electrode
------------	-------------------------------

---

<b>rpm</b>	revolutions per minute
------------	------------------------

---

<b>RuO<sub>2</sub></b>	ruthenium dioxide
------------------------	-------------------

---

<b>SECCM</b>	scanning electrochemical cell microscopy
--------------	--

---

<b>SEM</b>	scanning electron microscopy
------------	------------------------------

---

<b>STM</b>	scanning tunneling microscopy
------------	-------------------------------

---

<b>TOF</b>	turn-over frequency
------------	---------------------

---

<b>WE</b>	working electrode
-----------	-------------------

---

<b>XANES</b>	X-ray absorption near-edge structure
--------------	--------------------------------------

---

<b>XAS</b>	X-ray absorption spectroscopy
------------	-------------------------------

---

<b>V<sub>o</sub></b>	oxygen vacancy
----------------------	----------------

---



## References

- [1] Erisman, J. W., Sutton, M. A., Galloway, J., Klimont, Z. & Winiwarter, W. How a century of ammonia synthesis changed the world. *Nature Geosci.* **2008**, *1*, 636-639.
- [2] Pfromm, P. H. Towards sustainable agriculture: Fossil-free ammonia. *J. Renew. Sustain. Energy* **2017**, *9*, 034702.
- [3] Busacca, C. A., Fandrick, D. R., Song, J. J. & Senanayake, C. H. The growing impact of catalysis in the pharmaceutical industry. *Adv. Synth. Catal.* **2011**, *353*, 1825-1864.
- [4] Schäfer, B. Menthol. *Chem. Unserer Zeit.* **2013**, *47*, 174-182.
- [5] Zhang, X., Fevre, M., Jones, G. O. & Waymouth, R. M. Catalysis as an enabling science for sustainable polymers. *Chem. Rev.* **2018**, *118*, 839-885.
- [6] Zhang, H., Maijenburg, A. W., Li, X., Schweizer, S. L. & Wehrspohn, R. B. Bifunctional heterostructured transition metal phosphides for efficient electrochemical water splitting. *Adv. Funct. Mater.* **2020**, *30*, 2003261.
- [7] Staffell, I., Scamman, D., Abad, A. V., Balcombe, P., Dodds, E. P., Ekins, P. Shah, N. & Ward, K. R. The role of hydrogen and fuel cells in the global energy system. *Energy Environ. Sci.* **2019**, *12*, 463-491.
- [8] Cipriani, G., Di Dio, V., Genduso, F., La Cascia, D., Liga, R., Miceli, R. & Galluzzo, G. R. Perspective on hydrogen energy carrier and its automotive applications. *Int. J. Hydrog. Energy* **2014**, *39*, 8482-8494.
- [9] Scott, K. Introduction to electrolysis, electrolyzers and hydrogen production, in: Electrochemical Methods for Hydrogen Production Chapter 1. *The Royal Society of Chemistry* **2020**, pp. 1-27.
- [10] Zhang, L., Huang, Q.-A., Yan, W., Shao, Q. & Zhang, J. Design and fabrication of non-noble metal catalyst-based air-cathodes for metal-air battery. *Can. J. Chem. Eng.* **2019**, *97*, 2984-2993.
- [11] Lee, D. U., Cano, Z. P., Kashkooli, A. G., Park, M. G. & Chen, Z. Recent progress and perspectives on bi-functional oxygen electrocatalysts for advanced rechargeable metal-air batteries. *J. Mater. Chem. A* **2016**, *4*, 7107-7134.
- [12] Cheng, F. & Chen, J. Metal-air batteries: from oxygen reduction electrochemistry to cathode catalysts. *Chem. Soc. Rev.* **2012**, *41*, 2172-2192.

- 
- [13] Bockris, J. O'M. A hydrogen economy. *Science*. **1972**, *176*, 1323.
- [14] IEA Global Hydrogen Review 2021. <https://iea.blob.core.windows.net/assets/3a2ed84c-9ea0-458c-9421-d166a9510bc0/GlobalHydrogenReview2021.pdf> accessed on (05.11.2021).
- [15] European Commission. [https://ec.europa.eu/energy/sites/ener/files/hydrogen\\_strategy.pdf](https://ec.europa.eu/energy/sites/ener/files/hydrogen_strategy.pdf) accessed on (05.11.2021).
- [16] Müller, K. & Arlt, W. Status and development in hydrogen transport and storage for energy applications. *Energy Technol.* **2013**, *1*, 501-511.
- [17] Stetson, N. & Wieliczko, M. Hydrogen technologies for energy storage: A perspective. *MRS Energy Sustain.* **2020**, *7*, 41.
- [18] Miller, H. A., Bouzek, K., Hnat, J., Loos, S., Bernäcker, C. I., Weißgärber, T., Röntzsch, L. & Meier-Haack, J. M. Green hydrogen from anion exchange membrane water electrolysis: a review of recent developments in critical materials and operating conditions. *Sustain. Energy Fuels* **2020**, *4*, 2114-2133.
- [19] Wang, Y., Diaz, D. F. R., Chen, K. S., Wang, Z., & Adroher, X. C. Materials, technological status, and fundamentals of PEM fuel cells – A review. *Mater. Today* **2020**, *32*, 178-203.
- [20] Jacobsen, C. J. H., Dahl, S., Clausen, B. S., Bahn, S., Logadottir, A. & Nørskov, J. K. Catalyst design by interpolation in the periodic table: Bimetallic ammonia synthesis catalysts. *J. Am. Chem. Soc.* **2001**, *123*, 8404-8405.
- [21] Toyao, T., Maeno, Z., Takakusagi, S., Kamachi, T., Takigawa, I. & Shimizu, K. Machine learning for catalysis informatics: Recent applications and prospects. *ACS Catal.* **2020**, *10*, 2260-2297.
- [22] Dong, Y., Zhang, Y., Ran, M., Zhang, X., Liu, S., Yang, Y., Hu, W., Zheng, C. & Gao, X. Accelerated identification of high-performance catalysts for low-temperature NH<sub>3</sub>-SCR by machine learning. *J. Mater. Chem. A* **2021**, *9*, 23850-23859.
- [23] Döbereiner, J. W. Neu entdeckte merkwürdige eigenschaften des platinsuboxyds, des schwefel-platins und des metallischen platinstaubs. *Journal für Chemie und Physik* **1823**, *38*, 321-326.
- [24] Wisniak, J. The history of catalysis. From the beginning to nobel prizes. *Educ. Quim.* **2010**, *21*, 60-69.
- [25] Stacy, J., Regmi, Y. N., Leonard, B. & Fan, M. The recent progress and future of oxygen reduction reaction catalysis: A review. *Renew. Sust. Energ. Rev.* **2017**, *69*, 401-414.
- [26] Huang, L., Zaman, S., Tian, X., Wang, Z., Fang, W. & Xia, B. Y. Advanced platinum-based oxygen reduction electrocatalysts for fuel cells. *Acc. Chem. Res.* **2021**, *54*, 311-322.

## References

---

- [27] Zhao, R., Yue, X., Li, Q., Fu, G., Lee, J.-M. & Huang, S. Recent advances in electrocatalysts for alkaline hydrogen oxidation reaction. *Small* **2021**, 2100391.
- [28] Sabatier, P. Hydrogénations et déshydrogénations par catalyse. *Berichte der deutschen chemischen Gesellschaft*. **1911**, 44, 1984-2001.
- [29] Langmuir, I. Chemical reactions at low pressures. *J. Am. Chem. Soc.* **1915**, 37, 1139-1167.
- [30] Nørskov, J. K., Rossmeisl, J., Logadottir, A., Lindqvist, L., Kitchin, J. R., Bligaard, T. & Jónsson, H. Origin of the overpotential for oxygen reduction at a fuel-cell cathode. *J. Phys. Chem. B* **2004**, 108, 17886-17892.
- [31] Greeley, J. & Nørskov, J. K. Large-scale, density functional theory-based screening of alloys for hydrogen evolution. *Surf. Sci.* **2007**, 601, 1590-1598.
- [32] Tritsarlis, G. A. & Rossmeisl, J. Methanol oxidation on model elemental and bimetallic transition metal surfaces. *J. Phys. Chem. C* **2012**, 116, 11980-11986.
- [33] Reuter, K., Plaisance, C. P., Oberhofer, H. & Andersen, M. Perspective: On the active site model in computational catalyst screening. *J. Chem. Phys.* **2017**, 146, 040901.
- [34] Maheshwari, S., Li, Y., Agrawal, N. & Janik, M. J. Chapter three – Density functional theory models for electrocatalytic reactions. *Adv. Catal.* **2018**, 63, 117-167.
- [35] Bandarenka, A. S. & Koper, M. T. M. Structural and electronic effects in heterogeneous electrocatalysis: Toward a rational design of electrocatalysts. *J. Catal.* **2013**, 308, 11-24.
- [36] Bandarenka, A. S., Hansen, H. A., Rossmeisl, J. & Stephens, I. E. L. Elucidating the activity of stepped Pt single crystals for oxygen reduction. *Phys. Chem. Chem. Phys.* **2014**, 16, 13625-13629.
- [37] Kortlever, R., Shen, J., Schouten, K. J. P., Calle-Vallejo, F. & Koper, M. T. M. Catalysts and reaction pathways for the electrochemical reduction of carbon dioxide. *J. Phys. Chem. Lett.* **2015**, 6, 4073-4082.
- [38] Pohl, M. D., Watzele, S., Calle-Vallejo, F. & Bandarenka, A. S. Nature of highly active electrocatalytic sites for the hydrogen evolution reaction at Pt electrodes in acidic media. *ACS Omega* **2017**, 2, 8141-8147.
- [39] Del Colle, V., Perroni, P. B., Feliu, J. M., Tremiliosi-Filho, G. & Varela, H. The role of surface sites on the oscillatory oxidation of methanol on stepped Pt[n(111) × (110)] electrodes. *J. Phys. Chem. C* **2020**, 124, 10993-11004.
- [40] Taylor, H. S. A theory of the catalytic surface. *P. Roy. Soc. A-Math. Phys.* **1925**, 108, 105-111.

- [41] Garlyyev, B., Fichtner, J., Piqué, O., Schneider, O., Bandarenka, A. S. & Calle-Vallejo, F. Revealing the nature of active sites in electrocatalysis. *Chem. Sci.* **2019**, *10*, 8060-8075.
- [42] Li, F., Han, G.-F. & Baek, J.-B. Active site engineering in transition metal based electrocatalysts for green energy applications. *Acc. Mater. Res.* **2021**, *2*, 147-158.
- [43] Tang, Z., Zhao, S. & Yang, Y. Insight into structural evolution, active site and stability of heterogeneous electrocatalysts. *Angew. Chem. Int. Ed.* **2022**, *61*, e20211086.
- [44] Calle-Vallejo, F., Tymoczko, J., Colic, V., Vu, Q. H., Pohl, M. D., Morgenstern, K., Loffreda, D., Sautet, P., Schuhmann, W. & Bandarenka, A. S. Finding optimal surface sites on heterogeneous catalysts by counting nearest neighbors. *Science* **2015**, *350*, 185-189.
- [45] Garlyyev, B., Liang, Y., Xue, S., Watzele, S., Fichtner, J., Li, W.-J., Ding, X. & Bandarenka, A. S. Theoretical and experimental identification of active electrocatalytic surface sites. *Curr. Opin. Electrochem.* **2019**, *14*, 206-213.
- [46] Hou, S., Kluge, R. M., Haid, R. W., Gubanova, E. L., Watzele, S. A., Bandarenka, A. S. & Garlyyev, B. A review on experimental identification of active sites in model bifunctional electrocatalytic systems for oxygen reduction and evolution reactions. *ChemElectroChem.* **2021**, *8*, 3433-3456.
- [47] Pfisterer, J. H. K., Liang, Y., Schneider, O. & Bandarenka, A. S. Direct instrumental identification of catalytically active surface sites. *Nature* **2017**, *549*, 74-77.
- [48] Chen, C. J. Introduction to scanning tunneling microscopy. Third edition. *Oxford University Press*, **2021**.
- [49] Liang, Y., McLaughlin, D., Csoklich, C., Schneider, O. & Bandarenka, A. S. The nature of active centers catalyzing oxygen electro-reduction at platinum surfaces in alkaline media. *Energy Environ. Sci.* **2019**, *12*, 351-357.
- [50] Liang, Y., Csoklich, C., McLaughlin, D., Schneider, O. & Bandarenka, A. S. Revealing active sites for hydrogen evolution at Pt and Pd atomic layers on Au surfaces. *ACS Appl. Mater. Interfaces* **2019**, *11*, 12476-12480.
- [51] Mitterreiter, E., Liang, Y., Golibrzuch, M., McLaughlin, D., Csoklich, C., Bartl, J. D., Holleitner, A., Wurstbauer, U. & Bandarenka, A. S. In-situ visualization of hydrogen evolution sites on helium ion treated molybdenum dichalcogenides under reaction conditions. *npj 2D Mater. Appl.* **2019**, *3*, 1-9.
- [52] Kluge, R. M., Haid, R. W. & Bandarenka, A. S. Assessment of active areas for the oxygen evolution reaction on an amorphous iridium oxide surface. *J. Catal.* **2021**, *396*, 14-22.

## References

---

- [53] Kluge, R. M., Haid, R. W., Riss, A., Bao, Y., Seufert, K., Schmidt, T. O., Garlyyev, B., Barth, J. V., Allegretti, F., Auwärter, W., Calle-Vallejo, F. & Bandarenka, A. S. Analysis of the nature of active centres at the surface of Pt-alloy oxygen reduction electrocatalysts: Pt<sub>3</sub>Ni as an illustrative example. *In preparation*.
- [54] Kluge, R. M., Psaltis, E., Haid, R. W., Hou, S., Schmidt, T. O., Schneider, O., Garlyyev, B., Calle-Vallejo, F. & Bandarenka, A. S. Revealing the nature of active sites on Pt-Gd and Pt-Pr Alloys during the oxygen reduction reaction. *In preparation*.
- [55] Deutschmann, O., Knözinger, H., Kochloefl, K. & Turek, T. Heterogeneous catalysis and solid catalysis. In Ullmann's encyclopedia of industrial chemistry, (Ed.), 2009.
- [56] Ostwald, W. Über katalyse. *Nature*. **1902**, 65, 522-526.
- [57] Brett, C. M. A. & Brett, A. M. O. Electrochemistry: Principles, methods, and applications. *Oxford University Press*, **1993**.
- [58] Bard, A. J. & Faulkner, L. R. Electrochemical methods: Fundamentals and applications. *2<sup>nd</sup> ed. John Wiley & Sons Inc.*, **2001**.
- [59] Scholz, F. Electroanalytical methods: Guide to experiments and applications. *Springer Science & Business Media*, **2010**.
- [60] Helmholtz, H. Ueber einige gesetze der vertheilung elektrischer ströme in körperlichen leitern mit anwendung auf die thierisch-eletrischen versuche (schluss.). *Ann. Phys.* **1853**, 165, 211-233.
- [61] Gouy, M. Sur la constitution de la charge électrique à la surface d'un électrolyte. *J. Phys. Theor. Appl.* **1910**, 9, 457-468.
- [62] Chapman, D. L. LI. A contribution to the theory of electrocapillarity. *Phil. Mag.* **1913**, 25, 475-481.
- [63] Stern, O. Zur theorie der elektrolytischen doppelschicht. *Z. Elektrochem.* **1924**, 30, 508-516.
- [64] Shen, D., Liu, Y., Yang, G., Yu, H. & Peng, F. Mechanistic insights into cyclic voltammograms on Pt(111): Kinetics simulation. *ChemPhysChem* **2019**, 20, 2791-2798.
- [65] Elgrishi, N., Rountree, K. J., McCarthy, B. D., Rountree, E. S., Eisenhart, T. T. & Dempsey, J. L. A practical beginner's guide to cyclic voltammetry. *J. Chem. Educ.* **2018**, 95, 197-206.
- [66] Xing, W., Yin, G. & Zhang, J. Rotating electrode methods and oxygen reduction electrocatalysts. *Elsevier* **2014**.

- [67] Shinozaki, K., Zack, J. W., Richards, R. M., Pivovar, B. S. & Kocha, S. S. Oxygen reduction reaction measurements on platinum electrocatalysts utilizing rotating disk electrode technique: I. Impact of impurities, measurement protocols and applied corrections. *J. Electrochem. Soc.* **2015**, *162*, F1144.
- [68] Pedersen, C. M., Escudero-Escribano, M., Velázquez-Palenzuela, A., Christensen, L. H., Chorkendorff, I. & Stephens, I. E. L. Benchmarking Pt-based electrocatalysts for low temperature fuel cell reactions with the rotating disk electrode: oxygen reduction and hydrogen oxidation in the presence of CO (review article). *Electrochim. Acta.* **2015**, *179*, 647-657.
- [69] Kocha, S. S., Shinozaki, K., Zack, J. W., Myers, D. J., Kariuki, N., Nowicki, T., Stamenkovic, V. Kang, Y., Li, D. & Papageorgopoulos, D. Best practices and testing protocols for benchmarking ORR activities of fuel cell electrocatalysts using rotating disk electrode. *Electrocatalysis.* **2017**, *8*, 355-374.
- [70] Blizanac, B. B., Arenz, M., Ross, P. N & Marković, I. E. L. Surface electrochemistry of CO on reconstructed gold single crystal surfaces studied by infrared reflection absorption spectroscopy and rotating disk electrode. *J. Am. Chem. Soc.* **2004**, *126*, 10130-10141.
- [71] Zhu, Z., Liu, Q., Liu, X. & Shui, J. Temperature impacts on oxygen reduction reaction measured by the rotating disk electrode technique. *J. Phys. Chem. C* **2020**, *124*, 3069-3079.
- [72] Alia, S. M. & Anderson, G. C. Iridium oxygen evolution activity and durability baselines in rotating disk electrode half-cells. *J. Electrochem. Soc.* **2019**, *166*, F282.
- [73] Xue, S., Haid, R. W., Kluge, R., Ding, X., Garlyyev, B., Fichtner, J. Watzele, S., Hou, S. & Bandarenka, A. S. Enhancing the hydrogen evolution reaction activity of platinum electrodes in alkaline media using nickel-iron clusters. *Angew. Chem. Int. Ed.* **2020**, *59*, 10934-10938.
- [74] O'Hayre, R., Cha, S.-W., Colella, W. & Prinz, F.B. Fuel cell fundamentals. *Wiley* **2016**.
- [75] Basu, S. Recent trends in fuel cell science and technology. *Springer* **2007**.
- [76] Kuzume, A., Herrero, E. & Feliu, J. M. Oxygen reduction on stepped platinum surfaces in acidic media. *J. Electroanal. Chem.* **2007**, *599*, 333-343.
- [77] Hermann, K. & Rammer, F. Surface explorer. <http://surfexp.fhi-berlin.mpg.de>. **2010**, accessed on (26.01.2022).
- [78] Seh, Z. W., Kibsgaard, J., Dickens, C. F., Chorkendorff, I., Nørskov, J. K. & Jaramillo, T. F. Combining theory and experiment in electrocatalysis: Insights into materials design. *Angew. Science* **2017**, *355*, 6321.
- [79] Hohenberg, P. & Kohn, W. Inhomogeneous electron gas. *Phys. Rev.* **1964**, *136*, 864-871.

## References

---

- [80] Sham, L. J. & Kohn, W. One-particle properties of an inhomogeneous interacting electron gas. *Phys. Rev.* **1966**, *145*, 561-567.
- [81] Perdew, J. P. Density-functional approximation for the correlation energy of the inhomogeneous electron gas. *Phys. Rev. B* **1986**, *33*, 8822-8824.
- [82] Becke, A. D. Density-functional exchange-energy approximation with correct asymptotic behavior. *Phys. Rev. A* **1988**, *38*, 3098-3100.
- [83] Chengteh, L., Yang, W. & Parr, R. G. Development of the Colle-Salvetti correlation-energy formula into a functional of the electron density. *Phys. Rev. B* **1988**, *37*, 785-789.
- [84] Perdew, J. P., Burke, K. & Ernzerhof, M. Generalized gradient approximation made simple. *Phys. Rev. Lett.* **1996**, *77*, 3865-3868.
- [85] Adamo, C. & Barone, V. Toward reliable density functional methods without adjustable parameters: The PBE0 model. *J. Chem. Phys.* **1999**, *110*, 6158-6169.
- [86] Boese, A. D. & Martin, J. M. L. Development of density functionals for thermochemical kinetics. *J. Chem. Phys.* **2004**, *121*, 3405-3416.
- [87] Zhao, Y. & Truhlar, D. G. Design of density functionals that are broadly accurate for thermochemistry, thermochemical kinetics, and nonbonded interactions. *J. Phys. Chem. A* **2005**, *109*, 5656-5667.
- [88] Zhao, Y., Schultz, N. E. & Truhlar, D. G. Design of density functionals by combining the method of constraint satisfaction with parametrization for thermochemistry, thermochemical kinetics, and noncovalent interactions. *J. Chem. Theory Comput.* **2006**, *2*, 364-382.
- [89] Kabir, S., Artyushkova, K., Serov, A., Kiefer, B. & Atanassov, P. Binding energy shifts for nitrogen-containing graphene-based electrocatalysts – experiments and DFT calculations. *Surf. Interface Anal.* **2016**, *48*, 290-297.
- [90] Stephens, I. E. L., Bondarenko, A. S., Grønbjerg, U., Rossmeisl, J. & Chorkendorff, I. Understanding the electrocatalysis of oxygen reduction on platinum and its alloys. *Energy Environ. Sci.* **2012**, *5*, 6744-6762.
- [91] Chen, Z. W., Chen, L. X., Wen, Z. & Jiang, Q. Understanding electro-catalysis by using density functional theory. *Phys. Chem. Chem. Phys.* **2019**, *21*, 23782-23802.
- [92] Liao, X., Lu, R., Xia, L., Liu, Q., Wang, H., Zhao, K., Wang, Z. & Zhao, Y. Density functional theory for electrocatalysis. *Energy Environ. Mater.* **2022**, *5*, 157-185.
- [93] Greeley, J. & Mavrikakis, M. Alloy catalysts designed from first principles. *Nat. Mater.* **2004**, *3*, 810-815.

- [94] Skúlason, E., Tripkovic, V., Björketun, M. E., Gudmundsdóttir, S., Karlberg, G., Rossmeisl, J., Bligaard, T., Jónsson & Nørskov, J. K. Modeling the electrochemical hydrogen oxidation and evolution reactions on the basis of density functional theory calculations. *J. Phys. Chem. C* **2010**, *114*, 18182-18197.
- [95] Le, J.-B., Chen, A., Li, L., Xiong, J.-F., Lan, J., Liu, Y.-P., Iannuzzi, M. & Cheng, J. Modeling electrified Pt(111)-H<sub>ad</sub>/water interfaces from ab initio molecular dynamics. *Energy JACS Au* **2021**, *1*, 569-577.
- [96] Zagalskaya, A. & Alexandrov, V. Role of defects in the interplay between adsorbate evolving and lattice oxygen mechanisms of the oxygen evolution reaction in RuO<sub>2</sub> and IrO<sub>2</sub>. *ACS Catal.* **2020**, *10*, 3650-3657.
- [97] Klyukin, K., Zagalskaya, A. & Alexandrov, V. Ab initio thermodynamics of iridium surface oxidation and oxygen evolution reaction. *J. Phys. Chem. C* **2018**, *122*, 29350-29358.
- [98] Greeley, J., Jaramillo, T. F., Bonde, J., Chorkendorff, I. & Nørskov, J. K. Computational high-throughput screening of electrocatalytic materials for hydrogen evolution. *Nat. Mater.* **2006**, *5*, 909-913.
- [99] Pedersen, J. K., Batchelor, T. A. A., Bagger, A. & Rossmeisl, J. High-entropy alloys as catalysts for the CO<sub>2</sub> and CO reduction reactions. *Energy Environ. Sci.* **2020**, *10*, 2169-2176.
- [100] Mao, X., Wang, L., Xu, Y., Wang, P., Li, Y. & Zhao, J. Computational high-throughput screening of alloy nanoclusters for electrocatalytic hydrogen evolution. *npj Comput. Mater.* **2021**, *7*, 1-9.
- [101] Skúlason, E. & Jónsson, H. Atomic scale simulations of heterogeneous electrocatalysis: recent advances. *Adv. Phys.-X* **2017**, *2*, 481-495.
- [102] Liang, Y., Pfisterer, J. H. K., McLaughlin, D., Csoklich, C., Seidl, L., Bandarenka, A. S. & Schneider, O. Electrochemical scanning probe microscopies in electrocatalysis. *Small Methods* **2019**, *3*, 1800387.
- [103] Foster, A. J. & Lobo, R. F. Identifying reaction intermediates and catalytic active sites through in situ characterization techniques. *Chem. Soc. Rev.* **2010**, *39*, 4783-4793.
- [104] Timoshenko, J. & Cuenya, B. R. In situ/operando electrocatalyst characterization by X-ray absorption spectroscopy. *Chem. Rev.* **2021**, *121*, 882-961.
- [105] Fei, H., Dong, J., Chen, D., Hu, T., Duan, X., Shakir, I., Huang, Y. & Duan, X. Single atom electrocatalysts supported on graphene or graphene-like carbons. *Chem. Soc. Rev.* **2019**, *48*, 5207-5241.

## References

---

- [106] Yang, H. B., Miao, J., Hung, S.-F., Chen, J., Tao, H. B., Wang, X., Zhang, L., Chen, R., Chen, H. M., Dai, L. & Liu, B. Identification of catalytic sites for oxygen reduction and oxygen evolution in N-doped graphene materials: Development of highly efficient metal-free bifunctional electrocatalyst. *Sci. Adv.* **2010**, 2, e1501122.
- [107] Yang, Y., Wang, Y., Xiong, Y., Huang, X., Shen, L., Huang, R., Wang, H., Pastore, J. P., Yu, S.-H., Xiao, L., Brock, J. D., Zhuang, L. & Abruña, H. D. *In situ* X-ray absorption spectroscopy of a synergistic Co–Mn oxide catalyst for the oxygen reduction reaction. *J. Am. Chem. Soc.* **2019**, 141, 1463-1466.
- [108] Mukerjee, S., Srinivasan, S., Soriaga, M. P. & McBreen, J. Role of structural and electronic properties of Pt and Pt alloys on electrocatalysis of oxygen reduction: An in situ XANES and EXAFS investigation. *J. Electrochem. Soc.* **1995**, 142, 1409-1422.
- [109] Ebejara, N., Schnippering, M., Colburn, A. W., Edwards, M. A. & Unwin, P. R. Localized high resolution electrochemistry and multifunctional imaging: Scanning electrochemical cell microscopy. *Anal. Chem.* **2010**, 82, 9141-9145.
- [110] Snowden, M. E., Güell, A. G., Lai, S. C. S., McKelvey, K., Ebejer, N. O'Connell, M. A., Colburn, A. W. & Unwin, P. R. Scanning electrochemical cell microscopy: Theory and experiment for quantitative high resolution spatially-resolved voltammetry and simultaneous ion-conductance measurements. *Anal. Chem.* **2012**, 84, 2483-2491.
- [111] Ebejer, N., Güell, A. G., Lai, C. S. S., McKelvey, K., Snowden, M. E. & Unwin, P. R. Scanning Electrochemical Cell Microscopy: A versatile technique for nanoscale electrochemistry and functional imaging. *Annu. Rev. Anal. Chem.* **2013**, 6, 329-351.
- [112] Unwin, P. R., Güell, A. G. & Zhang, G. Nanoscale electrochemistry of sp<sup>2</sup> carbon materials: From graphite and graphene to carbon nanotubes. *Acc. Chem. Res.* **2016**, 49, 2041-2048.
- [113] Daviddi, E., Gonos, K. L., Colburn, A. W., Bentley, C. L. & Unwin, P. R. Scanning electrochemical cell microscopy (SECCM) chronopotentiometry: development and applications in electroanalysis and electrocatalysis. *Anal. Chem.* **2019**, 91, 9229-9237.
- [114] Tarnev, T., Aiyappa, H. B., Botz, A., Erichsen, T., Ernst, A., Andronescu, C. & Schuhmann, W., J. Scanning electrochemical cell microscopy investigation of single ZIF-derived nanocomposite particles as electrocatalysts for oxygen evolution in alkaline media. *Angew. Chem. Int. Ed.* **2019**, 58 14265-14269.
- [115] Pfisterer, J. H. K. & Domke, K. F. Unfolding the versatile potential of EC-TERS for electrocatalysis. *Curr. Opin. Electrochem.* **2018**, 8, 96-102.

- [116] Pfisterer, J. H. K., Baghernejad, M., Giuzio, G. & Domke, K. F. Reactivity mapping of nanoscale defect chemistry under electrochemical reaction conditions. *Nat. Commun.* **2019**, *10*, 1-10.
- [117] Kurouski, D., Mattei, M. & Van Duyne, R. P. Probing redox reactions at the nanoscale with electrochemical tip-enhanced raman spectroscopy. *Nano Lett.* **2015**, *15*, 7956-7962.
- [118] Sabanés, N. M., Ohto, T., Andrienko, D., Nagata, Y. & Domke, K. F. Electrochemical TERS elucidates potential-induced molecular reorientation of adenine/Au(111). *Angew. Chem. Int. Ed.* **2017**, *56*, 9796-9801.
- [119] Touzalin, T., Joiret, S., Maisonhaute, E. & Lucas, I. T. Capturing electrochemical transformations by tip-enhanced Raman spectroscopy. *Curr. Opin. Electrochem.* **2017**, *6*, 46-52.
- [120] Mattei, M., Kang, G., Goubert, G., Chulhai, D. V., Schatz, G. C., Jensen, L. & Van Duyne, R. P. Tip-enhanced Raman voltammetry: coverage dependence and quantitative modeling. *Nano Lett.* **2017**, *17*, 590-596.
- [121] Zeng, Z.-C., Huang, S.-C., Wu, D.-Y., Meng, L.-Y., Li, M.-H., Huang, T.-X., Zhong, J.-H., Wang, X., Yang, Z.-L. & Ren, B. Electrochemical tip-enhanced Raman spectroscopy. *J. Am. Chem. Soc.* **2015**, *137*, 11928-11931.
- [122] Stadler, J., Schmid, T. & Zenobi, R. Developments in and practical guidelines for tip-enhanced Raman spectroscopy. *Nanoscale* **2012**, *4*, 1856-1870.
- [123] Domke, K. F. & Pettinger, B. Studying surface chemistry beyond the diffraction limit: 10 years of TERS. *ChemPhysChem* **2010**, *11*, 1365-1373.
- [124] Verma, P. Tip-enhanced raman spectroscopy: Technique and recent advances. *Nano Lett.* **2017**, *17*, 6447-6466.
- [125] Alaswad, A., Baroutaji, A., Achour, H., Carton, J., Al Makky, A. & Olabi, A. G. Developments in fuel cell technologies in the transport sector. *Int. J. Hydrog. Energy* **2016**, *41*, 16499-16508.
- [126] Shiva Kumar, S. & Himabindu, V. Hydrogen production by PEM water electrolysis – A review. *Mater. Sci. Energy Technol.* **2019**, *2*, 442-454.
- [127] Kühn, S. & Strasser, P. Oxygen electrocatalysis on dealloyed Pt nanocatalysts. *Top. Catal.* **2016**, *59*, 1628-1637.
- [128] Lee, J.-S., Kim, S. T., Cao, R., Choi, N.-S., Liu, M., Lee, K. T. & Cho, J. Metal–air batteries with high energy density: Li–air versus Zn–air. *Adv. Energy Mater.* **2011**, *1*, 34-50.
- [129] Zhang, X.-B. Metal-Air Batteries: Fundamentals and applications. *Wiley-VCH* **2018**.

- [130] Wang, C., Yu, Y., Niu, J., Liu, Y., Bridges, D., Liu, X., Pooran, J., Zhang, Y. & Hu, A. Recent progress of metal–air batteries—A mini review. *Appl. Sci.* **2019**, *9*, 2787.
- [131] Zeng, M. & Li, Y. Recent advances in heterogeneous electrocatalysts for the hydrogen evolution reaction. *J. Mater. Chem. A* **2015**, *3*, 14942-14962.
- [132] Zeradjanin, A. R., Polymeros, G., Toparli, C., Ledendecker, M., Hodnik, N., Erbe, A., Rohwerder, M. & La Mantia, F. What is the trigger for the hydrogen evolution reaction? – towards electrocatalysis beyond the Sabatier principle. *Phys. Chem. Chem. Phys.* **2020**, *22*, 8768-8780.
- [133] Zeradjanin, A. R., Grote, J.-P., Polymeros, G. & Mayrhofer, K. J. J. A critical review on hydrogen evolution electrocatalysis: Re-exploring the volcano-relationship. *Electroanalysis* **2016**, *28*, 2256-2269.
- [134] Trasatti, S. Work function, electronegativity, and electrochemical behaviour of metals: III. Electrolytic hydrogen evolution in acid solutions. *J. Electroanal. Chem. Interf. Electrochem.* **1972**, *39*, 163-184.
- [135] Zhou, W., Jia, J., Jia, L., Yang, L., Hou, D., Li, G. & Chen, S. Recent developments of carbon-based electrocatalysts for hydrogen evolution reaction. *Nano Energy* **2016**, *28*, 29-43.
- [136] Zheng, Y., Jiao, Y., Li, L. H., Xing, T., Chen, Y., Jaroniec, M. & Qiao, S. Z. Toward design of synergistically active carbon-based catalysts for electrocatalytic hydrogen evolution. *ACS Nano* **2014**, *8*, 5290-5296.
- [137] Ge, X., Sumboja, A., Wu, D., An, T., Li, B., Goh, F. W. T., Hor, T. S. A., Zong, Y. & Liu, Z. Oxygen reduction in alkaline media: From mechanisms to recent advances of catalysts. *ACS Catal.* **2015**, *5*, 4643-4667.
- [138] Ma, J., Gong, L., Shen, Y., Sun, D., Liu, B., Zhang, J., Liu, D., Zhang, L. & Xia, Z. Detrimental effects and prevention of acidic electrolytes on oxygen reduction reaction Catalytic performance of heteroatom-doped graphene catalysts. *Front. Mater.* **2019**, *6*, 294.
- [139] Sui, S., Wang, X., Zhou, X., Su, Y., Riffat, S., & Liu, C.-j. A comprehensive review of Pt electrocatalysts for the oxygen reduction reaction: Nanostructure, activity, mechanism and carbon support in PEM fuel cells. *J. Mater. Chem. A* **2017**, *5*, 1808-1825.
- [140] Yin, X., & Zelenay, P. (Invited) Kinetic models for the degradation mechanisms of PGM-free ORR catalysts. *ECS Trans.* **2018**, *85*, 1239-1250.
- [141] Goellner, V., Armel, V., Zitolo, A., Fonda, E., & Jaouen, F. Degradation by hydrogen peroxide of metal-nitrogen-carbon catalysts for oxygen reduction. *J. Electrochem. Soc.* **2015**, *162*, H403-H414.

- [142] Li, Y., Li, Q., Wang, H., Zhang, L., Wilkinson, D. P. & Zhang, J. Recent progresses in oxygen reduction reaction electrocatalysts for electrochemical energy applications. *Electrochem. Energ. Rev.* **2019**, *2*, 518-538.
- [143] Shao, M., Chang, Q., Dodelet, J.-P. & Chenitz, R. Recent advances in electrocatalysts for oxygen reduction reaction. *Chem. Rev.* **2016**, *116*, 3594-3657.
- [144] Jin, H., Guo, C., Liu, X., Liu, J., Vasileff, A., Jiao, Y., Zheng, Y. & Qiao, S.-Z. Emerging two-dimensional nanomaterials for electrocatalysis. *Chem. Rev.* **2018**, *118*, 6337-6408.
- [145] Ramaswamy, N. & Mukerjee, S. Fundamental mechanistic understanding of electrocatalysis of oxygen reduction on Pt and non-Pt surfaces: acid versus alkaline media. *Adv. Phys. Chem.* **2012**, *2012*, 491604.
- [146] Plevová, M., Hnát, J. & Bouzek, K. Electrocatalysts for the oxygen evolution reaction in alkaline and neutral media. A comparative review. *J. Power Sources* **2021**, *507*, 230072.
- [147] Man, I. C., Su, H.-Y., Calle-Vallejo, F., Hansen, H. A., Martínez, J. I., Nilay, G. I., Kitchin, J., Jaramillo, T. F., Nørskov, J. K. & Rossmeisl, J. Universality in oxygen evolution electrocatalysis on oxide surfaces. *ChemCatChem* **2011**, *3*, 1159-1165.
- [148] Klyukin, K., Zagalskaya, A. & Alexandrov, V. Role of dissolution intermediates in promoting oxygen evolution reaction at RuO<sub>2</sub>(110) surface. *J. Phys. Chem. C* **2019**, *123*, 22151-22157.
- [149] Zagalskaya, A. & Alexandrov, V. Mechanistic study of IrO<sub>2</sub> dissolution during the electrocatalytic oxygen evolution reaction. *J. Phys. Chem. Lett.* **2020**, *11*, 2695-2700.
- [150] Rincón, R. A., Ventosa, E., Tietz, F., Masa, J., Seisel, S., Kuznetsov, V. & Schuhmann, W. Evaluation of perovskites as electrocatalysts for the oxygen evolution reaction. *ChemPhysChem* **2014**, *15*, 2810-2816.
- [151] Tian, G.-L., Zhao, M.-Q., Yu, D., Kong, X.-Y., Huang, J.-Q., Zhang, Q. & Wei, F. Nitrogen-doped graphene/carbon nanotube hybrids: In situ formation on bifunctional catalysts and their superior electrocatalytic activity for oxygen evolution/reduction reaction. *Small* **2014**, *10*, 2251-2259.
- [152] Chen, S., Duan, J., Jaroniec, M. & Qiao, S.-Z. Nitrogen and oxygen dual-doped carbon hydrogel film as a substrate-free electrode for highly efficient oxygen evolution reaction. *Adv. Mater.* **2014**, *26*, 2925-2930.
- [153] Duan, J., Chen, S., Jaroniec, M. & Qiao, S. Z. Heteroatom-doped graphene-based materials for energy-relevant electrocatalytic processes. *ACS Catal.* **2015**, *5*, 5207-5234.

## References

---

- [154] Feynman, R. P. There's plenty of room at the bottom. *Engineering and Science* **1960**, *23*, 22-36.
- [155] Binnig, G., Rohrer, H., Gerber, Ch. & Weibel, E. Surface studies by scanning tunneling microscopy. *Phys. Rev. Lett.* **1982**, *49*, 57-61.
- [156] Binnig, G. & Rohrer, H. Scanning tunneling microscopy. *Surface Science* **1983**, *126*, 236-244.
- [157] Binnig, G., Rohrer, H., Gerber, Ch. & Weibel, E. 7 x 7 Reconstruction on Si(111) resolved in real space. *Phys. Rev. Lett.* **1983**, *50*, 120-123.
- [158] Miranda, R., García, N., Baró, A. M., García, R., Peña, J. L. & Rohrer, H. Technological applications of scanning tunneling microscopy at atmospheric pressure. *Appl. Phys. Lett.* **1985**, *47*, 367-369.
- [159] Park, S.-I. & Quate, C. F. Tunneling microscopy of graphite in air. *Appl. Phys. Lett.* **1986**, *48*, 112-114.
- [160] Schneir, J., Sonnenfeld, R., Hansma, P. K. & Tersoff, J. Tunneling microscopy study of the graphite surface in air and water. *Phys. Rev. B* **1986**, *34*, 4979-4984.
- [161] Drake, B., Sonnenfeld, R., Schneir, J. & Hansma, P. K. Scanning tunneling microscopy of processes at liquid-solid interfaces. *Surface Science* **1987**, *181*, 92-97.
- [162] Liu, H. Y., Fan, F. R. F., Lin, C. W. & Bard, A. J. Scanning electrochemical and tunneling ultramicroelectrode microscope for high-resolution examination of electrode surfaces in solution. *J. Am. Chem. Soc.* **1986**, *108*, 3838-3839.
- [163] Itaya, K. & Tomita, E. Scanning tunneling microscope for electrochemistry – a new concept for the in situ scanning tunneling microscope in electrolyte solutions. *Surface Science* **1988**, *201*, L507-L512.
- [164] Chen, C. J. Introduction to scanning tunneling microscopy. Vol. 4. *Oxford University Press*, **1993**.
- [165] Oura, K., Katayama, M., Zotov, A. V., Lifshits, V. G. & Saranin, A. A. Surface science: An introduction. *Springer Science & Business Media*, **2003**.
- [166] Liang, Y. Direct instrumental identification of catalytically active sites using electrochemical scanning tunneling microscopy. Diss. *Technische Universität München*, **2019**.
- [167] Lustenberger, P., Rohrer, H., Christoph, R. & Siegenthaler, H. Scanning tunneling microscopy at potential controlled surfaces in electrolytic environment. *J. Electroanal. Chem. Interf. Electrochem.* **1988**, *243*, 225-235.

- [168] Auer, A. & Kunze-Liebhäuser, J. A universal quasi-reference electrode for in situ EC-STM. *Electrochem. commun.* **2019**, *98*, 15-18.
- [169] Auer, A., Sarabia, F. J., Griesser, C., Climent, V., Feliu, J. M. & Kunze-Liebhäuser, J. Cu(111) single crystal electrodes: Modifying interfacial properties to tailor electrocatalysis. *Electrochim. Acta* **2021**, *396*, 139222.
- [170] Auer, A., Ding, X., Bandarenka, A. S. & Kunze-Liebhäuser, J. The potential of zero charge and the electrochemical interface structure of Cu(111) in alkaline solutions. *J. Phys. Chem. C* **2021**, *125*, 5020-5028.
- [171] Stumm, C., Grau, S., Speck, F. D., Hilpert, F., Briega-Martos, V., Mayrhofer, K., Cherevko, S., Brummel, O. & Libuda, J. Reduction of oxide layers on Au(111): The interplay between reduction rate, dissolution, and restructuring. *J. Phys. Chem. C* **2021**, *125*, 22698-22704.
- [172] Stumm, C., Bertram, M., Kastenmeier, M., Speck, F. D., Sun, Z., Rodríguez-Fernández, J., Lauritsen, J. V., Mayrhofer, K. J. J., Cherevko, S., Brummel, O. & Libuda, J. Structural dynamics of ultrathin cobalt oxide nanoislands under potential control. *Adv. Funct. Mater.* **2021**, *31*, 2009923.
- [173] Hugelmann, M. & Schindler, W. Tunnel barrier height oscillations at the solid/liquid interface. *Surface Science* **2003**, *541*, L643-L648.
- [174] Simeone, K., Kolb, D., Venkatachalam, S. & Jacob, T. The Au(111)/electrolyte interface: A tunnel-spectroscopic and DFT investigation. *Angew. Chem. Int. Ed.* **2007**, *46*, 8903-8906.
- [175] Halbritter, J., Repphun, G., Vinzelberg, S., Staikov, G. & Lorenz, W. J. Tunneling mechanisms in electrochemical STM – distance and voltage tunneling spectroscopy. *Electrochim. Acta* **1995**, *40*, 1385-1394.
- [176] Pan, J., Jiang, T. W. & Lindsay, S. M. Tunneling barriers in electrochemical scanning tunneling microscopy. *J. Phys. Chem.* **1994**, *98*, 4205-4208.
- [177] Hugelmann, M. & Schindler, W. In situ distance tunneling spectroscopy at Au(111)/0.02 M HClO<sub>4</sub>: From faradaic regime to quantized conductance channels. *J. Electrochem. Soc.* **2004**, *151*, E97-E101.
- [178] Binnig, G., Fuchs, H. & Stoll, E. Surface diffusion of oxygen atoms individually observed by STM. *Surf. Sci. Lett.* **1986**, *169*, L295-L300.
- [179] Möller, R., Esslinger, A. & Koslowski, B. Noise in vacuum tunneling: Application for a novel scanning microscope. *Appl. Phys. Lett.* **1989**, *55*, 2360-2362.

## References

---

- [180] Sumetskii, M. & Kornyshev, A. A. Noise in STM due to atoms moving in the tunneling space. *Phys. Rev. B* **1993**, *48*, 17493.
- [181] Sumetskii, M., Kornyshev, A. A. & Stimming, U. Adatom diffusion characteristics from STM noise: theory. *Surf. Sci.* **1994**, *307-309*, 23-27.
- [182] Horcas, I., Fernández, R., Gómez-Rodríguez, J. M., Colchero, J., Gómez-Herrero, J. & Baro, A. M. WSXM: a software for scanning probe microscopy and a tool for nanotechnology. *Rev. Sci. Instrum.* **2007**, *78*, 013705.
- [183] Schmuki, P. & Virtanen, S. (Eds.) Electrochemistry at the nanoscale. *Springer Science & Business Media*, **2009**.
- [184] Nagahara, L. A., Thundat, T. & Lindsay, S. M. Preparation and characterization of STM tips for electrochemical studies. *Rev. Sci. Instrum.* **1989**, *60*, 3128-3130.
- [185] Wang, J. X., Markovic, N. M. & Adzic, R. R. Kinetic analysis of oxygen reduction on Pt(111) in acid solutions: Intrinsic kinetic parameters and anion adsorption effects. *J. Phys. Chem. B* **2004**, *108*, 4127-4133.
- [186] Tripković, V, Skúlason, E., Siahrostami, S., Norskov, J. K. & Rossmeisl, J. The oxygen reduction reaction mechanism on Pt(1 1 1) from density functional theory calculations. *Electrochim. Acta* **2010**, *55*, 7975-7981.
- [187] Marković, N. M., Adžić, R. R., Cahan, B. D. & Yeager, E. B. Structural effects in electrocatalysis: oxygen reduction on platinum low index single-crystal surfaces in perchloric acid solutions. *J. Electroanal. Chem.* **1994**, *377*, 249-259.
- [188] Wakisaka, M., Suzuki, H., Mitsui, S., Uchida, H. & Watanabe, M. Identification and quantification of oxygen species adsorbed on Pt(111) single-crystal and polycrystalline Pt electrodes by photoelectron spectroscopy. *Langmuir* **2009**, *25*, 1897-1900.
- [189] Bondarenko, A. S., Stephens, I. E. L., Hansen, H. A., Pérez-Alonso, F. J., Tripkovic, V., Johansson, T. P., Rossmeisl, J., Norskov, J. K. & Chorkendorff, I. The Pt(111)/electrolyte interface under oxygen reduction reaction conditions: An electrochemical impedance spectroscopy study. *Langmuir* **2011**, *27*, 2058-2066.
- [190] Gómez-Marín, A. M., Rizo, R., & Feliu, J. M. Oxygen reduction reaction at Pt single crystals: A critical overview. *Catal. Sci. Technol.* **2014**, *4*, 1685-1698.
- [191] Jinnouchi, R., Kodama, K., & Morimoto, Y. DFT calculations on H, OH and O adsorbate formations on Pt(111) and Pt(332) electrodes. *J. Electroanal. Chem.* **2014**, *716*, 31-44.

- [192] Maciá, M. D., Campiña, J. M., Herrero, E. & Feliu, J. M. On the kinetics of oxygen reduction on platinum stepped surfaces in acidic media. *J. Electroanal. Chem.* **2004**, *564*, 141-150.
- [193] Hoshi, N., Nakamura, M. & Hitotsuyanagi, A. Active sites for the oxygen reduction reaction on the high index planes of Pt. *Electrochim. Acta* **2013**, *112*, 899-904.
- [194] Calle-Vallejo, F., Pohl, M. D., Reinisch, D., Loffreda, D., Sautet, P. & Bandarenka, A. S. Why conclusions from platinum model surfaces do not necessarily lead to enhanced nanoparticle catalysts for the oxygen reduction reaction. *Chem. Sci.* **2017**, *8*, 2283-2289.
- [195] Haid, R. W., Kluge, R. M. & Bandarenka, A. S. In situ quantification of the local electrocatalytic activity via electrochemical scanning tunneling microscopy. *Small Methods* **2021**, *5*, 2000710.
- [196] Wakisaka, M., Asizawa, S., Uchida, H. & Watanabe, M. In situ STM observation of morphological changes of the Pt(111) electrode surface during potential cycling in 10 mM HF solution. *Phys. Chem. Chem. Phys.* **2010**, *12*, 4184-4190.
- [197] Jacobse, L., Huang, Y-F., Koper, M. T. M. & Rost, M. J. Correlation of surface site formation to nanoisland growth in the electrochemical roughening of Pt(111). *Nat. Mater.* **2018**, *17*, 277-282.
- [198] Kibler, L. A. Preparation and characterization of noble metal single crystal electrode surfaces. *International Society of Chemistry* **2003**.
- [199] Clavilier, J. The role of anion on the electrochemical behaviour of a {111} platinum surface; an unusual splitting of the voltammogram in the hydrogen region. *J. Electroanal. Chem. Interf. Electrochem.* **1980**, *107*, 211-216.
- [200] Marković, N. M., Schmidt, T. J., Grgur, B. N., Gasteiger, H. A., Behm, R. J. & Ross, P. N. Effect of temperature on surface processes at the Pt(111)-liquid interface: Hydrogen adsorption, oxide formation, and CO oxidation. *J. Phys. Chem. B* **1999**, *103*, 8568-8577.
- [201] Origin Lab, Gauss fit function. <https://www.originlab.com/doc/origin-help/gauss-fitfunc>, accessed on (26.01.2022).
- [202] Boudart, M. Turnover rates in heterogeneous catalysis. *Chem. Rev.* **1995**, *95*, 661-666.
- [203] Krupski, K., Moors, M., Jóźwik, P., Kobiela, T. & Krupski, A. Structure determination of Au on Pt(111) surface: LEED, STM and DFT study. *Materials.* **2015**, *8*, 2935-2952.
- [204] Tan, T. L., Wang, L.-L., Zhang, J., Johnson, D. D. & Bai, K. Platinum nanoparticle during electrochemical hydrogen evolution: Adsorbate distribution, active reaction species, and size effect. *ACS Catal.* **2015**, *5*, 2376-2383.

## References

---

- [205] Zhu, J., Hu, L., Zhao, P., Lee, Y. S. L. & Wong, K.-Y. Recent advances in electrocatalytic hydrogen evolution using nanoparticles. *Chem. Rev.* **2020**, *120*, 851-918.
- [206] Luo, W., Gan, J., Huang, Z., Chen, W., Qian, G., Zhou, X. & Duan, X. Boosting HER performance of Pt-based catalysts immobilized on functionalized vulcan carbon by atomic layer deposition. *Front. Mater.* **2019**, *6*, 251.
- [207] Wang, L., Sofer, Z. & Pumera, M. Catalytic hydrogen evolution reaction on “metal-free” graphene: key role of metallic impurities. *Nanoscale* **2019**, *11*, 11083-11085.
- [208] Jia, Y., Zhang, L., Du, A., Gao, G., Chen, J., Yan, X., Brown, C. L. & Yao, X. Defect graphene as a trifunctional catalyst for electrochemical reactions. *Adv. Mater.* **2016**, *28*, 9532-9538.
- [209] Sathe, B. R., Zou, X. & Asefa, T. Metal-free B-doped graphene with efficient electrocatalytic activity for hydrogen evolution reaction. *Catal. Sci. Technol.* **2014**, *4*, 2023-2030.
- [210] Zhang, J., Qu, L., Shi, G., Liu, J., Chen, J. & Dai, L. N,P-codoped carbon networks as efficient metal-free bifunctional catalysts for oxygen reduction and hydrogen evolution reactions. *Angew. Chem. Int. Ed.* **2016**, *55*, 2230.
- [211] Jiao, Y., Davey, K. & Qiao, S.-Z. Activity origin and catalyst design principles for electrocatalytic hydrogen evolution on heteroatom-doped graphene. *Nat. Energy* **2016**, *1*, 16130.
- [212] Jiang, H., Zhu, Y., Su, Y., Yao, Y., Liu, Y., Yang, X. & Li, C. Highly dual-doped multilayer nanoporous graphene: efficient metal-free electrocatalysts for the hydrogen evolution reaction. *J. Mater. Chem. A* **2015**, *3*, 12642-12645.
- [213] He, M., Fic, K., Frackowiak, E., Novák, P. & Berg, E. J. Ageing phenomena in high-voltage aqueous supercapacitors investigated by *in situ* gas analysis. *Energy Environ. Sci.* **2016**, *9*, 623-633.
- [214] Strmcnik, D., Castelli, I. E., Connell, J. G., Haering, D., Zorko, M., Martins, P., Lopes, P. P., Genorio, B., Østergaard, T., Gasteiger, H. A., Maglia, F., Antonopoulos, B. K., Stamenkovic, V. R., Rossmeisl, J. & Markovic, N. M. Electrocatalytic transformation of HF impurity to H<sub>2</sub> and LiF in lithium-ion batteries. *Nat. Catal.* **2018**, *1*, 255-262.
- [215] Lazouski, N., Chung, M., Williams, K., Gala, M. L. & Manthiram, K. Non-aqueous gas diffusion electrodes for rapid ammonia synthesis from nitrogen and water-splitting-derived hydrogen. *Nat. Catal.* **2020**, *3*, 463-469.

- [216] Kluge, R. M., Haid, R. W., Stephens, I. E. L., Calle-Vallejo, F. & Bandarenka, A. S. Monitoring the active sites for the hydrogen evolution reaction at model carbon surfaces. *Phys. Chem. Chem. Phys.* **2021**, *23*, 10051-10058.
- [217] Banhart, F., Kotakoski, J. & Krasheninnikov, A. V. Structural defects in graphene. *ACS Nano* **2010**, *5*, 26-41.
- [218] Geim, A. K. & Novoselov, K. S. The rise of graphene. *Nanosci. Nanotechnol.* **2009**, *11*, 183.
- [219] Hembacher, S., Giessibl, F. J., Mannhart, J. & Quate, C. F. Revealing the hidden atom in graphite by low-temperature atomic force microscopy. *PNAS*. **2003**, *100*, 12539-12542.
- [220] Davies, T. J., Hyde, M. E. & Compton, R. G. Nanotrench arrays reveal insight into graphite electrochemistry. *Angew. Chem. Int. Ed.* **2005**, *44*, 5121-5126.
- [221] Xie, A., Xuan, N., Ba, K. & Sun, Z. Pristine graphene electrode in hydrogen evolution reaction. *ACS Appl. Mater. Interfaces* **2017**, *9*, 4643-4648.
- [222] Wang, H., Li, X.-B., Gao, L., Wu, H.-L., Yang, J., Cai, L., Ma, T.-B., Tung, C.-H., Wu, L.-Z. & Yu, G. Three-dimensional graphene networks with abundant sharp edge sites for efficient electrocatalytic hydrogen evolution. *Angew. Chem. Int. Ed.* **2018**, *57*, 198-203.
- [223] Ferrari, A. G.-M., Brownson, D. A. C. & Banks, C. E. Investigating the integrity of graphene towards the electrochemical hydrogen evolution reaction (HER). *Scientific Reports*. **2019**, *9*, 15961.
- [224] Holmberg, N. & Laasonen, K. *Ab initio* electrochemistry: exploring the hydrogen evolution reaction on carbon nanotubes. *J. Phys. Chem. C* **2015**, *119*, 16166-16178.
- [225] Nørskov, J. K., Bligaard, T., Logadottir, A., Kitchin, J. R., Chen, J. G., Pandelov, S. & Stimming, U. Trends in the exchange current for hydrogen evolution. *J. Electrochem. Soc.* **2005**, *152*, J23.
- [226] Lai, S. C. S., Patel, A. N., McKelvey, K. & Unwin, P. R. Definitive evidence for fast electron transfer at pristine basal plane graphite from high-resolution electrochemical imaging. *Angew. Chem. Int. Ed.* **2012**, *51*, 5405-5408.
- [227] Holmberg, N. & Laasonen, K. Theoretical insight into the hydrogen evolution activity of open-ended carbon nanotubes. *J. Phys. Chem. Lett.* **2015**, *6*, 3956-3960.
- [228] Das, R. K., Wang, Y., Vasilyeva, S. V., Donoghue, E., Pucher, I., Kamenov, G., Cheng, H.-P. & Rinzler, A. G. Extraordinary hydrogen evolution and oxidation reaction activity from carbon nanotubes and graphitic carbons. *ACS Nano* **2014**, *8*, 8447-8456.

## References

---

- [229] Tang, C., Wang, H.-F., Chen, X., Li, B.-Q., Hou, T.-Z., Zhang, B., Zhang, Q., Titirici, M.-M. & Wei, F. Topological defects in metal-free nanocarbon for oxygen electrocatalysis. *Adv. Mater.* **2016**, *28*, 6845-6851.
- [230] Qu, K., Zheng, Y., Dai, S. & Qiao, S. Z. Graphene oxide-polydopamine derived N, S-codoped carbon nanosheets as superior bifunctional electrocatalysts for oxygen reduction and evolution. *Nano Energy* **2016**, *19*, 373-381.
- [231] Li, J.-C., Hou, P.-X., Zhao, S.-Y., Liu, C., Tang, D.-M., Cheng, M., Zhang, F. & Cheng, H.-M. A 3D bi-functional porous N-doped carbon microtube sponge electrocatalyst for oxygen reduction and oxygen evolution reactions. *Energy Environ. Sci.* **2016**, *9*, 3079-3084.
- [232] Zheng, Y., Song, H., Chen, S., Yu, X., Zhu, J., Xu, J., Zhang, K. A. I., Zhang, C. & Liu, T. Metal-free multi-heteroatom-doped carbon bifunctional electrocatalysts derived from a covalent triazine polymer. *Small.* **2020**, *16*, 2004342.
- [233] Maruyama, J., Maruyama, S., Fukuhara, T., Mizuhata, H., Takenaka, S., Yoshida, A. & Miyazaki, K. Bifunctional oxygen electrodes with highly step-enriched surface of Fe-N<sub>x</sub> containing carbonaceous thin film. *J. Electrochem. Soc.* **2020**, *167*, 060504.
- [234] Shin, J., Guo, J., Zhao, T. & Guo, Z. Functionalized carbon dots on graphene as outstanding non-metal bifunctional oxygen electrocatalyst. *Small* **2019**, *15*, 1900296.
- [235] Haid, R. W., Kluge, R. M., Schmidt, T. O. & Bandarenka, A. S. *In-situ* detection of active sites for carbon-based bifunctional oxygen reduction and evolution catalysis. *Electrochim. Acta* **2021**, *382*, 138285.
- [236] Tao, L., Wang, Q., Dou, S., Ma, Z., Huo, J., Wang, S. & Dai, L. Edge-rich and dopant-free graphene as a highly efficient metal-free electrocatalyst for the oxygen reduction reaction. *Chem. Commun.* **2016**, *52*, 2764-2767.
- [237] Shen, A., Zou, Y., Wang, Q., Dryfe, R. A. W., Huang, X., Dou, S., Dai, L. & Wang, S. Oxygen reduction reaction in a droplet on graphite: Direct evidence that the edge is more active than the basal plane. *Angew. Chem. Int. Ed.* **2014**, *53*, 10804-10808.
- [238] Yuan, W., Zhou, Y., Li, Y., Chun, L., Peng, H., Zhang, J., Liu, Z., Dai, L. & Shi, G. The edge- and basal-plane-specific electrochemistry of a single-layer graphene sheet. *Sci. Rep.* **2013**, *3*, 1-7.
- [239] Jiang, Y., Yang, L., Sun, T., Zhao, J., Lyu, Z., Zhuo, O., Wang, X., Wu, Q., Ma, J. & Hu, Z. Significant contribution of intrinsic carbon defects to oxygen reduction activity. *ACS Catal.* **2015**, *5*, 6707-6712.
- [240] Zhang, L., Xu, Q., Niu, J. & Xia, Z. Role of lattice defects in catalytic activities of graphene clusters for fuel cells. *Phys. Chem. Chem. Phys.* **2015**, *17*, 16733-16743.

- [241] Tang, C. & Zhang, Q. Nanocarbon for oxygen reduction electrocatalysis: Dopants, edges, and defects. *Adv. Mater.* **2017**, *29*, 1604103.
- [242] Lin, Y., Lu, Q., Song, F., Yu, L., Mechler, A. K., Schlögl, R. & Heumann, S. Oxygen evolution reaction at carbon edge sites: Investigation of activity evolution and structure–function relationships with polycyclic aromatic hydrocarbons. *Angew. Chem. Int. Ed.* **2019**, *58*, 8917.
- [243] Spöri, C., Kwan, J. T. H., Bonakdarpour, A., Wilkinson, D. P. & Strasser, P. The stability challenges of oxygen evolving catalysts: Towards a common fundamental understanding and mitigation of catalyst degradation. *Angew. Chem. Int. Ed.* **2017**, *56*, 5994-6021.
- [244] Li, G., Anderson, L., Chen, Y., Pan, M. & Chuang, P.-Y. A. New insights into evaluating catalyst activity and stability for oxygen evolution reactions in alkaline media. *Sustain. Energy Fuels* **2018**, *2*, 237-251.
- [245] Ferreira, K. N., Iverson, T. M., Maghlaoui, K., Barber, J. & Iwata, S. Architecture of the photosynthetic oxygen-evolving center. *Science* **2004**, *303*, 1831-1838.
- [246] Gorlin, Y. & Jaramillo, T. F. A bifunctional nonprecious metal catalyst for oxygen Reduction and Water Oxidation. *J. Am. Chem. Soc.* **2010**, *132*, 13612-13614.
- [247] Risch, M., Stoerzinger, K. A., Han, B., Regier, T. Z., Peak, D., Sayed, S. Y., Wei, C., Xu, Z. & Shao-Horn, Y. Redox processes of manganese oxide in catalyzing oxygen evolution and reduction: An in situ soft X-ray absorption spectroscopy study. *J. Phys. Chem. C* **2017**, *121*, 17682-17692.
- [248] Tian, L., Zhai, X., Wang, X., Li, J. & Li, Z. Advances in manganese-based oxides for oxygen evolution reaction. *J. Mater. Chem. A* **2020**, *8*, 14400-14414.
- [249] Roy, I., Wang, Q. & Chakrapani, V. Nature of reaction intermediates and origin of bifunctionality in manganese oxide. *J. Phys. Chem. C* **2020**, *124*, 5286-5299.
- [250] Post, J. E. Manganese oxide minerals: Crystal structures and economic and environmental significance. *PNAS* **1999**, *96*, 3447-3454.
- [251] Jin, Z. & Bard, J. A. Surface interrogation of electrodeposited MnO<sub>x</sub> and CaMnO<sub>3</sub> perovskites by scanning electrochemical microscopy: Probing active sites and kinetics for the oxygen evolution reaction. *Angew. Chem. Int. Ed.* **2021**, *60*, 794-799.
- [252] Kuo, C.-H., Mosa, I. M., Thanneeru, S., Sharma, V., Zhang, L., Biswas, S., Aindow, M., Alpay, S. P., Rusling, J. F., Suib, S. J. & He, J. Facet-dependent catalytic activity of MnO electrocatalysts for oxygen reduction and oxygen evolution reactions. *Chem. Commun.* **2015**, *51*, 5951-5954.

## References

---

- [253] Smith, P. F., Deibert, B. J., Kaushik, S., Gardner, G., Hwang, S., Wang, H., Al-Sharab, J. F., Garfunkel, E., Fabris, L., Li, J. & Dismukes, G. C. Coordination geometry and oxidation state requirements of corner-sharing  $\text{MnO}_6$  octahedra for water oxidation catalysis: An investigation of manganite ( $\gamma\text{-MnOOH}$ ). *ACS Catal.* **2016**, *6*, 2089-2099.
- [254] Ramírez, A., Hillebrand, P., Stellmach, D., May, M. M., Bogdanoff, P. & Fiechter, S. Evaluation of  $\text{MnO}_x$ ,  $\text{Mn}_2\text{O}_3$ , and  $\text{Mn}_3\text{O}_4$  electrodeposited films for the oxygen evolution reaction of water. *J. Mater. Chem. C* **2014**, *118*, 14073-14081.
- [255] Pickrahn, K. L., Park, S. W., Gorlin, Y., Lee, H.-B., Jaramillo, T. F. & Bent, S. F. Active  $\text{MnO}_x$  electrocatalysts prepared by atomic layer deposition for oxygen evolution and oxygen reduction reactions. *Adv. Energy Mater.* **2012**, *2*, 1269-1277.
- [256] Meng, Y., Song, W., Huang, H., Ren, Z., Chen, S.-Y. & Suib, L. Structure–property relationship of bifunctional  $\text{MnO}_2$  nanostructures: Highly efficient, ultra-stable electrochemical water oxidation and oxygen reduction reaction catalysts identified in alkaline media. *J. Am. Chem. Soc.* **2014**, *136*, 11452-14464.
- [257] Robinson, D. M., Go, Y. B., Mui, M., Gardner, G., Zhang, Z., Mastrogiovanni, D., Garfunkel, E., Li, J., Greenblatt, M. & Dismukes, G. C. Photochemical water oxidation by crystalline polymorphs of manganese oxides: structural requirements for catalysis. *J. Mater. Chem. A* **2013**, *135*, 3494-3501.
- [258] Huynh, M., Shi, C., Billinge, S., J. L. & Nocera, D. G. Nature of activated manganese oxide for oxygen evolution. *J. Am. Chem. Soc.* **2015**, *137*, 14887-14904.
- [259] Salmanion, M., Kudov, I., Vandichel, M., Aleshkevych & Najafpour, M. Surprisingly low reactivity of layered manganese oxide toward water oxidation in Fe/Ni-free electrolyte under alkaline conditions. *Inorg. Chem.* **2022**, *61*, 2292-2306.
- [260] Kakizaki, H., Ooka, H., Hayashi, T., Yamaguchi, A., Bonnet-Mercier, N., Hashimoto, K. & Nakamura, R. Evidence that crystal facet orientation dictates oxygen evolution intermediates on rutile manganese oxide. *Adv. Funct. Mater.* **2018**, *28*, 1706319.
- [261] Oxford, G. A. E. & Chaka, A. M. First-principles calculations of clean, oxidized, and reduced  $\beta\text{-MnO}_2$  surfaces. *J. Phys. Chem. C* **2011**, *115*, 16992-17008.
- [262] Takashima, T., Hashimoto, K. & Nakamura, R. Mechanisms of pH-dependent activity for water oxidation to molecular oxygen by  $\text{MnO}_2$  electrocatalysts. *J. Am. Chem. Soc.* **2012**, *134*, 1519-1527.
- [263] Maruyama, J., Maruyama, S., Fukuhara, T., Takao, Y. & Miyazaki, K. Nanoscopic combination of edge and flat planes in the active site for oxygen reduction and Evolution. *Eur. J. Inorg. Chem.* **2019**, *38*, 4117-4121.

- [264] Yang, S., Song, X., Zhang, P. & Gao, L. Facile synthesis of nitrogen-doped graphene–ultrathin MnO<sub>2</sub> sheet composites and their electrochemical performances. *ACS Appl. Mater. Interfaces* **2013**, *5*, 3317-3322.
- [265] Zhao, Y., Chang, C., Teng, F., Zhao, Y., Chen, G., Shi, R., Waterhouse, G. I. N., Huang, W. & Zhang, T. Defect-engineered ultrathin  $\delta$ -MnO<sub>2</sub> nanosheet arrays as bifunctional electrodes for efficient overall water splitting. *Adv. Energy Mater.* **2017**, *7*, 1700005.
- [266] Wang, H., Zhang, J., Hang, X., Zhang, X., Xie, J., Pan, B. & Xie, Y. Half-metallicity in single-layered manganese dioxide nanosheets by defect engineering. *Angew. Chem. Int. Ed.* **2015**, *54*, 1195-1199.
- [267] Liu, B., Sun, Y., Liu, L., Xu, S. & Yan, X. Advances in manganese-based oxides cathodic electrocatalysts for Li–air batteries. *Adv. Funct. Mater.* **2018**, *28*, 1704973.
- [268] Su, H.-Y., Gorlin, Y., Man, I. C., Calle-Vallejo, F., Nørskov, J. K., Jaramillo, T. F. & Rossmeisl, J. Identifying active surface phases for metal oxide electrocatalysts: a study of manganese oxide bi-functional catalysts for oxygen reduction and water oxidation catalysis. *Phys. Chem. Chem. Phys.* **2012**, *14*, 14010-14022.
- [269] Li, L., Feng, X., Nie, Y., Chen, S., Shi, F., Xiong, K., Ding, W., Qi, X., Hu, J., Wei, Z., Wan, L.-J. & Xia, M. Insight into the effect of oxygen vacancy concentration on the catalytic performance of MnO<sub>2</sub>. *ACS Catal.* **2015**, *5*, 4825-4832.
- [270] Li, Y.-F. & Liu, Z.-P. Active site revealed for water oxidation on electrochemically induced  $\delta$ -MnO<sub>2</sub>: Role of spinel-to-layer phase transition. *J. Am. Chem. Soc.* **2018**, *140*, 1783-1792.
- [271] Wang, Y., Hu, T., Chen, Y., Yuan, H. & Qiao, Y. Crystal facet-dependent activity of  $\alpha$ -Mn<sub>2</sub>O<sub>3</sub> for oxygen reduction and oxygen evolution reactions. *Int. J. Hydrog. Energy* **2020**, *45*, 22744-22751.
- [272] Tymoczko, J., Colic, V., Ganassin, A., Schuhmann, W. & Bandarenka, A. S. Influence of the alkali metal cations on the activity of Pt(1 1 1) towards model electrocatalytic reactions in acidic sulfuric media. *Catal. Today* **2015**, *45*, 96-102.
- [273] Arminio-Ravelo, J. A., Jensen, A. W., Jensen, K. D., Quinson, J. & Escudero-Escribano, M. Electrolyte effects on the electrocatalytic performance of iridium-based nanoparticles for oxygen evolution in rotating disc electrodes. *ChemPhysChem* **2019**, *20*, 2956-2963.
- [274] Goyal, A. & Koper, M. T. M. The interrelated effect of cations and electrolyte pH on the hydrogen evolution reaction on gold electrodes in alkaline media. *Angew. Chem. Int. Ed.* **2021**, *60*, 13452-13462.

## References

---

- [275] Kamat, G. A., Zeledón, J. A. Z., Gunasooriya, K. K., Dull, S. M., Perryman, J. T., Nørskov, J. K., Stevens, M. B. & Jaramillo, T. F. Acid anion electrolyte effects on platinum for oxygen and hydrogen electrocatalysis. *Commun. Chem.* **2022**, *5*, 1-10.
- [276] Haid, R. W., Ding, X., Sarpey, T. K., Bandarenka, A. S. & Garlyyev, B. Exploration of the electrical double-layer structure: Influence of electrolyte components on the double-layer capacitance and potential of maximum entropy. *Curr. Opin. Electrochem.* **2022**, *32*, 100882.
- [277] Ding, X., Scieszka, D., Watzele, S., Xue, S., Garlyyev, B., Haid, R. W. & Bandarenka, A. S. A systematic study of the influence of electrolyte ions on the electrode activity. *ChemElectroChem* **2022**, *9*, e202101088.
- [278] Strmcnik, D., Kodama, K., van der Vliet, D., Greeley, J., Stamenkovic, V. R. & Marković, N. M. The role of non-covalent interactions in electrocatalytic fuel-cell reactions on platinum. *Nature Chem.* **2009**, *1*, 466-472.
- [279] Li, G.-F., Divinagracia, M., Labata, M. F., Ocon, J. D. & Chuang, P.-Y. A. Electrolyte-dependent oxygen evolution reactions in alkaline media: electrical double layer and interfacial interactions. *ACS Appl. Mater. Interfaces* **2019**, *11*, 33748-33758.
- [280] Xue, S., Garlyyev, B., Watzele, S., Liang, Y., Fichtner, J., Pohl, M. D. & Bandarenka, A. S. Influence of alkali metal cations on the hydrogen evolution reaction activity of Pt, Ir, Au, and Ag electrodes in alkaline electrolytes. *ChemElectroChem* **2018**, *5*, 2326-2329.